



City Research Online

City, University of London Institutional Repository

Citation: Zhu, Y. (1996). Digital signal and image processing techniques for ultrasonic non-destructive evaluation. (Unpublished Doctoral thesis, City, University of London)

This is the accepted version of the paper.

This version of the publication may differ from the final published version.

Permanent repository link: <https://openaccess.city.ac.uk/id/eprint/30983/>

Link to published version:

Copyright: City Research Online aims to make research outputs of City, University of London available to a wider audience. Copyright and Moral Rights remain with the author(s) and/or copyright holders. URLs from City Research Online may be freely distributed and linked to.

Reuse: Copies of full items can be used for personal research or study, educational, or not-for-profit purposes without prior permission or charge. Provided that the authors, title and full bibliographic details are credited, a hyperlink and/or URL is given for the original metadata page and the content is not changed in any way.

**Digital Signal and Image
Processing Techniques for
Ultrasonic Nondestructive
Evaluation**

by

Yong Zhu

Thesis submitted for the degree of

DOCTOR OF PHILOSOPHY

Department of Electrical, Electronic and

Information Engineering

The City University

London

June 1996

Contents

Acknowledgments	1
Copyright	2
Abstract	3
1. Introduction	4
2. Theory: Scattering and attenuation	8
2.1 Frequency dependence of scattering and absorption	9
2.2 Scattering characteristics in the time and space domains	14
3. Theory: Signal detection	16
3.1 Theory of signal detection	16
3.2 Fixed threshold detector	20
3.3 Adaptive detection	23
3.3.1 Cell-averaging CFAR detector	25
3.3.2 ACML-CFAR detector	29
4. Theory: Signal enhancement	35
4.1 Split spectrum processing methods	36
4.1.1 Split spectrum minimisation	40
4.1.2 Split spectrum polarity thresholding	41
4.1.3 SSP parameter selection	43
4.2 Adaptive filtering.....	49
4.2.1 Adaptive systems.....	50
4.2.2 FIR adaptive filtering and noise canceling	51
4.2.3 NLMS adaptive algorithm.....	56
4.2.4 Adaptive filter with bandpass filtered reference input	61

5. Optimal time-space array processing and image enhancement	63
5.1 Optimal time-space array processing	63
5.1.1 Time-space array representation of a line A-scan array	63
5.1.2 Minimum-noise distortionless response matrix filtering	67
5.1.3 Minimum-noise distortionless response filter: performance	72
5.1.4 Minimum-variance distortionless response filtering	76
5.1.5 Minimum-noise distortionless response filter: Implementation	77
5.2 Adaptive Wiener filter	80
5.2.1 Adaptive Wiener filtering for image enhancement	81
5.2.2 Performance of adaptive Wiener filter	86
5.2.3 Attenuation compensation	87
6. Results	90
6.1 Experimental systems	91
6.1.1 Data acquisition	91
6.1.2 Testing material and targets	92
6.2 Results: Detection	96
6.3 Results: Split spectrum processing	102
6.3.1 Processing parameter selection	102
6.3.2 Processing results	103
6.3.3 Discussion	114
6.4 Results: Adaptive filtering	116
6.4.1 Processing parameter selection	116
6.4.2 Processing results	116
6.4.3 Adaptive filtering with bandpass filtered reference input	124
6.4.4 Processing results using a non-uniformly excited transducer	127
6.5 Results: Optimal array processing and image enhancement	131
6.5.1 Time-space array processing	134
6.5.2 Adaptive Wiener filtering	139
6.5.3 Discussion	142

7. Conclusion.....	143
8 Future work.	147
Glossary of acronyms.....	150
References	151

Acknowledgements

I am most indebted to Dr. J.P. Weight for his constant encouragement, valuable advice and helpful support. I am also most grateful to Professor K.T.V. Grattan, the head of the Electrical, Electronic and information Engineering Department for his encouragement and support; to Professor A.F. Brown, Professor R.E. Challis and Dr. T.J. Ellis for their comments and helpful suggestions on the manuscript, to Mr. R. Vipond for giving useful advice on microscopic examination of the testing material.

I am thankful to the Ministry of Defence for financial support (Research Contract Agreement No: 2090/75) and Mr. A. Dunhill, at NDT department of Rolls-Royce plc for providing valuable experimental data in evaluating the signal processing techniques presented here.

I am also deeply indebted to my wife YuWan Liu for her forbearance, unwavering backing, and helpful advice on computer graphics.

Copyright declaration

I grant power of discretion to the University Librarian to allow this thesis to be copied in whole or in part without further reference to me. This permission covers only single copies made for study purpose, subject to normal conditions of acknowledgement.

Abstract

A number of signal and image processing methods have been developed and evaluated for applications in ultrasonic quantitative non-destructive testing of highly scattering materials. The work falls into three main areas: signal and image enhancement and signal detection.

Analyses have been made of the differential features of grain and defect scattering in the frequency, time and space domains. The insight gained has led to the development of novel multi-channel adaptive filtering approaches to enhance true defect signals and images. The methods used include: normalised least-mean square error adaptive filtering, minimum-variance distortionless response array-processing and two-dimensional adaptive Wiener filtering. Automatic detection of the enhanced signals is achieved using constant false alarm rate detectors adapted and developed from well-established radar techniques. Two approaches have been used: cell-averaging detection and automatically censored mean level detection.

The performances of all the approaches are evaluated by processing extensive sets of A-scan data from test blocks containing artificial targets and a real flaw. Comparisons between the new adaptive filtering and detection approaches and existing methods such as split spectrum processing and spatial averaging have been presented in a number of tables summarising performance over a set of 64 sequential A-scans. These results show that the new approaches can detect all the test targets, with near zero false alarms, representing a considerable improvement over the performance of existing methods. The results of array and image processing are presented as false colour B-scan images in which the visibility of defect images corrupted by grain scattering has been considerably enhanced. An important feature of the current work is that fixed processing parameters have been used throughout.

1. Introduction

The ultrasonic pulse-echo method was originally developed to detect submarines during the first World War. In the early 1940s, ultrasonic pulse echo techniques were introduced to detect defects in materials. Since then, they have been developed to become some of the most versatile tools for quantitative non-destructive evaluation of materials and the location and characterisation of defects.

As the sound wave interacts with materials mechanically, it can provide more information concerning the mechanical properties of the testing materials than can, for instance, electromagnetic techniques. However, the sensitivity and resolution of ultrasonic pulse-echo techniques are limited by a number of factors such as: transducer size and frequency, pulse length, material absorption and grain scattering, etc. In general, to achieve high axial and lateral resolution, a high frequency, short pulse length and narrow beam width should be used. Short pulses can be obtained with heavily damped transducers but at the expense of overall sensitivity. To achieve a pencil-like beam, the transducer radius must be at least a few centre-frequency wavelengths. On other hand, it must be borne in mind that absorption and scattering tend to increase with frequency, therefore the sensitivity would decrease with frequency. So a compromise must be struck between the requirements for axial resolution and sensitivity. In the near field, the beam width approximates to the transducer diameter, so the lateral resolution is relatively constant with range. However the structure of echo responses from near- field targets can be greatly complicated by diffraction effects, especially for the case of a solid medium of propagation [Weight, J.P., 1982, 1993][Stacey, R., 1993][Lhemery, A., 1995]. In general, this complication becomes less important in the far field. However, once again a compromise must be struck, since if the transducer aperture is chosen to be small enough to ensure that targets lie in the far field, the lateral resolution and sensitivity suffers as a result of the beam spreading, by an amount proportional to the ratio of the central frequency wavelength to the transducer aperture.

In the present work the material of interest is coarse-grained Waspaloy. Waspaloy is a Nickel based superalloy designed to maintain high strength in demanding high-temperature environments [Shen, G.]. A typical example is the disk like structures anchoring the turbine blades in a jet engine. Since jet engine disks are safety-critical components, the ability to detect small defects with reliability guaranteed by a large safety margin is, of course, of paramount importance. However, as a result of the coarse-grained microstructure of Waspaloy, the detection of small flaws is often limited by the masking effect of scattering from grain boundaries. Such scattering arising from within the bulk of a "defect free" material is referred to hereafter as "grain noise".

As is well known, "grain noise" is a coherent interference pattern arising from the interaction of ultrasonic waves backscattered by the, in general, randomly distributed grains. Usually, the interference pattern depends on both the frequency content of the transmitted signal and the position of the transducer over the material being tested. Since grain noise is coherent, it cannot be reduced by conventional time averaging. The objective of the current application is to develop and evaluate digital signal and image processing methods based on established radar and sonar techniques, both to enhance the defect signal to grain noise ratio (SNR)¹ and to improve the detection of small defects in highly scattering materials. In the main, conventional ultrasonic pulse echo techniques and transducers are used, but some results obtained with a specially developed high-resolution transducer are included.

Most existing techniques to "clean up" grain noise are based on either the spatial or frequency characteristics of grain scattering. Examples are: spatial and frequency averaging [Kraus, S.], bandpass filtering [Shankar, P.M.], Split-spectrum minimisation (SSM) and SSM in conjunction with polarity thresholding (SSPTM) [Newhouse, V.L.], [Bilgutay, N.M.], [Yue, L.]. Some of these methods can give very promising signal enhancement if optimum parameters are used [Karpur, P., 1987]. An alternative approach developed for a related problem in

¹ A glossary of acronyms is on page 150.

sonar beamforming systems [Yan, A.], is to enhance the signal-to-noise ratio by adaptive filtering that makes use of differential spatial features between the signals and noise as received by a sensor array. A major advantage of such an approach is its self-optimising nature, which avoids requiring, *a priori*, detailed knowledge of input data to choose optimum parameters.

The present work makes use of these latter concepts, in particular the analysis of the differential features of grain and defect scattering. This has led to the development of novel multi-channel adaptive filtering approaches for the current application. The methods used to enhance the defect signals and images include: normalised least-mean-square error adaptive filtering [Zhu, Y., 1994], minimum-variance distortionless response array-processing and two-dimensional adaptive Wiener filtering. Automatic detection of the enhanced signals is achieved using constant false alarm rate detectors adapted and developed from well-established radar techniques [Zhu, Y., 1993]. Two approaches have been used: cell-averaging detection and automatically censored mean level detection.

In practical quantitative non-destructive evaluation (QNDE), the main task can be divided into two main procedures referred to as pre-processing and post-processing. The objectives of pre-processing are searching to locate all potential defects and deciding whether further post-processing is necessary. Thus the pre-processing should be performed on-line in real-time. The potential defects detected can then be further analysed by post-processing to accurately locate, size, characterise and classify these defects. This actually is also a double check for verifying whether a potential defect detected in the pre-processing is a real defect. The post-processing is usually only required for a small portion of the test materials, e.g. only for those failing to pass the pre-processing. As the post-processing is often computationally intensive, it is usually performed off-line. Since the pre-processing needs to be performed on-line in real-time, it is highly desirable to have some means to detect automatically the existence of any true target signals, especially for one-dimensional signal processing. Possible approaches include fixed thresholding detectors widely used in practical QNDE and recently

introduced adaptive detection methods whereby the detection threshold is automatically adjusted to suit the nonstationary noise environment.

The developments and experimental evaluation of the methods mentioned above and on various combinations of them will be presented here. In particular, the use of spatial and frequency decorrelation techniques combined with adaptive filtering has been developed to enhance the signal-to-noise ratio. The true defect signals are then identified automatically using constant false alarm rate detectors adapted from radar detection techniques. Furthermore, minimum-variance distortionless-response array-processing and two-dimensional adaptive Wiener filtering techniques are introduced and developed to explore differential features between the signal and noise in both spatial and time domain to enhance the B-scan image. The performance of the approaches investigated are evaluated by processing extensive A-scan data from test blocks of highly scattering materials containing both artificial targets and real flaws. Comparisons between the various methods have been presented in a number of tables summarising performance over a data set containing 64 A-scans or in false colour B-scan images.

In Chapter 2, relevant absorption/scattering attenuation theory is examined first to identify any possible differential features between the signals from grain scattering and those from typical defect echoes. The insights gained from such investigations are then used to select and develop signal processing techniques that may prove suitable for the current application. The theories of the relevant signal detection, signal and image enhancement techniques are then reviewed and developed in the following chapters. Since signal detection processing can be used to provide an objective and consistent comparison of the performance among various signal enhancement methods, the signal detection methods are presented in Chapter 3 before the signal and image enhancement algorithms are introduced and developed in Chapters 4 and 5 respectively. The data acquisition system, the testing material and targets, and extensive evaluation results of all processing methods investigated are given in Chapter 6. Some suggested areas of future work are given in Chapter 7, before drawing the final conclusions in Chapter 8.

2. Theory: scattering and attenuation

The ultrasonic pulse-echo method is a very effective non-destructive testing technique for detecting and locating defects in test components. In this, a transducer is employed in transmit-receive mode to interrogate the targets. The time series waveform received at a stationary testing position is usually called an A-scan trace. The decision on the presence of defects is made based on the information obtained from the A-scans containing waves scattered from the defect boundaries. More detailed defect characterisations can be also obtained from the A-scans by the post-processing.

In order to identify useful information within the backscattered waves to be able to discriminate the defect signal from grain noise, it is instructive to consider the time, frequency and spatial domain characteristics of the ultrasonic scattering arising from both the grain structures of the bulk material and from typical defects of interest.

Depending on the dimension of the effective reflection surface of the defect boundary relative to the dominant wavelength of the ultrasound and the orientation of the defect relative to the sound beam, the information can be interpreted by using purely geometric-optical concepts or by taking account of general diffraction effects. For example, a transverse crack with a large smooth boundary facing the incident ultrasound beam can be treated as a mirror, whereas for a small defect with dimensions similar to the wavelengthes, diffraction effects will become

important. It should be noted that the amplitude of the echo response from a flaw depends not only on the size of its reflection surface but also its orientation relative to the incident ultrasound beam. Thus the designation "small" by no means implies the real geometrical size of the flaw, therefore its seriousness.

A full theoretical model to predict a single A-scan time series, taking into account the plane- and diffracted edge-wave nature of the beam radiated into a solid from typical transducers, the scattering from grain boundaries and any defects present, and the resulting output from a receiving transducer - is not available, but a useful starting point is to consider classical plane-wave scattering characteristics.

Since the current application involves scanning the transducer over the whole area of the test piece, any changes in the way in which the grain scattering and defect signals vary with transducer position will also be explored.

2.1 Frequency dependence of scattering and absorption

In practical ultrasonic non-destructive testing, attenuation effects are present in any real material. In general, the overall reduction in (plane-wave) signal amplitude can be attributed to energy loss caused by grain scattering (scattering attenuation), or by energy conversion from sound into heat (absorption attenuation). Scattering attenuation is mainly due to the incident and the reflected sound energy being diffracted at grain boundaries. Whereas absorption attenuation involves dissipative processes such as thermal conduction, or relaxation. The dissipative processes tend to slow down the oscillations of the particles and

weaken the transmitted energy of both the wanted echo from flaws and unwanted scattering from grains.

On the one hand, the attenuation effects may limit the ultrasonic testing range or the minimum detectable defect size. On the other hand, any differential feature of the attenuation effects for defects and grains could be made use of in discriminating defect signals from grain noise.

Considering plane-wave theory, it is well known [Mason, W.P.] that the scattering and absorption effects are dependent on the sound wavelength in relation to size of scatterer. The total attenuation of a sound wave which has travelled over a distance z can be described by

$$A(f) = A_0(f)e^{-\alpha(f)z}$$

Eq. 2.1

where $A_0(f)$ and $A(f)$ are the amplitudes of the transmitted sound waveform and the received echo waveform, respectively. The total attenuation coefficient $\alpha(f)$ consists of the absorption component $\alpha_a(f)$ and the scattering component $\alpha_s(f)$. That is

$$\alpha(f) = \alpha_a(f) + \alpha_s(f)$$

Eq. 2.2

where, for many materials, the absorption coefficient $\alpha_a(f)$ is proportional to frequency, i.e.

$$\alpha_a(f) = C_a f$$

Eq. 2.3

As is well known, the form of the scattering coefficient $\alpha_s(f)$ varies according to the size D of the scatterers in terms of the wavelength λ of the impinging ultrasound. If $D \ll \lambda$ we have Rayleigh scattering, for $D \cong \lambda$ stochastic scattering, and diffusion scattering or reflection when $D \gg \lambda$ [Papadakis, E.P., 1981].

For the Rayleigh region, the scattering coefficient varies with D and λ according to

$$\alpha_s(f) = C_R D^3 f^4$$

if $D \ll \lambda$,

Eq. 2.4

where C_R is a constant related to the material properties such as anisotropy.

For a stochastic scattering region, the scattering coefficient is less sensitive to D and λ , and is given by

$$\alpha_s(f) = C_S D f^2$$

if $D \cong \lambda$,

Eq. 2.5

in which C_S is a constant independent of any anisotropy.

In the diffusion region, the scattering coefficient is independent of frequency but is inversely proportional to D

$$\alpha_s(f) = C_d \frac{1}{D}$$

if $D \gg \lambda$,

Eq. 2.6

again C_d being a constant related to the material properties such as anisotropy.

In fine-grain materials the backscattering from grain boundaries - the grain "noise" - can be mainly attributed to Rayleigh scattering, since in most ultrasonic non-destructive testing applications the wavelengths used are considerably larger than the average grain size. Furthermore, as a result of the random grain size and orientation, each multi-faceted grain boundary can act as a collection of small scatterers. For the material of the current interest, it is known that the grain structure can vary dramatically for components undergoing different heat treatment and may even vary within a single component [Shen, G.]. Typically the mean grain size D can be from 0.02mm to 0.2mm and an investigation of the actual structure of a representative sample of the material used here will be presented later but it is convenient to report at this point that the mean grain size D is about 0.1mm. Whereas, for the centre frequency of the transducers used in the current work, the wavelengths λ are in the range of 0.6 ~ 1.2mm. Thus, in general the majority of the grain scattering may be considered to be in the Rayleigh region for the dominant frequencies in typical interrogating pulses. Therefore according to the above scattering theory, the grain scattering is strongly frequency dependent. Although the planar targets considered in the current work (0.6 - 1mm) are comparable in size to the pulse wavelengths, they will tend to preferentially scatter the higher

frequencies in the direction of the transducer, bearing in mind that each target has in effect just one normally-aligned facet. However in returning to the transducer, the target scattering will be attenuated by the frequency dependent grain scattering and the final outcome can be that the lower frequency components dominate in the received target signal. This means that higher frequencies are likely to be more predominant in the grain noise than in the target signals and target signals should have longer correlation length in the time-space domain than does the grain scattering. These differential features could be used to optimise the frequency domain based processing and may be used to preferentially enhance the target signals in the time-space domain adaptive filtering approaches.

Furthermore, as a result of the relatively simple geometry and large size of the normally small number of flaws compared to the much larger number of grains with smaller average size, the frequency dependence of the interference pattern arising from grain scattering is likely to be stronger and more complicated than that of the defect echoes. This means that in the frequency domain, the defect scattering on the whole may fluctuate less than does the grain noise. Such characteristics point to the use of frequency-diverse techniques such as split spectrum processing. Alternatively, adaptive filtering with bandpass-filtered reference approach and optimal rule-based adaptive array processing may be appropriate, especially as any differential features in both of the spatial and the frequency domains may be exploited.

The frequency domain differential features discussed above will be illustrated later in Section 6.4.3 by comparing the frequency spectrum of the signal from a real defect with that from a representative sample of grain noise obtained from the same test piece under the same experimental conditions.

2.2 Scattering characteristics in the time and space domains

Theoretical analyses and experimental results have shown that the probability distribution function (PDF) of grain noise amplitude within a single A-scan trace can be modelled by a Rayleigh distribution function [Saniie, J. 1986, 1988] [Luis, V.D.]. However in general, a priori knowledge of the distribution parameter is usually not available and furthermore is likely to vary with physical conditions and even the testing locations. Such characteristics of the grain noise environment suggest that a nonparametric detection method should be applied. On the other hand, for the current application it is reasonable to anticipate that the probability distribution of grain noise amplitude will not vary greatly in closely spaced regions. So it may be possible to estimate the noise statistics from neighbouring regions and make use of them to extract potential differential features from the local region and its neighbouring regions. Therefore it could be used to discriminate defect signals from grain noise.

Furthermore, in scanning applications, the transmitted beam profile is likely to affect the spatial characteristics of sequential A-scans. The coupling ranges used in the current application were such that data was collected from an area lying in the far field for all but the highest frequencies in the pulse spectrum and therefore the beam width will be wider for the lower frequencies. Also, it has already been established that the lower-frequency components are likely to be more predominant in the target signals than in the grain noise (see Section 2.1 above). Therefore, it is likely that the target signals will vary less as the transducer is scanned than will the grain scattering. Consequently, it could be anticipated that the received target signals would have better spatial cross-correlation than does the grain noise. Such differential features between the target signal and the grain noise could be exploited in methods related to spatial correlation and a number of such techniques will be introduced and investigated later.

To verify the presence of such characteristics for the data of current interest, the normalised spatial cross-correlations for both the signals reflected from a known target and scattered from the grains in the same test block under same experimental conditions will be analysed. The results will be presented later in Section 6.4.2.

3. Theory: Signal detection

In this chapter, three different signal detection methods will be investigated. The relevant detection theories [Hou, X.Y.], [Finn, H.M.], [Himonas, S.D.] will be reviewed and developed for the current application in a unified approach.

3.1 Theory of signal detection

In ultrasonic QNDE, it is of course crucial to make a correct decision on whether a given signal is from a true defect or not. This task often becomes very difficult due to the uncertainties arising from the strong grain scattering that gives rise to signals of similar amplitude to those from a true defect. Under this circumstance, it is desirable to find an optimum decision rule to detect the defect signals automatically and consistently.

Depending on *a priori* knowledge of the wanted signals, signal detection can be classified as either coherent, or noncoherent. In coherent detection, the amplitude, phase, frequency and time delays of the expected signal should be known *a priori* - this requires a truly synchronous reference signal; conversely in noncoherent detection, these parameters can be unknown or random. In the current application, usually there is no synchronised reference signal, therefore the noncoherent detection method has to be used.

In general, sampled data x containing wanted signals masked by noise can be expressed as

$$x = s + n \quad x \in \Omega ,$$

Eq. 3.1

where Ω is the sample space, and s, n are the signal and noise sample respectively. Suppose that the noise samples n are independent and stationary with mean μ_0 , or *expectation*, $E[n] = \mu_0$. Then if the signal s is absent, the mean of the sample is

$$E[x] = \mu_0. \tag{Eq. 3.2}$$

This will be denoted as the *null* hypothesis H_0 . Meanwhile if the signal s is present, the mean of the samples becomes

$$\begin{aligned} E[x] &= E[s + n], \\ &= s + \mu_0 \equiv \mu_1. \end{aligned} \tag{Eq. 3.3}$$

This will be denoted by the alternative hypothesis H_1 .

The decision rule can be made based on hypothesis testing such that

$$\begin{array}{l} H_1 \\ x > T \\ H_0 \end{array} \tag{Eq. 3.4}$$

where T is a threshold level to be determined by statistical theory. This decision rule is a linear mapping from sample space Ω to decision space $D = D_0 \cup D_1$. Here D_0 denotes the region $(-\infty, T]$ and D_1 is the region (T, ∞) .

The detection performance of a decision rule can be quantified by two kinds of error probabilities associated with the test statistic x . An error of the first kind is defined for the case when

$$x > T,$$

but the null hypothesis H_0 is actually true, i.e., the signal is absent. The probability of this kind of error is defined as

$$\begin{aligned}
 p(x > T|H_0) &= p(x \in D_1|H_0), \\
 &= \int_{D_1} f(x|H_0)dx, \\
 &= \int_T^{\infty} f(x|H_0)dx, \\
 &\equiv p_f,
 \end{aligned}$$

Eq. 3.5

here $f(x)$ is the probability distribution function (PDF) and adopting radar terminology, p_f is the false alarm rate.

The second kind of error is defined for the case when

$$x \leq T,$$

but the alternative hypothesis H_1 is true, i.e., the signal is present. The corresponding probability is defined as the miss alarm probability p_m , given by

$$\begin{aligned}
 p_m &= p(x \leq T|H_1), \\
 &= p(x \in D_0|H_1), \\
 &= \int_{D_0} f(x|H_1)dx, \\
 &= \int_0^T f(x|H_1)dx.
 \end{aligned}$$

Eq. 3.6

The probability of detection p_d is defined such that the alternative hypothesis is decided while the signal is present, i.e.

$$\begin{aligned}
p(x > T|H_1) &= p(x \in D_1|H_1), \\
&= \int_{D_1} f(x|H_1)dx, \\
&= \int_T^{\infty} f(x|H_1)dx, \\
&= 1 - p_m, \\
&\equiv p_d.
\end{aligned}$$

Eq. 3.7

It is seen that the detection performance of a decision rule is dependent on the cumulative probabilities of the test statistic x . These can be directly calculated from the moment generating function (MGF) of the test statistic by using the residue theorem [Hou, X.Y.]. The MGF $\Phi_f(z)$ is defined as the expectation of e^{zx} under PDF $f(x)$. This is also equivalent to the Laplace transform of the PDF $f(x)$, i.e.

$$\begin{aligned}
\Phi_f(z) &= E_{f(x)}[e^{zx}], \\
&= \int_{-\infty}^{\infty} f(x)e^{zx} dx,
\end{aligned}$$

Eq. 3.8

and $f(x)$ can be expressed as

$$\begin{aligned}
f(x) &= \frac{1}{2\pi j} \int_c \Phi_f(z)e^{-xz} dz, \\
&= \sum_k \text{res}[\Phi_f(z)e^{-xz}, z_k],
\end{aligned}$$

Eq. 3.9

when $x > 0$, the contour of integration c includes a line crossing the real x axis at $x = c_1$ and joins a semicircle lying in the right half x -plane at infinity. Thus all the poles of $\Phi_f(z)$ that lie in the right half x -plane are enclosed in the contour c .

If the MGF $\Phi_f(z)$ satisfies

$$\lim_{|z| \rightarrow \infty} \Phi_f(z) = 0 \quad \text{for } x > 0,$$

Eq. 3.10

then the two most important measures of detection performance - the false alarm probability and the detection probability can be calculated directly for a given threshold T by

$$\begin{aligned} \int_T^{\infty} f(x|H_i) dx &= \int_T^{\infty} \sum_{ki} \text{res}[\Phi_{f_i}(z) e^{-zx}, z_{ki}] dx \\ &= \sum_{ki} \text{res}[\Phi_{f_i}(z) \frac{e^{-Tz}}{z}, z_{ki}] \\ &= p_i \end{aligned}$$

Eq. 3.11

where z_{ki} are the poles of $\Phi_{f_i}(z)$ lying in the right half-plane. Eq. 3.11 gives the false alarm probability when $i = 0$ (with MGF Φ_{f_i} evaluated under the null hypothesis), and the detection probability when $i = 1$ (under the alternative hypothesis).

In following sections, the use of both fixed and adaptive threshold detectors will be investigated following a unified approach based on the above hypothesis testing theory.

3.2 Fixed threshold detector

Since fixed threshold detection is still by far the most common method used to detect defect signals in industry, extensive tests to compare its performance with some more sophisticated adaptive detectors have been carried out here.

As mentioned before, in the current application there is no synchronised reference signal, thus the noncoherent detection method should be used here. Since in noncoherent detection only the amplitude information of the input signal is used in making a decision, a square law envelope detector is used to detect the envelope of the input signal prior to fixed threshold detection. In square law envelope detection, the incoming data is divided into a number of resolution cells of duration similar to that of the peak duration of the transmitted pulse. The point-by-point amplitude within each cell is squared and integrated to give an output power of each cell.

The power level of each cell can then be compared to the fixed threshold level, and any cell having a power greater than this is deemed to contain a defect signal. In practice, the threshold level can be set to just detect the signal from a suitable calibration target at the greatest depth of interest.

As mentioned in Section 2.2, the probability density function $f_i(x)$ for the amplitude of the grain noise can be modelled by a Rayleigh distribution. That is

$$\begin{aligned} f_i(x) &= f(x|H_i) \\ &= \frac{x}{\sigma_i^2} e^{-x^2/\sigma_i^2} \end{aligned} \tag{Eq. 3.12}$$

where σ_i is the distribution parameter defined as $\sigma_i^2 = \sigma_0^2(1+r_i)$ in which σ_0^2 is the grain noise variance, r_i is the average input SNR and $i = 0, 1$ denotes the distribution corresponding to a null or an alternative hypothesis, respectively

$$r_i = \begin{cases} 0 & \text{for } i = 0 \\ r & \text{for } i = 1. \end{cases} \tag{Eq. 3.13}$$

As mentioned above, a square law envelope detector is used to detect the envelope of the input signal prior to threshold detection, it is therefore necessary to derive the PDF $f_i(y)$ for the square law detector output. Since the original input data has a Rayleigh distribution, we can derive an expression for $f_i(y)$ using a fundamental theorem of probability theory [Papoulis, A.], i.e.

$$\begin{aligned} f_i(y) &= \sum_k \frac{f_i(x_k)}{|y'(x_k)|} \\ &= \frac{1}{\sigma_i^2} e^{-y/\sigma_i^2} u(y) \end{aligned}$$

Eq. 3.14

where $y'(x_k)$ are the derivatives of $y(x)$ at its real roots $x = x_k$ and $u(*)$ is the unit step function. The MGF of the $f_i(y)$ can then be calculated by

$$\begin{aligned} \Phi_{f_i}(z) &= \int_{-\infty}^{\infty} \frac{1}{\sigma_i^2} e^{-y/\sigma_i^2} u(y) e^{zy} dy \\ &= \frac{1}{1 - \sigma_i^2 z} \end{aligned}$$

Eq. 3.15

This MGF will be used throughout the following in order to provide a unified approach to evaluate the performance of all the detectors considered.

Clearly, $\Phi_{f_i}(z)$ has only one first order pole at $z_i = 1/\sigma_i^2$. So the false alarm probability ($i = 0$) and detection probability ($i = 1$) can be found from Eq. 3.11 and Eq. 3.15, i.e.

$$p_i = e^{-T/\sigma_i^2}.$$

Eq. 3.16

Therefore, the detection performance of the fixed thresholding detector is described by

$$p_f = e^{-T/\sigma_0^2},$$

Eq. 3.17

and

$$\begin{aligned} p_d &= e^{-T/\sigma_0^2(1+r)}, \\ &= p_f \frac{1}{1+r}. \end{aligned}$$

Eq. 3.18

From Eq. 3.17, it is seen that in fixed threshold detection, the false alarm probability is very sensitive to any fluctuation in noise variance and in many NDT applications this may vary with transducer positions. Therefore the consistency of detection performance can not be guaranteed. As will be discussed below, one approach to overcome such a limitation is to adjust the threshold level adaptively, taking account of fluctuations in noise level.

3.3 Adaptive detection

Adaptive detection techniques are widely used to improve detection of true targets in radar applications. One such approach is the Constant False Alarm Rate (CFAR) detection. In this the detection threshold is adjusted adaptively to maintain the required constant false alarm rate. This approach has been introduced into ultrasonic non-destructive evaluation in present work [Zhu, Y.]. Also, a related but different method has been used by [Saniie J., 1992].

As schematically illustrated in Figure 3.1, in a constant false alarm rate detector, the incoming signal is first fed to a square law envelope detector of the type described above. The output signal power of the square law detector is in turn compared with a decision threshold which itself is adaptively controlled by the desired false alarm rate and the noise level estimated from the surrounding reference cells. Depending on the way in which the noise level is estimated, such

adaptive detectors can be classified as Cell-Averaging [Finn, H.M.], Order Statistic [Rohling, H.] or Trimmed Mean [Gandhi P.P.].

The theory of some of these detectors will be reviewed in detail below but very briefly, in the Cell-Averaging (CA-CFAR) detector, the noise level is estimated from an equal weighted average of the noise power outputs from reference cells adjacent to the cell under test. Whereas in the Order Statistic (OS-CFAR) detector, the power of each range cell is ranked in ascending order. A k th. cell is empirically selected to represent the noise level. As a generalisation of the OS-CFAR detector, the TM-CFAR detector trims k_1 cells from the lower end and k_2 cells from the upper end of the rank ordered cells. The noise level is estimated from the mean of the remaining cells within the range $k_1 \leq k \leq k_2$. Again the trimming points need to be selected empirically.

Detailed analysis [Gandhi, P.P.] indicates that in a homogeneous noise environment and for a single target situation, the CA-CFAR detector gives better detection than an OS-CFAR detector, however the OS-CFAR detector has superior performance if multiple targets are present. The TM-CFAR detector offers a better performance over the OS-CFAR detector, if the trimming points k_1 , k_2 are properly selected based on *a priori* knowledge of the noise environment. However, this will become difficult in dealing with non-stationary noise. In order to select the trimming points adaptively, automatic censoring CFAR algorithms have recently been proposed [Himonas, S.D.]. It is one form of this latter type of detector that has been found to be most suited for the current application - the Automatic Censored Mean Level (ACML) detector. Details of this and the simpler Cell-Averaging detector are given below.

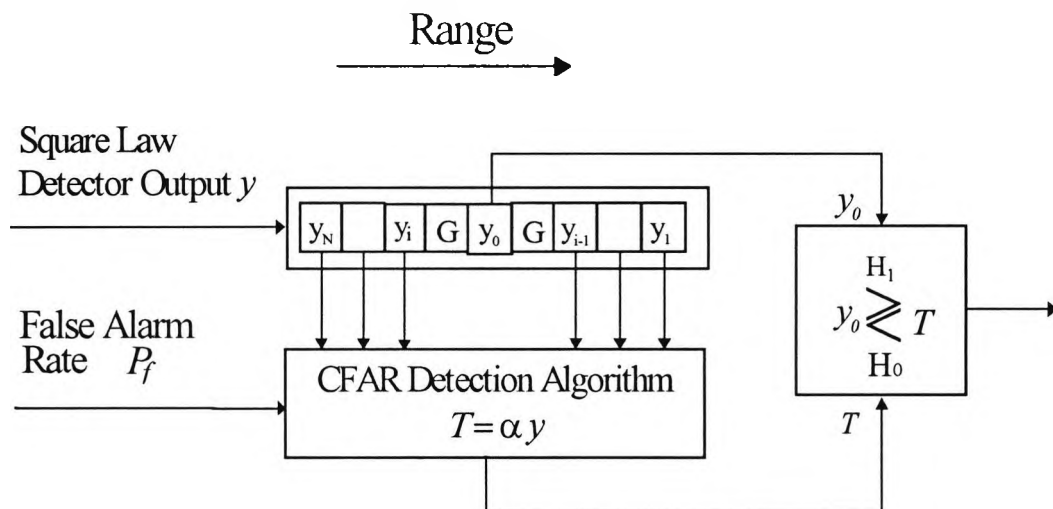


Figure 3.1 Schematic configuration of constant false alarm rate detector.

3.3.1 Cell-averaging CFAR detector

Constant false alarm rate detections are well-established techniques in radar applications [Finn, H.M.], [Hansen, V.G.], [Moor, J.D.]. For data suffering from homogeneous Gaussian noise, such as that anticipated to predominate at the output of the square law detector when fed with the data of current interest, a commonly used method is the cell-averaging CFAR technique (CA-CFAR). In this, the incoming data is demodulated by a square law detector as described in section 3.2. The output of the square law detector y_i is fed into each resolution cell of the adaptive detector. To achieve the desired false alarm rate, the decision threshold is set to an equal weighted average of the noise power outputs from cells adjacent to “guard” cells G either side of the cell under test. To avoid a potential problem due to signal components from a target “spilling over” to the cells adjacent to the test cell, the outputs from the guard cells are excluded when estimating the noise level.

Under the same assumption of the noise PDF given by Eq. 3.14 for a test cell, the MGF is still the same as Eq. 3.15. As mentioned before in Section 3.2,

since the false alarm rate is very sensitive to the noise variance, one approach is to adjust the threshold level adaptively according to the noise level estimated from reference cells surrounding the cell under test. The cell-averaging CFAR procedure [Finn, H.M.], [Moor, J.D.], assumes that the reference cells are homogeneous with the same variance σ_0^2 and may therefore be weighted equally in estimating the noise level y given by

$$y = \frac{1}{N} \sum_{i=1}^N y_i,$$

$$= \frac{\sigma_0^2}{N} \sum_{i=1}^N x_i^2,$$

Eq. 3.19

where the x_i^2 , $i=1,2,\dots,N$ terms are the outputs of a square law envelope detector and are assumed to be squared and statistically independent Gaussian random variables with zero mean. It should be noted that Eq. 3.19 differs from the corresponding expression in Radar applications where two, quadrature, signal channels need to be considered, as opposed to the single data channel in the current work. This results in the summation of Eq. 3.19 being over $i = 1$ to N rather than 1 to $2N$. Consequently, for the homogeneous noise with the same variance, the distribution for Ny/σ_0^2 will then be a chi-square PDF $g(y)$ with degree of freedom N

$$g(y) = \frac{1}{2^{\frac{N}{2}} \Gamma\left(\frac{N}{2}\right)} \frac{N}{\sigma_0^2} \left(\frac{N}{\sigma_0^2} y\right)^{\frac{N-2}{2}} e^{-\frac{Ny}{2\sigma_0^2}} u(y)$$

Eq. 3.20

where $\Gamma(*)$ and $u(*)$ are the gamma and step functions, respectively. For an adaptive threshold level T proportional to the estimated noise level y , i.e. $T = \alpha y$,

the expected probability of false alarm or true detection P_i , $i=0,1$, respectively, can be calculated from the above PDF $f(x)$, $g(y)$ (given by Eq. 3.14 and Eq. 3.20) and their MGF using Eq. 3.11, i.e.

$$\begin{aligned}
 P_i &= \int_0^{\infty} g(y) \int_{\alpha y}^{\infty} f(x) dx dy, \\
 &= \int_0^{\infty} g(y) \int_{\alpha y}^{\infty} \sum_{ki} \text{res}[\Phi_{f_i}(z) e^{-zx}, z_{ki}] dx dy, \\
 &= \sum_{ki} \text{res}[\Phi_{f_i}(z) \frac{\Phi_g(-\alpha z)}{z}, z_{ki}],
 \end{aligned}$$

Eq. 3.21

where the $\Phi_{f_i}(\cdot)$ and $\Phi_g(\cdot)$ are the MGF of the PDF $f(x)$ and $g(y)$ but the argument of $\Phi_g(\cdot)$ is replaced by $-\alpha z$. It should be noted that all the residues referred to here are dependent only on the poles of $\Phi_{f_i}(z)$. For the $\Phi_{f_i}(z)$ given in Eq. 3.15, Eq. 3.21 reduces to

$$\begin{aligned}
 P_i &= \Phi_g(-\alpha z_{ki}) \\
 &= \Phi_g\left(-\frac{\alpha}{\sigma_i^2}\right)
 \end{aligned}$$

Eq. 3.22

where the subscript $i = 0,1$ denotes that the corresponding MGF is evaluated at the poles of $\Phi_{f_i}(z)$ under the null or alternative hypothesis, respectively.

From Eq. 3.8 and Eq. 3.20, the MGF of the PDF $g(y)$ can be obtained by

$$\begin{aligned}\Phi_g(-\alpha z) &= \int_{-\infty}^{\infty} \frac{1}{2^{\frac{N}{2}} \Gamma\left(\frac{N}{2}\right)} \frac{N}{\sigma_0^2} \left(\frac{N}{\sigma_0^2} y\right)^{\frac{N-2}{2}} e^{-\frac{Ny}{2\sigma_0^2}} u(y) e^{-\alpha zy} dy, \\ &= \frac{1}{\left(1 + \frac{2\alpha\sigma_0^2 z}{N}\right)^{N/2}}.\end{aligned}$$

Eq. 3.23

From Eq. 3.22 and Eq. 3.23, the expected probability of false alarm P_f is found to be

$$\begin{aligned}P_f &= \Phi_g\left(-\frac{\alpha}{\sigma_0^2}\right), \\ &= \left(1 + \frac{2\alpha}{N}\right)^{-N/2},\end{aligned}$$

Eq. 3.24

and

$$\begin{aligned}P_d &= \Phi_g\left(-\frac{\alpha}{\sigma_1^2}\right), \\ &= \left(1 + \frac{2\alpha}{N(1+r)}\right)^{-N/2}.\end{aligned}$$

Eq. 3.25

The threshold scaling factor α for a desired constant false alarm rate P_f is then determined by

$$\alpha = \frac{N}{2} \left(P_f^{-2/N} - 1 \right)$$

Eq. 3.26

and the CFAR threshold level can be set to

$$T = \alpha y.$$

Eq. 3.27

Since it is assumed that there is no target signal present in the reference cells, they are all weighted equally in estimating the noise level. This implies that the CA-CFAR detector will only perform optimally if there is no wanted signal present in the reference range resolution cells. However, if there are a few wanted signals present in the reference cells, detection performance will be close to optimum, provided that their effect on estimating the noise level is negligible. Where this cannot be guaranteed, better performance can be obtained with an automatic censored mean level (ACML) detector - as discussed below.

3.3.2 ACML-CFAR detector

The ACML-CFAR detector [Himonas, S.D.] is designed for the situation where multiple target signals may exist but there is no sudden jump in noise level (so called “clutter edge” in radar terminology). In ACML-CFAR detection, all range cells $\{y_i\}$, $i=1, \dots, N$, are ranked in ascending order $\{y_{(i)}\}$, $i=1, \dots, N$, according to the magnitude of the power within each cell:

$$y_{(1)} \leq y_{(2)} \leq \dots \leq y_{(N)}.$$

Eq. 3.28

A decision needs to be made for the cut-off point above which all cells are deemed to contain wanted signals. This is known as the censoring point k which is determined adaptively according to the following testing hypothesis

$$y_{(k+1)} \underset{H_0}{\overset{H_1}{>}} \beta_k s_k,$$

Eq. 3.29

where the hypothesis H_0 denotes that $y_{(k+1)}$ is purely noise, while the hypothesis H_1 indicates that $y_{(k+1)}$ and consequently $y_{(k+2), \dots, y_{(N)}}$ are samples containing defect signal interference. Initially $s_1 = y_{(1)}$ and β_k is a scaling factor depending on the false censoring probability P_{fc} at the k th step of the censoring procedure. The false censoring probability is defined as the probability that hypothesis H_1 is taken to be true ($y_{(k+1)} > \beta_k s_k$) while the hypothesis H_0 is actually true. If the hypothesis H_0 is accepted at the k th step of the censoring procedure, the test will proceed to the $k+1$ step and the noise level estimation will be updated to $s_{k+1} = s_k + y_{k+1}$. Otherwise the censoring procedure will be stopped at the censoring point k and the estimated noise level will be

$$y = s_k,$$

$$= \sum_{i=1}^k y_i.$$

Eq. 3.30

The hypothesis testing equation (Eq. 3.29) can be represented by a equivalent test statistic defined as

$$u_k = y_{k+1} - \beta_k s_k.$$

Eq. 3.31

Using Eq. 3.9 and Eq. 3.11, the probability of false censoring P_{fc} can then be written as

$$\begin{aligned}
P_{fc} &= P(u_k > 0 | H_0), \\
&= \frac{1}{2\pi j} \int_c \Phi_{g(u_k | H_0)}(z) \frac{dz}{z},
\end{aligned}$$

Eq. 3.32

where $\Phi_{g(u_k | H_0)}(z)$ is the MGF of u_k under hypothesis H_0 .

Suppose the above censoring process stopped at the k th step and resulted in a subset of the order statistics (including the last one tested at the k th step $y_{(k+1)}$) defined in Eq. 3.28 as

$$y_{(1)} \leq y_{(2)} \leq \dots \leq y_{(k+1)}.$$

Eq. 3.33

The joint PDF of the subset is given by [Vaughan, R.J.]

$$g(y_{(1)}, \dots, y_{(k+1)}) = \frac{1}{k!(N-k-1)!} \text{per}|G|,$$

Eq. 3.34

where $\text{per}|G|$ is the permanent of a matrix G (similar to the determinant, except that all signs are positive)

$$\text{per}|G| = \left| \begin{array}{ccc}
F(y_{(k)}) & \dots & F(y_{(k)}) \\
\dots & \dots & \dots \\
F(y_{(k)}) & \dots & F(y_{(k)}) \\
f(y_{(k+1)}) & \dots & f(y_{(k+1)}) \\
1-F(y_{(k+1)}) & \dots & 1-F(y_{(k+1)}) \\
\dots & \dots & \dots \\
1-F(y_{(k+1)}) & \dots & 1-F(y_{(k+1)})
\end{array} \right| \begin{array}{l}
\} k \text{ rows} \\
\} N-k-1 \text{ rows}
\end{array}$$

Eq. 3.35

where $f(*)$ is the PDF of the cell outputs and $F(*)$ is the corresponding cumulative distribution function. It should be noted that the same function appears in each row of G , since the cell outputs are assumed to be statistically independent, and

identically distributed. Using the exponential random variables PDF Eq. 3.14, derived from the PDF Eq. 3.12 for the signal at the square-law detector input, the joint MGF of the subset order statistics can be found from Eq. 3.8 and Eq. 3.34 [Himonas, S.D.]

$$\begin{aligned}\Phi_{g(y_{(1)}, \dots, y_{(k+1)})}(z_1, \dots, z_{k+1}) &= E_{g(y_{(1)}, \dots, y_{(k+1)})} \left[\exp \left(\sum_{i=1}^{k+1} z_i y_{(i)} \right) \right], \\ &= \frac{N!}{(N-k-1)!} \prod_{i=1}^{k+1} \left(\frac{1}{v_i + N - i + 1} \right),\end{aligned}\tag{Eq. 3.36}$$

where

$$v_i = - \sum_{l=i}^{k+1} z_l.\tag{Eq. 3.37}$$

Here the distribution parameter σ in $g(*)$ has been normalised to unity since it will be cancelled in the derivation and therefore will not affect the final result - as has been shown in Eq. 3.20-Eq. 3.24.

By comparing the definition of the MGF $\Phi_{g(u_k|H_0)}(z)$ to Eq. 3.36, it is seen that $\Phi_{g(u_k|H_0)}(z)$ can be obtained from Eq. 3.36 by setting

$$\begin{aligned}z_1 = z_2 = \dots = z_k &= -\beta_k z, \\ z_{k+1} &= z.\end{aligned}\tag{Eq. 3.38}$$

Substituting $\Phi_{g(u_k|H_0)}(z)$ into Eq. 3.32 will give the probability of false censoring P_{fc} at the k th step of the censoring procedure as

$$P_{fc} = \binom{N}{k} \frac{1}{[1 + \beta_k(N - k)]^k}.$$

Eq. 3.39

The censoring scaling factor β_k can then be determined for a required false censoring probability P_{fc} .

The noise level y estimated from Eq. 3.29 and Eq. 3.30 is used to control the threshold level adaptively for each cell under test. The output of a test cell y_0 is then compared to the threshold to decide if a target signal is present - hypothesis H_1 - or if the test cell contains noise only - hypothesis H_0 :

$$\begin{array}{c} H_1 \\ y_0 > \alpha y, \\ H_0 \\ y_0 < \alpha y, \end{array}$$

Eq. 3.40

where α is scaling factor determined by the desired probability of false alarm p_f and the automatically selected censoring point k .

Similarly, by comparing the definition of the MGF of the noise estimator y $\Phi_{g(y)}(z)$ to Eq. 3.36, it can be found that $\Phi_{g(y)}(z)$ can be obtained from Eq. 3.36 by setting

$$z_i = z \quad i = 1, \dots, k + 1.$$

Eq. 3.41

The probability of a false alarm P_f can then be found by substituting the $\Phi_{g(y)}(z)$ into Eq. 3.22 to give

$$P_f = \binom{N}{k} \prod_{i=1}^k \left(\alpha + \frac{N-i+1}{k-i+1} \right)^{-1} .$$

Eq. 3.42

In practice, the false censoring rate P_{fc} can be set to be equal to the desired false alarm rate P_f .

As has been mentioned before, the performance of CA-CFAR and ACML-CFAR detectors for the current application will be evaluated by processing a group of 64 A-scans data taken from a Waspaloy Jet engine disc. The CA-CFAR and ACML-CFAR processing results will be compared with the fixed threshold detection results.

4. Theory: Signal enhancement

As mentioned before, in quantitative ultrasonic non-destructive evaluation of highly-scattering materials, the main limitation in detecting small flaws is the masking effect of "grain noise". Since such noise is coherent, it cannot be reduced by conventional time averaging. Usually, the ensuing interference pattern depends on both the frequency content of the transmitted signal and the position of the transducer over the material being tested. As discussed in chapter 2, in many applications, the grain scattering is often in the Rayleigh region, so that the grain noise pattern and the scattering attenuation is strongly frequency dependent. Existing techniques based on the frequency characteristics of grain scattering, include frequency averaging [Kraus, S. 1978], linear bandpass filtering [Shankar, P.M. 1988] [Murthy, R. 1989], and non-linear frequency diverse filtering, such as split spectrum processing (SSP) family [Newhouse, V.L. 1982] [Li, Y. 1987] [Bilgutay N.M. 1990]. Amongst these techniques, the SSP methods give very promising improvement in signal-to-noise ratios but can be sensitive to the optimum choice of parameters. This has motivated a number of researchers [Karpur, P., 1987, 1988], [Mohana, P. 1989] to seek systematic approaches to optimise the SSP parameters. Meanwhile alternative methods such as adaptive filtering have also been developed [Zhu, Y.]. The methods adapted from well-established radar and sonar techniques and developed for the current application, together with their feasibility in practice will be described and discussed in detail in the following sections.

4.1 Split spectrum processing

As has been described and demonstrated by a number of investigations (see above), "grain noise" from highly-scattering materials can be "cleaned up" by using split spectrum processing. Here, we further investigate the practical feasibility of this approach, running extensive tests with a large number of A-scans. The aim has been to evaluate the sensitivity of the method to changes in both the parameters used and the data itself. Brief outlines of the theory of the various SSP methods will be given, and new extensions to the SSP approaches will be introduced and evaluated here.

In split spectrum processing, it is assumed that the grain scattering can be described as Rayleigh scattering, thus according to the scattering theory described in Chapter 2, the scattering attenuation coefficient is proportional to the fourth power of the frequency of the ultrasonic wave. On the other hand, the flaw size is assumed to be much larger than the wavelengths used, hence the scattering from the flaw is in the diffusion region and the corresponding attenuation coefficient is independent of the frequency. So it is possible to make use of these differences to decorrelate and suppress the grain noise but keep the flaw echo unaffected. Based on such concepts, split spectrum processing methods were suggested to suppress grain noise via a frequency diversity approach that emulates the frequency agility techniques successfully used in radar systems to decorrelate and suppress clutter [Beasley, E.W.].

Suppose the received wideband signal $x(t)$ can be expressed as

$$\begin{aligned}x(t) &= s(t) + n(t) && \text{(under hypothesis } H_1: \text{ defect present)} \\x(t) &= n(t) && \text{(under hypothesis } H_0: \text{ defect absent)}\end{aligned}$$

Eq. 4.1

where $s(t)$ and $n(t)$ represent the defect signal and the grain noise, respectively. The SSP method involves "splitting" the received wideband signal $x(t)$ by passing it through a bank of N (normally overlapping) Gaussian bandpass filters (BPF) with equally spaced centre frequencies f_1, f_2, \dots, f_N - as shown in Figure 4.1.1. The filtering is usually performed in the frequency domain by multiplying the Fourier transform of the wideband signal $x(t)$, $X(f)$ with the frequency transfer function of each narrow bandpass filter, i.e.

$$X(f) = \mathcal{F}[x(t)] \tag{Eq. 4.2}$$

and

$$\begin{aligned} Z_i(f) &= X(f)H_i(f) \\ &= X(f)H(f - f_i) \quad i = 1, 2, \dots, N \end{aligned} \tag{Eq. 4.3}$$

where

$$\begin{aligned} H_i(f) &= \mathcal{F}[h(t) \exp(j2\pi f_i t)] \\ &= H(f - f_i) \end{aligned} \tag{Eq. 4.4}$$

in which $h(t)$ is the impulse response of the narrow bandpass filter and $H(f)$ is the corresponding frequency response, which is usually selected to have a Gaussian form, f_i being the central frequency of the i th narrow bandpass filter.

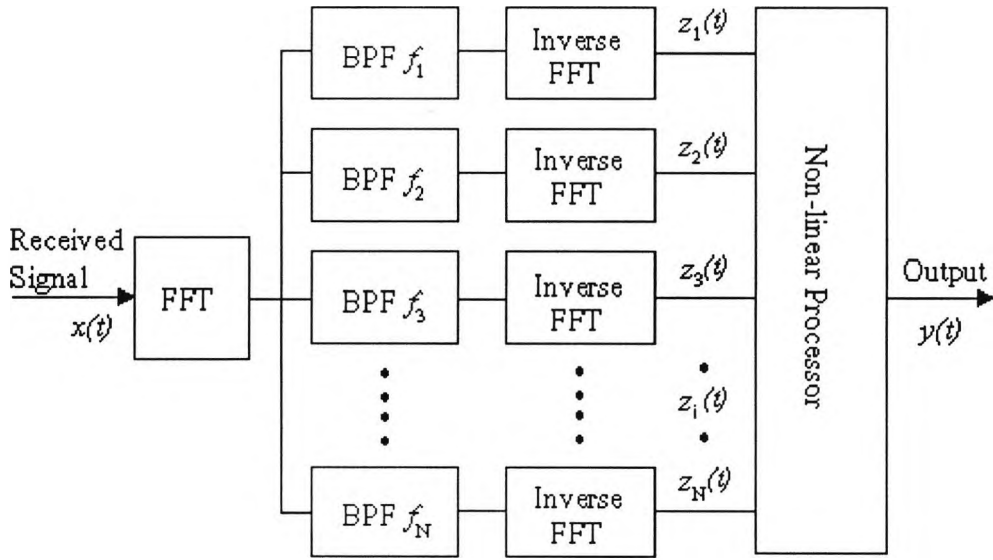


Figure 4.1.1 Split spectrum processing system configuration.

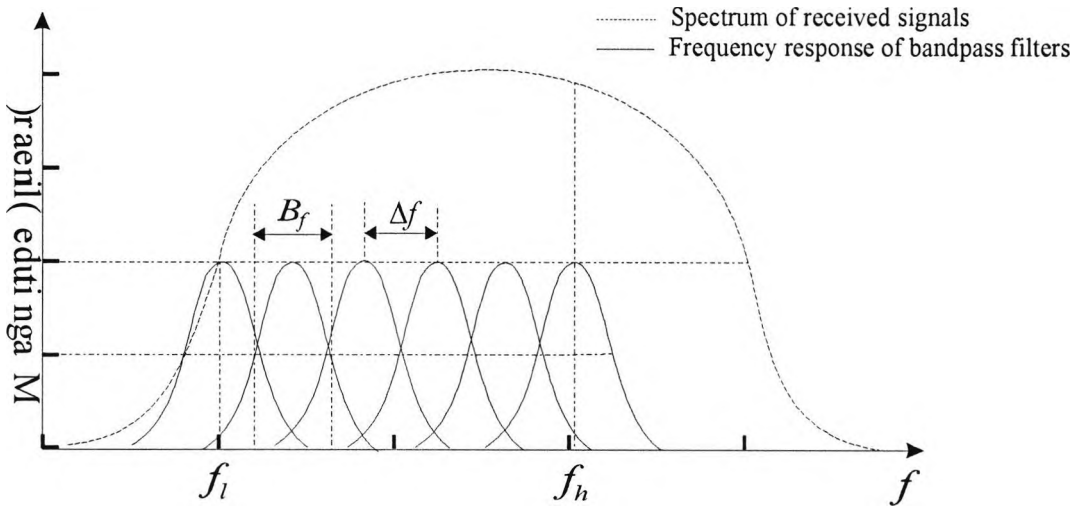


Figure 4.1.2 Frequency domain filtering scheme of split spectrum processing.

Here two different filter configurations will be evaluated. The approach used in the current application applies Gaussian filters that overlap at the half power point. As illustrated in Figure 4.1.2, the half power bandwidth B_f is determined by the number of filters N and the frequency range $f_l \leq f \leq f_h$ where f_l and f_h are the lowest and highest frequencies of interest, respectively. The shape of the Gaussian bandpass filter is given by

$$H(f - f_i) = \exp[-\alpha(f - f_i)^2] \quad \text{Eq. 4.5}$$

where

$$\alpha = -\frac{\ln 0.5}{(B_f / 2)^2} \quad \text{Eq. 4.6}$$

and

$$B_f = \frac{f_h - f_l}{N - 1} \quad \text{Eq. 4.7}$$

Alternatively, in the method of [Karpur, P.] the filter bank is implemented with arbitrarily chosen half power bandwidth B_f but fixed central frequency separation at an interval $\Delta f = 1/T$, where T is the time duration of the input A-scan data. The performance of these two different implementations will be compared later.

The frequency bands generated by the filter bank are transformed back to the time domain to yield the corresponding time domain signals, one for each filter in the bank according to

$$z_i(t) = \mathcal{F}^{-1}[Z(f_i)] \quad i = 1, 2, \dots, N. \quad \text{Eq. 4.8}$$

This set of band limited versions of the original signals can then be further processed by non-linear operations to enhance the wanted signals.

4.1.1 Split spectrum minimisation

Based on the assumption that the echo signal from a defect is less sensitive to the change of the frequency content of the radiated ultrasonic wave than is the grain scattering, the overall signal-to-noise ratio can be enhanced by the split spectrum "minimisation" (SSM) method. In this, the minimum amplitude $y_{\min}(t)$ of the band-limited signal: $z_1(t), z_2(t), \dots, z_i(t), \dots, z_M(t)$ is selected as the final output of the minimisation processor at each time instant t :

$$y_{\min}(t) = \min[z_1(t), z_2(t), \dots, z_i(t), \dots, z_N(t)] \quad \text{Eq. 4.9}$$

Since it has been assumed that the defect signals fluctuate less in the frequency domain than does the grain scattering, the grain noise level would vary more after passing through the narrow bandpass filter bank than does the defect signal. Therefore, the grain noise level would be likely to be reduced more by the minimisation processor than does the defect signal level. As the result, the overall signal-to-noise ratio could be enhanced. The data of interest may partially meet this criterion as discussed in chapter 2, but as demonstrated later (Section 6.3) the method is particularly sensitive to the optimum choice of processing parameters. In fact, if the amplitude of the defect signal at any one of the bandpass filter outputs becomes lower than the minimal amplitude of the grain noise for a chosen

frequency range, the signal-to-noise ratio may even be reduced after the SSM processing.

In an attempt to reduce sensitivity to processing parameters, a cyclic approach has been introduced. In this new approach, the output of the SSM processor is fed back to its input once or twice. Since this iterative adaptation requires fewer filters to give similar signal enhancement, there could be less dependence on the optimum choice of processing parameters than is the case for the conventional, non-cyclic approach. Furthermore as will demonstrated later, with similar signal enhancement to that of the conventional method, the number of filters can be reduced to such an extent that overall processing times are much less, in spite of the iterative procedure.

A further development introduced here has been to retain the original data as one of the sets compared in the minimisation process. This provides a "reference" signal containing undistorted information that should lead to further noise reduction.

4.1.2 Split spectrum polarity thresholding

The minimisation technique described in the previous section uses just amplitude information. As could be anticipated, the same principle can be applied to process the phase related information - here, the polarity (the sign) of the narrow bandpass filtered signals.

The effectiveness of split spectrum polarity thresholding (SSPT) method is based on assumption that the polarity of the echo signal from a defect should be frequency independent. Whereas the signals scattered by grains should be frequency dependent due to the natures of the grain scattering discussed in Chapter

2. Thus, the polarity of the bandpass filter outputs at the time instant of the defect presence should be identical for all bandpass filters if the bandpass filters used here have zero phase shift. Meanwhile, with grain scattering, the polarity of the filter bank outputs would be almost random. So it may be possible to detect the presence or absence of a defect signal by a polarity thresholding operation. However, it should be noted that in reality real defect signals are also scattered by grains. This could result in missing detection and sensitivity to parameter selection as discussed later.

According to the above assumption, if all the narrow bandpass filter outputs: $z_1(t), z_2(t), \dots, z_i(t), \dots, z_N(t)$ have the same polarity then a defect signal is registered and the output signal can be set equal to the input. Otherwise, the output is set to zero, i.e.

$$\begin{aligned}
 y_{PT}(t) &= x(t) && \text{if } z_i(t)z_j(t) > 0 \text{ for all } i, j = 1, 2, \dots, N \\
 &= 0 && \text{otherwise}
 \end{aligned}
 \tag{Eq. 4.10}$$

Polarity thresholding can also be applied in conjunction with minimisation (SSPTM) to achieve further noise reduction. That is

$$\begin{aligned}
 y_{PTM}(t) &= \min[z_1(t), z_2(t), \dots, z_i(t), \dots, z_N(t)] && \text{if } z_i(t)z_j(t) > 0 \text{ for all } i, j = 1, \dots, N \\
 &= 0 && \text{otherwise}
 \end{aligned}
 \tag{Eq. 4.11}$$

The approach adopted here is to use this combined method but with the incorporation of the second development mentioned in Section 4.1.1, namely

retaining the original data as one of the sets to be compared in the polarity thresholding procedure.

4.1.3 SSP parameter selection

It has been shown [Karpur, P., 1987, 1988], [Mohana, P. 1989] [Zhu, Y.] that SSP approaches are sensitive to the optimum choice of processing parameters. In particular the processing frequency range and number of filters must be chosen so that all useful information in the wanted signal is retained, whilst achieving good reduction of the scattering noise. Inappropriate choice of such parameters can result in wanted signals being lost and in some cases it is even possible to enhance the noise rather than the wanted signal. For this reason Karpur and Mohana have investigated an approach whereby the frequency dependence of grain scattering is taken into account in setting the processing frequency range.

As discussed in Chapter 2, and as shown schematically in Figure 4.1.3 for the transducer pulse shapes, target sizes and typical grain size in the current application, it is anticipated that the spectrum of the grain noise will be stronger towards the higher frequencies (Figure 4.1.3(c)) than is the wanted signal spectrum (Figure 4.1.3(b)). Therefore the lower cut-off frequency f_l of the processing range can be set to match that of the echo spectrum received by the wideband transducer as illustrated in Figure 4.1.3(a). Karpur [Karpur, P., 1988], has suggested selection of the upper cut-off frequency f_h by consideration of the way in which average grain size determines the frequency dependence of attenuation due to grain scattering. Of course such an approach requires *a priori* knowledge of the average grain size.

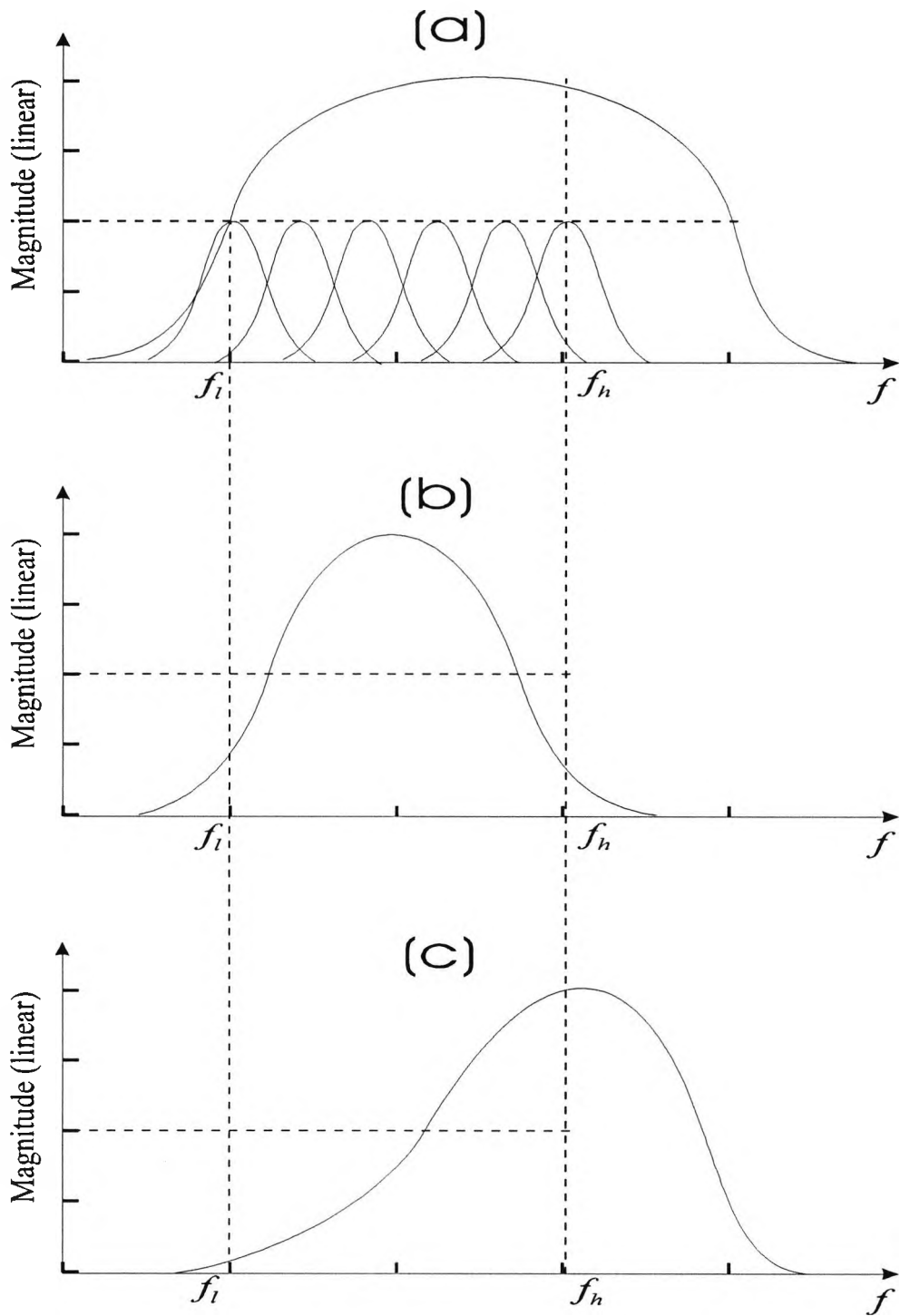


Figure 4.1.3 Schematic graph of power spectra: (a) for a short pulse echo received by a wideband transducer; (b) for a short pulse reflected by a flat bottom hole or the backwall of a test block; (c) for grain scattering.

As is well known (see for instance [Papadakis, E.P., 1968]), the frequency dependence of attenuation can be expressed as

$$A(f) = A_0(f)10^{-\alpha z/20} \quad \text{Eq. 4.12}$$

where $A_0(f)$ is the original unattenuated wave amplitude at frequency f and z is the distance inside the material over which the attenuation occurred. The attenuation coefficient α is given by

$$\alpha = D^3 f^4 S \quad \text{for wavelength } \lambda \gg D, \quad \text{Eq. 4.13}$$

and

$$\alpha = Df^2 \Sigma \quad \text{for wavelength } \lambda \approx D. \quad \text{Eq. 4.14}$$

Here S and Σ are material constants that have been tabulated in the literature [Papadakis, E.P., 1968]. In practice, *a priori* knowledge of the average grain size D is often not easy to obtain and moreover, it could vary with testing location. In attempt to overcome this limitation Karpur [Karpur, P. 1988] has suggested that f_h can be determined empirically by taking a fixed lower frequency and a fixed filter central frequency separation and then increasing the number of SSP filters until the backwall echo is lost in the SSP output. It should be noted that this approach can only be used where the amplitude of the backwall echo is not so large as to saturate the receiving amplifier. Furthermore the procedure is not independent of individual filter bandwidth.

Suppose that an optimal processing frequency range and hence the bandwidth of the SSP filter bank ($f_l \leq B \leq f_h$) has been determined for a given time series of duration T . The sampling frequency is

$$F_s = \frac{N_d}{T},$$

Eq. 4.15

where N_d is the number of data points and the corresponding Nyquist frequency is

$$F_{\max} = \frac{1}{2} F_s$$

Eq. 4.16

The number of independent complex frequency components for N_d real samples is

$$N_f = \frac{1}{2} N_d$$

Eq. 4.17

and the minimum resolvable frequency interval is

$$\begin{aligned} \Delta f_{\min} &= \frac{F_{\max}}{N_f} \\ &= \frac{1}{T} \end{aligned}$$

Eq. 4.18

Karpur suggested [Karpur, P. 1987] that Δf_{\min} is also the optimal central frequency separation between adjacent SSP filters. The influence of using such a fine frequency interval in the current application will be investigated and compared with the half-power-point overlapping approach used here.

If the central frequency separation is taken as Δf_{min} , the total number of filters required to cover the chosen processing frequency bandwidth B becomes

$$N = BT + 1 \tag{Eq. 4.19}$$

However, for SSP with polarity thresholding, the theoretical analysis of Mohana [Mohana, P. 1989] indicated that the optimum number of filters should be taken as the smaller of the values given by Eq. 4.19 or a value calculated (numerically) from

$$SNR_{enh} = \frac{SNR_{out}}{SNR_{in}} = \frac{\left[1 - erf\left(\frac{SNR_{in}}{\sqrt{2N}}\right)^N \right] + \left[1 + erf\left(\frac{SNR_{in}}{\sqrt{2N}}\right)^N \right]}{2^{(N+1)/2}} \tag{Eq. 4.20}$$

where

$$erf(z) = \frac{2}{\sqrt{\pi}} \int_0^z e^{-x^2} dx \tag{Eq. 4.21}$$

and

$$SNR_{in} = \frac{E[s(t)]}{\sqrt{E[n^2(t)]}} = \frac{m}{\sigma_n} \tag{Eq. 4.22}$$

Equations Eq. 4.20 and Eq. 4.21 are obtained under the assumption that the grain noise has a Gaussian distribution with a zero mean and variance σ_n . The expectation $E[*]$ is taken over many sampling channels corresponding to the outputs from each SSP filter at a time instant within the duration of the wanted signal. It should be noted that this approach requires *a priori* knowledge of SNR_{in} which is usually unknown in practice.

4.2 Adaptive filtering

An alternative approach that has been used in a related problem in sonar beamforming systems [Yan, A.] is to make use of adaptive filtering to enhance the signal-to-noise ratio by exploring both the spatial and time domain differential features between the signal and noise received by a sensor array.

It is noteworthy that a widely used signal enhancement technique in practical NDT, called linear spatial averaging [Kraus, S.], can be viewed as a primitive type of beamforming technique, known as delay-and-sum beamforming. More specifically, linear spatial averaging is a special case of delay-and-sum beamforming with zero delay for all input channels. The usefulness of the linear spatial averaging method depends on the defect echo signals in adjacent A-scans being more closely correlated than is the corresponding grain noise. Also as discussed in Section 2.1, the target signals tend to have longer correlation length in the time domain than that of the grain scattering. Where these differential features do exist, it should be possible to develop an adaptive filtering approach to preferentially enhance the defect signals by making use of the difference in the way in which the wanted target signal and the unwanted grain noise vary with changes in the position of the transducer. The objective of the processing is of course to enhance the correlated signals present in adjacent or nearby A-scans but suppress the less correlated noise. Furthermore, the grain noise and the defect signal are often non-stationary in both time and space domain, and therefore adaptive methods can be particularly advantageous.

4.2.1 Adaptive systems

In general, the essential principle of an adaptive system is that it adjusts itself to fit different conditions and/or a time-varying environment without requiring, *a priori*, detailed, or even statistical knowledge of these.

Over past decades, adaptive systems have been successfully developed in diverse scientific and engineering disciplines. They offer attractive solutions in many applications such as: adaptive antennae and beamformers, adaptive system identification and inverse control, adaptive filtering and interference cancelling, biomedical electronics [Widrow, B., 1975, 1985], and ultrasonic non-destructive testing [Donohue, K.D., 1993][Challis, R. E., 1995], etc., etc.

Depending on whether the adaptive process is controlled by the knowledge acquired from its input or output, it can be classified in terms of open-loop and closed-loop adaption, respectively. In the open-loop system, the adjustment of the adaptive process is controlled by algorithms using information derived from the inputs and/or from environmental characteristics. In a closed-loop system, the adaptive process is controlled by algorithms using the information obtained from its output - so called performance feedback control.

Generally speaking, the closed-loop approach has the advantage of being widely applicable where analytic synthesis is either impossible or difficult to obtain due to the systems being non-linear or time-varying. This feature could make it a suitable choice for the current application. However as might be anticipated, this

does not imply that closed-loop adaptive systems are trouble free. In fact there is no guarantee that the adaptation process will always converge to a global minimum. In fact, the performance function may not have a global minimum, or even if it does, the adaptation process may converge to other local minima. Even though there are these possibilities, closed-loop adaptation is still very powerful under certain conditions. In general, its performance is ultimately dependent on the structure of the adaptive system; the shape of the performance surface; the start point of the adaptation process and the algorithm used for searching for the global minimum, if it exists. Each of these details will be discussed in turn in the following sections.

4.2.2 FIR Adaptive filtering and noise cancelling

The adaptive filter described here is developed from the widely used technique of adaptive noise cancellation [Widrow, B., 1975]. As shown in Figure 4.2, the basic system is a dual-input, closed-loop system. The coherent noise n in the primary input $d = s + n$ can be suppressed provided that a correlated (but perhaps distorted version of the noise n) reference noise signal $x = n'$ is available. The objective of the adaptive processor is to produce an output y that resembles n as closely as possible, so that it will cancel the corresponding noise component n in the signal d . The overall output e will then closely resemble the desired signal s . In this case, the performance criterion is the mean square value of e .

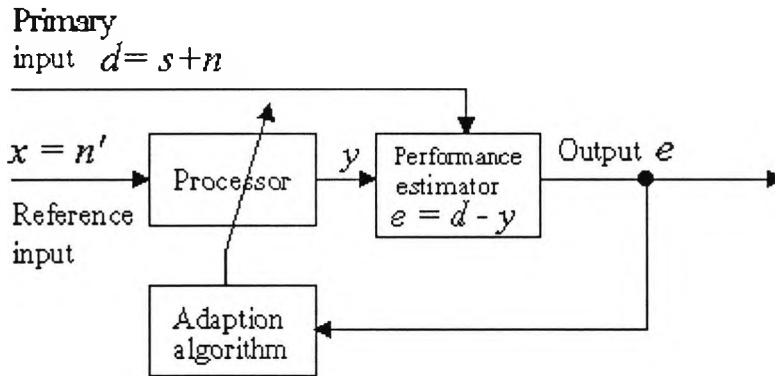


Figure 4.2.1 Schematic configuration of a closed-loop adaptive noise canceller.

Since ultrasonic grain noise varies with transducer position, it is not possible to obtain a reference signal consisting of noise alone, where the noise is correlated with that present in the signal containing a target echo. This has precluded straightforward application of adaptive noise cancelling techniques for the current application. However, if the echo signals present in two A-scans obtained by laterally moving the transducer by less than its beam width, are more closely correlated than is the corresponding grain noise, it is possible to adapt the principle of adaptive noise cancelling to enhance signal-to-noise ratio.

Consider the filter configuration shown in Figure 4.2.2, where $d(k)$ is the primary input, and $x(k)$ is the reference input. As is usual, we assume that the primary input, $d(k)$, can be written as

$$d(k) = s(k) + n(k)$$

Eq. 4.23

where $s(k)$ and $n(k)$ are the target echo and the grain noise, respectively. Assume that $s(k)$, $n(k)$ and $y(k)$ are all statistically stationary, and $n(k)$ is white noise with mean power σ_n^2 . The mean square error is given by

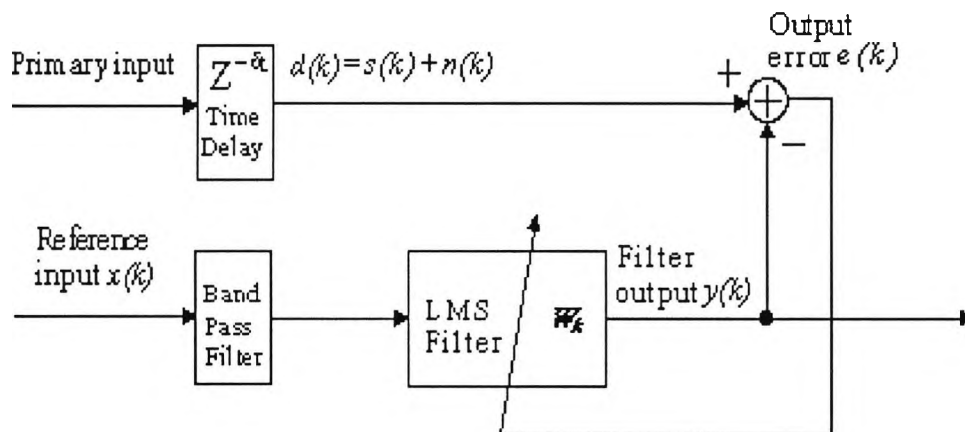


Figure 4.2.2 Outline of the adaptive filter configured with a bandpass filtered reference input. The two input channels are from adjacent A-scans.

$$\begin{aligned}
 E[e^2(k)] &= E[(d(k) - y(k))^2] \\
 &= E[(((s(k) - y(k)) + n(k))^2)] \\
 &= E[(s(k) - y(k))^2 + n^2(k) + 2n(k)(s(k) - y(k))]
 \end{aligned}$$

Eq. 4.24

Suppose $n(k)$ is uncorrelated with $s(k)$ and $y(k)$. Then,

$$\begin{aligned}
 E[e^2(k)] &= E[(s(k) - y(k))^2 + n^2(k)] \\
 &= E[(s(k) - y(k))^2] + \sigma_n^2
 \end{aligned}$$

Eq. 4.25

When the filter is optimised, the mean-square error will be a minimum, i.e.

$$\min\{E[e^2(k)]\} = \min\{E[(s(k)-y(k))^2]\} + \sigma_n^2$$

Eq. 4.26

Since the possible minimum of $E[(s(k)-y(k))^2]$ is zero, the smallest possible mean-square error is

$$E[e^2(k)]_{\min} = \sigma_n^2$$

Eq. 4.27

If this is achieved, the filter output will be completely noise free, i.e. $y(k)=s(k)$. However, in reality the mean-square error will more likely be minimised close to σ_n^2 rather than exactly equal to σ_n^2 . Therefore, the filter output will not be completely noise free but the overall signal-to-noise ratio at the output will be enhanced.

The above analysis shows that the performance criterion of the adaptation process is the output mean-square error MSE. The way in which the MSE varies with filter coefficients can be represented by the performance surface. The objective of an adaptive algorithm is then to search for a global minimum on the performance surface. Obviously two questions arise:

- (i) Does a global minimum exist?
- (ii) Are there any local minima?

To answer these fundamental questions, detailed analysis of the characteristics of the performance surface is required [see for instance Widrow, B., 1985]. Here only the main features of performance surface of FIR adaptive filter applied in the current application will be briefly reviewed.

For convenience, the reference input signal and the filter weight coefficients can be written in vector notation defined as:

$$\mathbf{X}^T(k) = [x(k), x(k-1), \dots, x(k-L)], \quad \text{Eq. 4.28}$$

and

$$\mathbf{W}_k^T = [w_k(0), w_k(1), \dots, w_k(L)]. \quad \text{Eq. 4.29}$$

The FIR filter output can be written as:

$$\begin{aligned} y(k) &= \mathbf{W}_k^T \mathbf{X}(k) \\ &= \mathbf{X}^T(k) \mathbf{W}_k \end{aligned} \quad \text{Eq. 4.30}$$

The performance function of the FIR adaptive filter can be expressed by taking the expectation operation over the discrete time index k i.e.

$$\begin{aligned} \text{MSE} &= \xi \\ &= E[e^2(k)] \\ &= E\{[d(k) - \mathbf{X}^T(k) \mathbf{W}_k]^2\} \\ &= E[d^2(k)] - 2\mathbf{P}_k^T \mathbf{W}_k + \mathbf{W}_k^T \mathbf{R}_k \mathbf{W}_k \end{aligned} \quad \text{Eq. 4.31}$$

where

$$\mathbf{R}_k = E[\mathbf{X}(k) \mathbf{X}^T(k)] \quad \text{Eq. 4.32}$$

and

$$\mathbf{P}_k = E[d(k)\mathbf{X}^T(k)]$$

Eq. 4.33

It is seen from the Eq. 4.31 that it contains only the first and second order power of \mathbf{W}_k . Thus, it is a quadratic function of the weight vector \mathbf{W}_k . It can be viewed as a hyper-parabolic surface in a $L+2$ dimensional space spanned by $L+1$ components of \mathbf{W}_k plus one dimension in mean-square error ξ . In general, the performance surface so defined must be a concave upward surface, since the power of a real, physical error signal must be always positive. Also there is only one minimum on a quadratic performance surface, and this guarantees an optimum solution.

It should be noted that the quadratic performance surface is an important feature attributable to the non-recursive structure of the FIR filter defined in Eq. 4.30. In contrast, the performance surface of a recursive system is generally nonquadratic and may even have local minima [Widrow, B., 1985]. However, according to the definition Eq. 4.31, the performance surface and therefore its minima may change or move with time in the performance space, if the input signals $x(k)$ and/or $d(k)$ are nonstationary and have time-varying statistical characteristics. Since it is anticipated that the current data may exhibit such behaviour, the adaptive approach to be adopted here should offer improved performance compared to a conventional fixed filter.

4.2.3 NLMS adaptive algorithm

After defining the performance surface, the goal of an adaptive algorithm is of course to search for the minimum of the performance surface. In searching the minimum on a quadratic performance surface, a sensible consideration is to search along the steepest descent direction. That is in the direction of negative gradient of the performance surface. Although this may be not exactly in the direction toward

the minimum, unless the gradient is taken on one of the principal axes of the surface, it does guarantee the convergence process is approaching toward the minimum. Therefore it can be still an optimal choice for the current application, as the convergence process will be guaranteed without requiring any supervision during the processing.

The gradient of mean square error performance surface can be conveniently defined as a column vector [Widrow, B., 1985]

$$\begin{aligned}
 \nabla \xi_k &\equiv \frac{\partial \xi_k}{\partial \mathbf{W}_k} \\
 &= \left[\frac{\partial \xi_k}{\partial W_k(0)}, \frac{\partial \xi_k}{\partial W_k(1)}, \dots, \frac{\partial \xi_k}{\partial W_k(L)} \right]^T \\
 &= 2\mathbf{R}_k \mathbf{W}_k - 2\mathbf{P}_k
 \end{aligned}$$

Eq. 4.34

For a quadratic performance surface, the minimum can be obtained by setting the gradient to be zero:

$$\begin{aligned}
 \nabla \xi_k &= 2(\mathbf{R}_k \mathbf{W}_k - \mathbf{P}_k) \\
 &= 0
 \end{aligned}$$

Eq. 4.35

If the \mathbf{R}_k is non-singular, the optimal weight vector \mathbf{W}'_k will be

$$\mathbf{W}'_k = \mathbf{R}_k^{-1} \mathbf{P}_k$$

Eq. 4.36

This is the vector form of the well known Wiener-Hopf equation.

Although the Wiener-Hopf equation gives an explicit, analytical expression for the optimal weight vector \mathbf{W} , its direct application is limited due to the required expectation of the autocorrelation matrix \mathbf{R}_k and the cross-correlation vector \mathbf{P}_k , which usually are unknown *a priori*. This means that it is not straightforward to calculate \mathbf{W} and therefore alternative approaches have been developed. One of the most successful methods is the least mean square (LMS) algorithm proposed by Widrow and his co-workers.

Instead of estimating the gradient of the performance surface from the statistic expectation of the squared error $\xi_k = E[e^2(k)]$, the LMS algorithm takes the instantaneous squared error $e^2(k)$ itself as an estimate of ξ_k

$$\begin{aligned}\xi'_k &= e^2(k) \\ &= [d(k) - \mathbf{X}^T(k)\mathbf{W}_k]^2\end{aligned}\tag{Eq. 4.37}$$

Thus the gradient of the performance surface can be approximated by

$$\begin{aligned}\nabla_{\xi'_k} &= \frac{\partial e^2}{\partial \mathbf{W}_k} \\ &= -2e(k)\mathbf{X}(k).\end{aligned}\tag{Eq. 4.38}$$

In fact it is easy to show that this is an unbiased estimate, since if we estimate the gradient with any given \mathbf{W}_k , the expectation of Eq. 4.38 will become

$$\begin{aligned}E[\nabla_{\xi'_k}] &= -2E[e(k)\mathbf{X}(k)], \\ &= -2E[d(k)\mathbf{X}(k) - \mathbf{X}(k)\mathbf{X}^T(k)\mathbf{W}_k], \\ &= 2(\mathbf{R}_k\mathbf{W}_k - \mathbf{P}_k), \\ &= \nabla_{\xi_k}.\end{aligned}\tag{Eq. 4.39}$$

This suggests that $-\nabla \xi'_k$ can be used as a suitable instantaneous estimate of the steepest descent direction to optimise the weight vector iteratively, i.e.

$$\begin{aligned}\mathbf{W}_{k+1} &= \mathbf{W}_k - \mu \nabla \xi_k, \\ &= \mathbf{W}_k + 2\mu e(k)\mathbf{X}(k),\end{aligned}\tag{Eq. 4.40}$$

where μ is a step size of the iteration that regulates the speed and stability of the adaptive process. In general, it has been shown [Widrow, B., 1985] that the convergence of the adaptive process can be guaranteed only if μ is bounded within the range

$$0 < \mu < \frac{1}{\text{tr}[\mathbf{R}]}\tag{Eq. 4.41}$$

For a transversal filter this becomes

$$0 < \mu < \frac{1}{(L+1)\sigma_x^2},\tag{Eq. 4.42}$$

where σ_x^2 is the average input signal power and L is the filter length. This suggests that the step size should be taken inversely proportional to the input signal power.

Thus if we define a normalised step size μ_n as

$$\mu_n = \mu(L+1)\sigma_x^2(k),\tag{Eq. 4.43}$$

where the input signal power can be estimated on-line for a nonstationary process by

$$\sigma_x^2(k) = \alpha x^2(k) + (1-\alpha)\sigma_x^2(k-1),\tag{Eq. 4.44}$$

where $\sigma_x^2(k)$ is a time varying estimation of the average input signal power and α is a "fading factor" introduced to reduce the influence of the past inputs. Inspection of Eq. 4.44 shows that the fading factor α must lie in the range $0 < \alpha < 1$. Replacing the convergence step size μ in Eq. 4.40 with the normalised μ_n will lead to the so-called normalised LMS algorithm (NLMS). The convergence of this will be guaranteed if $0 < \mu_n < 1$. It has been shown that the speed of convergence of the NLMS algorithm can be considerably improved over that of the LMS method [Tarrab, M. 1988].

The adaptive iteration can be initialised with the filter weight vector W_k set to zero and $\sigma_x(0)$ set to the average input signal power. The number of filter coefficients L is often required to be set empirically to suit the data.

It should be noted that since the steepest descent method may not converge exactly in the direction toward the minimum, it may not necessarily give the fastest convergence, but its convergence on a quadratic performance surface is guaranteed. Alternative methods such as the recursive least squares (RLS) and Kalman filter algorithms can give faster convergence. However they may inherently have numerical instability problems, due to their recursive structures and nonquadratic performance surfaces. Their convergence therefore may not be guaranteed [Widrow, B., 1985]. For these reasons, if the convergence speed of the NLMS is sufficient for the application in hand, the NLMS algorithm should be still the algorithm of first choice in terms of computational efficiency.

Although the convergence of the NLMS algorithm can be guaranteed, the speed of convergence is also a very important factor in the present application. Since our objective is to enhance the correlated signals masked by somewhat less correlated noise, the adaptive filter must converge quickly enough to follow the

space and time variation of the cross correlation of the input signals. In order to monitor the time response of the adaptive filter in such a nonstationary environment, a time domain "gain" of the filter is defined as

$$\begin{aligned} g(k) &= \mathbf{W}_k^T \cdot \mathbf{W}_k \\ &= \|\mathbf{W}_k\|^2 \end{aligned}$$

Eq. 4.45

As will be demonstrated later, the convergence speed can be checked by plotting $g(k)$ for data containing a known target. Such a plot can also be useful to indicate whether parameters are optimised for signal enhancement.

4.2.4 Adaptive filter with bandpass filtered reference input

As discussed in the above analysis, if the adaptive filtering method is to be useful, the reference input $x(k)$, should contain a signal component correlated with $s(k)$, but the noise component in the reference input should be less correlated with either $s(k)$ or $n(k)$. This can be achieved to a certain extent by laterally moving the transducer by less than its beam width. The effectiveness of this approach is based on the disparity in the spatial dependence of the received echo waveform from grains and flaws. In fact as is well known the differential impedance at a defect boundary is usually much greater than that at a grain boundary and this is certainly the case here where the defects are air-filled flat-bottomed holes. Thus the cross-correlation between the defect echoes in the two input channels would be higher than that of the corresponding grain scattering even for a grain with similar dimension and geometry to that of the defect. Furthermore, it may be possible to decorrelate the grain noise by making use of the frequency characteristics of the scattering as argued in Chapter 2. Based on this consideration, an attempt has been made to further decorrelate the grain noise with respect to the primary input by

applying a bandpass filter to the reference input channel, as shown in Figure 4.2.2. A linear phase filter with a filter length L_b of about 20 was used - with a Hamming window, but it is likely that any smoothing function would be acceptable for the current application. As shown in Figure 4.2.2, a time delay $\delta t = L_b \Delta t / 2$ is introduced into the primary input to compensate for the delay in the bandpass filter, thereby retaining the correlation between the wanted signals in the two input channels. Here Δt is the sampling time interval. The effectiveness of this extension will be evaluated later using A-scans containing a real defect signal.

5. Optimal Time-space array processing and image enhancement techniques

In the previous chapter, some one-dimensional signal processing techniques were explored. These were based on the time-, spatial- or frequency-domain characteristics of the grain noise and the defect signals. In particular, differences in the spatial variation of the cross correlation of defect signals and noise were exploited by an adaptive filtering method. Alternative, two-dimensional, approaches to exploit such differences further are: time-space array filtering having either a minimum-noise distortionless response (MNDR) or a minimum-variance distortionless response (MVDR), and adaptive Wiener filtering methods. These are treated in turn in the following two sections.

5.1 Optimal Time-space array processing

5.1.1 Time-space vector representation of a line A-scan array

Suppose a given linear A-scan array contains M A-scan time series with time duration T and bandwidth W . In accordance with the sampling theorem, the whole ultrasound field covered by the linear A-scan array can be reconstructed from $2TWM$ samples. This time-space sampling series can be expressed as a $2TWM$ dimensional vector:

$$\mathbf{x}^T = [x_1(0), x_1(1), \dots, x_1(N-1); x_2(0), x_2(1), \dots, x_M(N-1)] \quad \text{Eq. 5.1}$$

which contains M A-scans with $N = 2TW$ samples of each.

The discrete Fourier transform of the \mathbf{x} will be a complex vector:

$$\mathbf{X}^T = [\mathbf{X}^T(f_1), \mathbf{X}^T(f_2), \dots, \mathbf{X}^T(f_l), \dots, \mathbf{X}^T(f_{N/2})]$$

Eq. 5.2

where

$$\mathbf{X}^T(f_l) = [X_1(f_l), X_2(f_l), \dots, X_M(f_l)]$$

Eq. 5.3

and

$$X_i(f_l) = \sum_{k=0}^{N-1} x_i(k) e^{-j2\pi f_l k},$$

$$i = 1, 2, \dots, M;$$

$$l = 1, 2, \dots, \frac{N}{2}.$$

Eq. 5.4

It should be noted that since $x_i(k)$ is a real process, its Fourier components must be complex conjugate symmetrical. Thus there are only $N/2$ independent Fourier components for the N samples of each A-scan trace.

Consider the input signal vector \mathbf{x} is comprised of a defect signal \mathbf{s} and grain scattering noise \mathbf{n} with zero mean, i.e.

$$\mathbf{x} = \mathbf{s} + \mathbf{n}$$

Eq. 5.5

where

$$\mathbf{s}^T = [s_1(0), s_1(1), \dots, s_1(N-1); s_2(0), s_2(1), \dots, s_M(N-1)] \quad \text{Eq. 5.6}$$

and

$$\mathbf{n}^T = [n_1(0), n_1(1), \dots, n_1(N-1); n_2(0), n_2(1), \dots, n_M(N-1)] \quad \text{Eq. 5.7}$$

Accordingly, their discrete Fourier transforms (DFT) are

$$\mathbf{S}^T = [\mathbf{S}^T(f_1), \mathbf{S}^T(f_2), \dots, \mathbf{S}^T(f_1), \dots, \mathbf{S}^T(f_{N/2})] \quad \text{Eq. 5.8}$$

and

$$\mathbf{N}^T = [\mathbf{N}^T(f_1), \mathbf{N}^T(f_2), \dots, \mathbf{N}^T(f_1), \dots, \mathbf{N}^T(f_{N/2})] \quad \text{Eq. 5.9}$$

If the experiment is conducted under the condition that the plane wave approximation can be applied, the target signal vector can be decomposed as:

$$\mathbf{S}(f_i) = S(f_i)\mathbf{u}(f_i) \quad \text{Eq. 5.10}$$

where $S(f_i)$ is the frequency spectrum of the signal \mathbf{s} and $\mathbf{u}(f_i)$ is the incident signal directional vector or steering vector given by

$$\mathbf{u}^T(f_i) = [1, \dots, e^{-j2\pi f_i \tau_i}, \dots, e^{-j2\pi f_i \tau_{M-1}}] \quad \text{Eq. 5.11}$$

where τ_i is the arrival time of the received signal at the i th A-scan transducer position relative to the first A-scan trace.

The corresponding covariance spectrum matrix for the received signal, \mathbf{P} , and scattering noise, \mathbf{Q} are $(MN/2) \times (MN/2)$ dimensional, i.e.

$$\mathbf{P} = E[\mathbf{X}\mathbf{X}^+] \tag{Eq. 5.12}$$

and

$$\mathbf{Q} = E[\mathbf{N}\mathbf{N}^+] \tag{Eq. 5.13}$$

where the superscript '+' denotes Hermitian conjugation, i.e. transposition combined with the complex conjugate operation.

It can be shown that for a stationary process, its DFT forms a Karhunen-Loeve expansion [Van Trees, H.L.]. Thus the Fourier coefficients for different frequencies are uncorrelated. Consequently the corresponding covariance matrix defined by Eq. 5.12 and Eq. 5.13 are blocking diagonal, i.e.

$$\mathbf{P} = \begin{pmatrix} \mathbf{P}(f_1) & 0 & \dots & \dots & \dots & 0 \\ 0 & \mathbf{P}(f_2) & 0 & \dots & \dots & \cdot \\ \cdot & \dots & \dots & \dots & \dots & \cdot \\ \cdot & \dots & 0 & \mathbf{P}(f_i) & 0 & \cdot \\ \cdot & \dots & \dots & \dots & \dots & 0 \\ 0 & \dots & \dots & \dots & 0 & \mathbf{P}(f_{N/2}) \end{pmatrix} \tag{Eq. 5.14}$$

in which $\mathbf{P}(f_i)$ is a $M \times M$ dimensional sub-matrix:

$$\mathbf{P}(f_i) = E[\mathbf{X}(f_i)\mathbf{X}^+(f_i)] \tag{Eq. 5.15}$$

and the same for \mathbf{Q} :

$$\mathbf{Q} = \begin{pmatrix} \mathbf{Q}(f_1) & 0 & \dots & \dots & \dots & 0 \\ 0 & \mathbf{Q}(f_2) & 0 & \dots & \dots & \dots \\ \dots & \dots & \dots & \dots & \dots & \dots \\ \dots & \dots & 0 & \mathbf{Q}(f_l) & 0 & \dots \\ \dots & \dots & \dots & \dots & \dots & 0 \\ 0 & \dots & \dots & \dots & 0 & \mathbf{Q}(f_{N/2}) \end{pmatrix}$$

Eq. 5.16

where

$$\mathbf{Q}(f_l) = E[\mathbf{N}(f_l)\mathbf{N}^+(f_l)].$$

Eq. 5.17

It should be noted that if the signal is nonstationary over the time duration of the processing cell, then a nonvanishing off-diagonal sub-covariance matrix can be expected. This fact suggests that in order to simplify the computations, we should properly select the processing cell length so that the signal over the time duration can be assumed as stationary.

5.1.2 Minimum-noise distortionless response matrix filtering

Minimum-noise distortionless response filtering is an optimal rule based processing method that can be viewed as an open-loop adaptive filter. As shown in Figure 5.1, a matrix filter is applied to process M inputs of a linear array to extract the wanted signals by exploiting both time and space characteristics of the input data. More specifically, the method is based on the rule of minimising the noise output under the constraint of a distortionless response [Lim, J.S.]. For

convenience the method is reviewed here, before developing an analysis to aid in its evaluation.

Suppose the processing cell has been appropriately selected so that the covariance matrix of the received signal and the scattering noise are blocking diagonal (see Eqs. 5.14 -17). Thus the output noise intensity at frequency f_i and output channel i can be written as

$$\mathbf{H}_i^+(f_i)\mathbf{N}(f_i)\mathbf{N}^+(f_i)\mathbf{H}_i(f_i) = \mathbf{H}_i^+(f_i)\mathbf{Q}(f_i)\mathbf{H}_i(f_i) \quad \text{Eq. 5.18}$$

where $\mathbf{H}_i(f_i)$ is the i th column vector of the sub-matrix filter transfer function at frequency f_i . Under plane wave conditions, the distortionless constraint can be expressed as:

$$\mathbf{H}_i^+(f_i)\mathbf{S}(f_i) = S(f_i) \quad \text{Eq. 5.19}$$

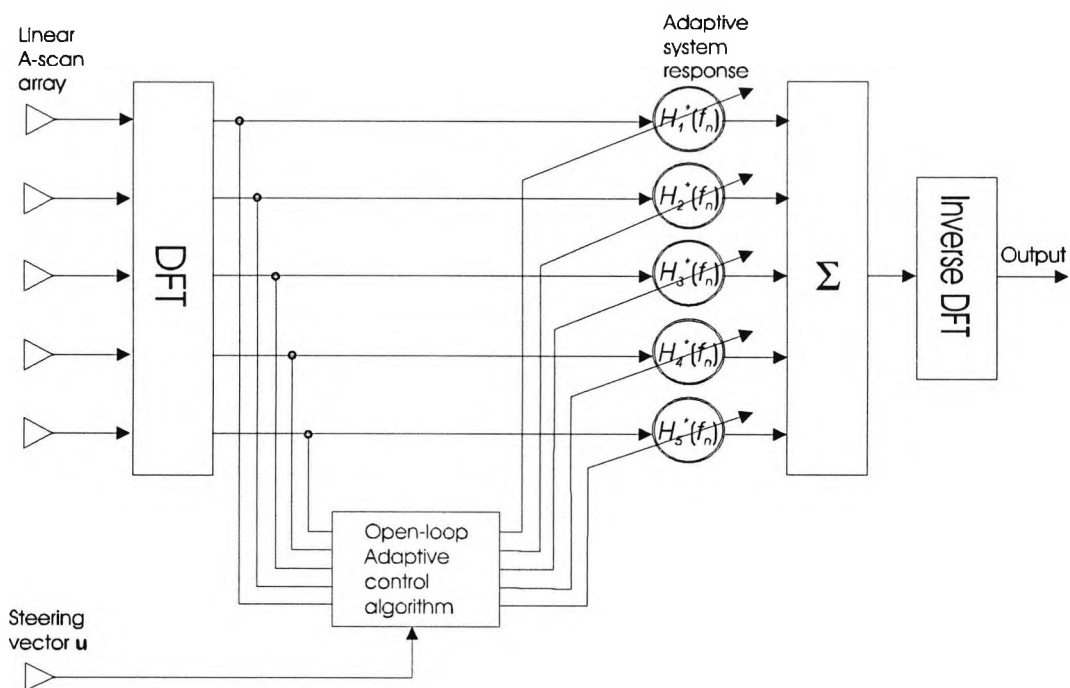


Figure 5.1 Adaptive MNDR and MVDR filter system configuration.

or

$$\mathbf{H}_i^+(f_i)\mathbf{u}(f_i) = 1 \quad \text{Eq. 5.20}$$

This constraint explicitly states that if just the signal is present in the input and no noise exists, then the output signal should be an exact replica of the input signal, with no distortion. This condition can be also rewritten in an equivalent form:

$$\mathbf{H}_i^+(f_i)\mathbf{u}(f_i) + \mathbf{u}^+(f_i)\mathbf{H}_i(f_i) = 2. \quad \text{Eq. 5.21}$$

Using the Lagrangian multiplier method, we can express the above optimal rule as a constrained minimisation problem:

$$\mathcal{L}[\mathbf{H}_i(f_i)] = \mathbf{H}_i^+(f_i)\mathbf{Q}(f_i)\mathbf{H}_i(f_i) + \lambda[\mathbf{H}_i^+(f_i)\mathbf{u}(f_i) + \mathbf{u}^+(f_i)\mathbf{H}_i(f_i)] \quad \text{Eq. 5.22}$$

Taking the variation of Eq. 5.22 with respect to $\mathbf{H}_i(f_i)$ and setting the result to be zero, we have

$$\begin{aligned} \delta\mathcal{L}[\mathbf{H}_i(f_i)] &= \delta\mathbf{H}_i^+(f_i)\mathbf{Q}(f_i)\mathbf{H}_i(f_i) + \mathbf{H}_i^+(f_i)\mathbf{Q}(f_i)\delta\mathbf{H}_i(f_i) \\ &\quad + \lambda[\delta\mathbf{H}_i^+(f_i)\mathbf{u}(f_i) + \mathbf{u}^+(f_i)\delta\mathbf{H}_i(f_i)] \\ &= 0 \end{aligned} \quad \text{Eq. 5.23}$$

thus

$$\delta\mathbf{H}_i^+(f_i)[\mathbf{Q}(f_i)\mathbf{H}_i(f_i) + \lambda\mathbf{u}(f_i)] + [\mathbf{H}_i^+(f_i)\mathbf{Q}(f_i) + \lambda\mathbf{u}^+(f_i)]\delta\mathbf{H}_i(f_i) = 0 \quad \text{Eq. 5.24}$$

A sufficient solution that can always satisfy Eq. 5.24 is

$$\mathbf{Q}(f_i)\mathbf{H}_i(f_i) + \lambda\mathbf{u}(f_i) = 0,$$

Eq. 5.25

therefore

$$\mathbf{H}_i(f_i) = -\lambda\mathbf{Q}^{-1}(f_i)\mathbf{u}(f_i).$$

Eq. 5.26

The multiplier λ can be determined from the constrain condition Eq. 5.20 and Eq. 5.26

$$\lambda = \frac{-1}{\mathbf{u}^+(f_i)\mathbf{Q}^{-1}(f_i)\mathbf{u}(f_i)}$$

Eq. 5.27

Thus the i th column vector of the optimal matrix filter transfer function can be expressed as:

$$\mathbf{H}_i(f_i) = \frac{\mathbf{Q}^{-1}(f_i)\mathbf{u}(f_i)}{\mathbf{u}^+(f_i)\mathbf{Q}^{-1}(f_i)\mathbf{u}(f_i)}.$$

Eq. 5.28

The filtered i th channel output waveform spectrum can be found from

$$\begin{aligned} Y_i(f_i) &= \mathbf{H}_i^+(f_i)\mathbf{X}(f_i) \\ &= \frac{\mathbf{u}^+(f_i)\mathbf{Q}^{-1}(f_i)\mathbf{X}(f_i)}{\mathbf{u}^+(f_i)\mathbf{Q}^{-1}(f_i)\mathbf{u}(f_i)}, \\ l &= 1, 2, \dots, N/2 \\ i &= 1, 2, \dots, M \end{aligned}$$

Eq. 5.29

and the corresponding time domain waveform can be obtained by the inverse DFT of the estimated waveform spectrum:

$$y_i(k) = \frac{1}{N} \sum_{l=-N/2}^{N/2} Y_i(f_l) e^{j2\pi f_l k},$$

$$k = 0, 1, 2, \dots, N-1.$$

$$i = 1, 2, \dots, M.$$

Eq. 5.30

It is readily shown that above result is equivalent to the maximum likelihood estimation under the condition where signals present in zero mean Gaussian background noise with joint probability distribution function (PDF) of \mathbf{X}

$$P(\mathbf{X}) = \prod_{l=1}^{N/2} A e^{-[\mathbf{X}(f_l) - \mathbf{S}(f_l)]^+ \mathbf{Q}^{-1}(f_l) [\mathbf{X}(f_l) - \mathbf{S}(f_l)]}$$

Eq. 5.31

The maximum likelihood estimation of the deterministic signal $\mathbf{S}(f_l)$ can be obtained by maximising the PDF $P(\mathbf{X})$. This is equivalent to maximising the logarithm of the PDF $P(\mathbf{X})$

$$\begin{aligned} \delta \ln P(\mathbf{X}) &= \delta \{ [\mathbf{X}(f_l) - \mathbf{S}(f_l)]^+ \mathbf{Q}^{-1}(f_l) [\mathbf{X}(f_l) - \mathbf{S}(f_l)] \} \\ &= -\delta \mathbf{S}(f_l)^+ \mathbf{Q}^{-1}(f_l) [\mathbf{X}(f_l) - \mathbf{S}(f_l)] - [\mathbf{X}(f_l) - \mathbf{S}(f_l)]^+ \mathbf{Q}^{-1}(f_l) \delta \mathbf{S}(f_l) \\ &= -\delta S(f_l)^* \mathbf{u}^+(f_l) \mathbf{Q}^{-1}(f_l) [\mathbf{X}(f_l) - S(f_l) \mathbf{u}(f_l)] - \delta S(f_l) [\mathbf{X}(f_l) \\ &\quad - S(f_l) \mathbf{u}(f_l)]^+ \mathbf{Q}^{-1}(f_l) \mathbf{u}(f_l) \\ &= 0 \end{aligned}$$

Eq. 5.32

A sufficient solution to satisfy Eq. 5.32 is

$$\mathbf{u}^+(f_l)\mathbf{Q}^{-1}(f_l)\mathbf{X}(f_l) = S(f_l)\mathbf{u}^+(f_l)\mathbf{Q}^{-1}(f_l)\mathbf{u}(f_l) \quad \text{Eq. 5.33}$$

Thus once again we have

$$\begin{aligned} S_{ML}(f_l) &= \mathbf{H}_i^+(f_l)\mathbf{X}(f_l) \\ &= \frac{\mathbf{u}^+(f_l)\mathbf{Q}^{-1}(f_l)\mathbf{X}(f_l)}{\mathbf{u}^+(f_l)\mathbf{Q}^{-1}(f_l)\mathbf{u}(f_l)} \\ & \quad l = 1, 2, \dots, N/2. \end{aligned} \quad \text{Eq. 5.34}$$

which is the same as Eq. 5.29. According to this analysis, a maximum likelihood estimation based ultrasonic signal processing method proposed recently by [Donohue, K.D., 1992] can be viewed as an one-dimensional form of Eq. 5.34. Obviously, the one-dimensional processing can not make use of the spatial differential features between the target signal and grain noise but the two-dimensional array processing proposed here does make use of such information.

5.1.3 Minimum-noise distortionless response matrix filter: Performance

To gain some insight of the potential performance of the minimum-noise distortionless response array processing method, it is convenient to make some simplifying assumptions concerning the nature of the data so that a theoretical analysis can be developed.

Let the input signal spectrum be denoted by $S_{in}(f)$. Then the power spectrum of the signal input to the matrix filter is

$$\begin{aligned}\mathbf{S}_{in}^+(f_l)\mathbf{S}_{in}(f_l) &= S_{in}^2(f_l)\mathbf{u}^+(f_l)\mathbf{u}(f_l) \\ &= MS_{in}^2\end{aligned}\tag{Eq. 5.35}$$

Suppose the scattering noise is uncorrelated between different traces of the M A-scan inputs but is homogeneous with spectrum $N_{in}(f)$. Thus the scattering noise covariance matrix is diagonal

$$\begin{aligned}\mathbf{Q}(f_l) &= \mathbf{N}_{in}(f_l)\mathbf{N}_{in}^+(f_l) \\ &= N_{in}^2(f_l)\mathbf{I}\end{aligned}\tag{Eq. 5.36}$$

where \mathbf{I} is a $M \times M$ dimensional unit matrix. The input noise power spectral density will be

$$\begin{aligned}|\mathbf{N}_{in}(f_l)|^2 &= \mathbf{N}_{in}^+(f_l)\mathbf{N}_{in}(f_l) \\ &= \text{Tr } \mathbf{Q}(f_l) \\ &= N_{in}^2(f_l)\text{Tr } \mathbf{I} \\ &= MN_{in}^2(f_l)\end{aligned}\tag{Eq. 5.37}$$

From Eq. 5.35 and Eq. 5.37 we can obtain the input signal-to-noise ratio $SNR_{in}(f)$ as

$$\begin{aligned}SNR_{in}(f_l) &= \frac{MS_{in}^2(f_l)}{MN_{in}^2(f_l)} \\ &= \frac{S_{in}^2(f_l)}{N_{in}^2(f_l)}\end{aligned}\tag{Eq. 5.38}$$

According to the distortionless constraint represented by Eq. 5.19, the output signal power spectral density (PSD) should be identical to that of the input signal PSD, i.e.

$$|\mathbf{S}_{out}(f_1)|^2 = MS_{in}^2(f_1) \quad \text{Eq. 5.39}$$

Meanwhile the output noise PSD can be found from Eq. 5.18, Eq. 5.28 and Eq. 5.36 as

$$\begin{aligned} |\mathbf{N}_{out}(f_1)|^2 &= \mathbf{H}_i^+(f_1)\mathbf{N}(f_1)\mathbf{N}^+(f_1)\mathbf{H}_i(f_1) \\ &= \mathbf{H}_i^+(f_1)\mathbf{Q}(f_1)\mathbf{H}_i(f_1) \\ &= \frac{\mathbf{u}^+(f_1)\mathbf{Q}^{-1}(f_1)}{\mathbf{u}^+(f_1)\mathbf{Q}^{-1}(f_1)\mathbf{u}(f_1)}\mathbf{Q}(f_1)\frac{\mathbf{Q}^{-1}(f_1)\mathbf{u}(f_1)}{\mathbf{u}^+(f_1)\mathbf{Q}^{-1}(f_1)\mathbf{u}(f_1)} \\ &= \frac{1}{\mathbf{u}^+(f_1)\mathbf{Q}^{-1}(f_1)\mathbf{u}(f_1)} \\ &= \frac{1}{\mathbf{u}^+(f_1)[N_{in}^2(f_1)\mathbf{I}]^{-1}\mathbf{u}(f_1)} \\ &= \frac{N_{in}^2(f_1)}{M} \end{aligned} \quad \text{Eq. 5.40}$$

Therefore the output signal-to-noise ratio $SNR_{out}(f_1)$ is

$$\begin{aligned} SNR_{out}(f_1) &= \frac{|\mathbf{S}_{out}(f_1)|^2}{|\mathbf{N}_{out}(f_1)|^2} \\ &= \frac{MS_{in}^2(f_1)}{\frac{1}{M}N_{in}^2(f_1)} \\ &= M^2 \frac{S_{in}^2(f_1)}{N_{in}^2(f_1)} \end{aligned} \quad \text{Eq. 5.41}$$

and the matrix filter system SNR gain is

$$\begin{aligned} G(f_1) &= \frac{SNR_{out}(f_1)}{SNR_{in}(f_1)} \\ &= M^2 \end{aligned}$$

Eq. 5.42

where the M is the number of the matrix filter input channels. This result is M times better than that of a conventional averaging filter, under the same assumptions as above.

It should be noted that in practice the matrix filter gain will not always increase with the number of input channels. This is because the above analysis is obtained under the following ideal assumptions:

- (i) All M input channels are receiving the same wanted (plane wave) signal.
- (ii) The noise in the M channels is uncorrelated.

Obviously, as the number of input A-scans (channels) M increases, it would be more likely that assumption (i) above will no longer be valid. Alternatively, if we increase the number of the input channels within the transducer beam width to guarantee that all channels receive the same wanted signal, then the noise in the M channels will become increasingly correlated and so assumption (ii) is in jeopardy. Furthermore, even if M has been properly selected, the scattering noise in different channels may still be partially correlated. And finally, there is no guarantee that the defect signal in the adjacent channels will be unchanged. All these facts can degrade the performance of the matrix filter.

5.1.4 Minimum-variance distortionless response filtering

In practice, we usually can not obtain the noise covariance matrix $\mathbf{Q}(f_i)$ alone, since target signals may be present. However, we can always measure the total signal covariance matrix $\mathbf{P}(f_i)$ directly. If we replace the noise covariance matrix $\mathbf{Q}(f_i)$ with the total signal covariance matrix $\mathbf{P}(f_i)$ in Eq. 5.18 and follow the same procedures described in section 5.1.2, we can obtain a column vector of the transfer function for the minimum variance distortionless response (MVDR):

$$\mathbf{H}_t(f_i) = \frac{\mathbf{P}^{-1}(f_i)\mathbf{u}(f_i)}{\mathbf{u}^+(f_i)\mathbf{P}^{-1}(f_i)\mathbf{u}(f_i)}$$

Eq. 5.43

The philosophy behind this rule is that we can anticipate on the whole, that the main contribution to the total signal power is from the noise in a highly scattering environment. Thus if the total output signal power can be minimised under the constraint that the wanted signal is not distorted, the output signal-to-noise ratio will be enhanced. However, it might be anticipated that the achievable SNR enhancement of the present method could be less than that can be obtained by the MNDR method, since the MVDR method uses less *a priori* information concerning the noise environment.

5.1.5 Minimum-noise distortionless matrix filter: Implementation

As mentioned before, in order to simplify the computations, the processing cell length should be properly selected so that the signal over the time duration of the cell can be assumed as stationary with uncorrelated Fourier coefficients for different frequencies. Therefore, the corresponding covariance matrix defined by Eq. 5.11 and Eq. 5.12 is blocking diagonal. To meet this requirement, a novel implementation is specially designed for the current application environment. In this, the input A-scan traces were divided into a number of processing cells or windows with equal time duration close to the pulse length. The processing window is then slid over the time and space range of the A-scans. The adjacent processing windows can be with or without overlapping.

As is well known, for a stationary process, its ensemble expectation can be approximated by the best unbiased estimate over a finite number of observations of the signals. That is for stationary noise, the covariance matrix $\mathbf{Q}(f_l)$ can be estimated by

$$\begin{aligned}\mathbf{Q}(f_l) &= E[\mathbf{N}_k(f_l)\mathbf{N}_k^+(f_l)] \\ &= \frac{1}{k+1} \sum_{j=0}^k \mathbf{N}_j(f_l)\mathbf{N}_j^+(f_l).\end{aligned}$$

Eq. 5.44

Under a nonstationary situation, Eq. 5.44 would not be a good estimate of $\mathbf{Q}(f)$, since as a result of its infinite memory nature, changes in the statistical characteristics of the data cannot be tracked.

In a nonstationary situation, the ideal noise covariance $\mathbf{Q}(f)$ can be approached by the sequential regression (SER) algorithm [Ahmed, N.]. In this, $\mathbf{Q}(f)$ is estimated from past k observations of the signal with “fading” memory α

$$\begin{aligned}\mathbf{Q}_k(f_l) &= \sum_{j=0}^k \alpha^{k-j} \mathbf{N}_j(f_l) \mathbf{N}_j^+(f_l) \\ &= \alpha \sum_{j=0}^{k-1} \alpha^{k-1-j} \mathbf{N}_j(f_l) \mathbf{N}_j^+(f_l) + \mathbf{N}_k(f_l) \mathbf{N}_k^+(f_l) \\ &= \alpha \mathbf{Q}_{k-1}(f_l) + \mathbf{N}_k(f_l) \mathbf{N}_k^+(f_l)\end{aligned}$$

$$0 < \alpha < 1$$

Eq. 5.45

where α is the scaling factor. It should approach 1 if $\mathbf{N}_j(f)$ is stationary. The summation of this scaling factor over k iterations is

$$\sum_{j=0}^k \alpha^{k-j} = \frac{1 - \alpha^{k+1}}{1 - \alpha}$$

Eq. 5.46

If we define the sequential regression estimation of the noise covariance matrix $\mathbf{Q}(f)$ by normalising Eq. 5.45 with this value, then we have

$$\begin{aligned} \mathbf{Q}(f_l) &= \frac{1-\alpha}{1-\alpha^{k+1}} \mathbf{Q}_k(f_l) \\ &= \frac{1-\alpha}{1-\alpha^{k+1}} \sum_{j=0}^k \alpha^{k-j} \mathbf{N}_j(f_l) \mathbf{N}_j^+(f_l). \end{aligned}$$

Eq. 5.47

It is seen that in the limiting case, where $\mathbf{N}_j(f_l)$ is stationary for all j , α approaches 1 and we get exactly the same expression for the stationary noise covariance matrix $\mathbf{Q}(f_l)$ given by Eq. 5.44.

The new implementation of the MVDR time-space array processing with sequential regression estimation of the noise covariance matrix developed for the current application can now be summarised as:

- (i) Select the input channel number M of the matrix filter to cover an area about same as the beam width of the transducer and the processing window length N about same as the signal pulse duration.
- (ii) Use the $M \times N$ input samples to form the time-space sampling vector \mathbf{x} defined by Eq. 5.1 and transfer it to the frequency domain \mathbf{X} according to the definition of Eq. 5.2-Eq. 5.4.
- (iii) Initially assume the first cell contains noise only, i.e. use $\mathbf{N}_0(f_l) = \mathbf{X}_0(f_l)$ to estimate the noise covariance matrix $\mathbf{Q}_0(f_l)$. In processing the $(k+1)$ th window, assume the k th window contains noise only, i.e. $\mathbf{N}_k(f_l) = \mathbf{X}_k(f_l)$, and use it with $\mathbf{Q}_{k-1}(f_l)$ to estimate the noise covariance matrix $\mathbf{Q}(f_l)$ according to Eq. 5.45 and Eq. 5.47.
- (iv) Slide the processing window (or processing cell) throughout the A-scan traces with or without overlapping and estimate the signal

frequency spectrum and time waveform using Eq. 5.29 and Eq. 5.30 respectively.

- (v) Shifting the matrix filter across every A-scan trace to obtain the optimal waveform estimation for all the scanned region to produce a B-scan image.

It should be noted in the above processing procedures it has been assumed that there is no target signal present in the previous nearby cells but in practice this might not always be the case. However as has been pointed out in Section 5.1.4, suppose the target signals are present in the past nearby cells, under such circumstances the MNDR filter will be degraded to the MVDR filter but the signal-to-noise ratio can still be enhanced by the MVDR filter. On the other hand, it can also be anticipated that potential interference of target signals in the past cells can be reduced by using sequential regression estimation of the noise covariance matrix due to its “fading” memory feature.

5.2 Adaptive Wiener filter

From a consideration of the non-stationary nature of the grain scattering it can be anticipated that two dimensional adaptive optimal filtering approaches should be advantageous in exploiting differential features between a local region in an image and its neighbouring regions. One such optimal filter considered here is an adaptive Wiener filter [Lee, J.S.]. The configuration of the Wiener filter is schematically presented in Figure 5.2. Its implementation and performance will be discussed in detail below.

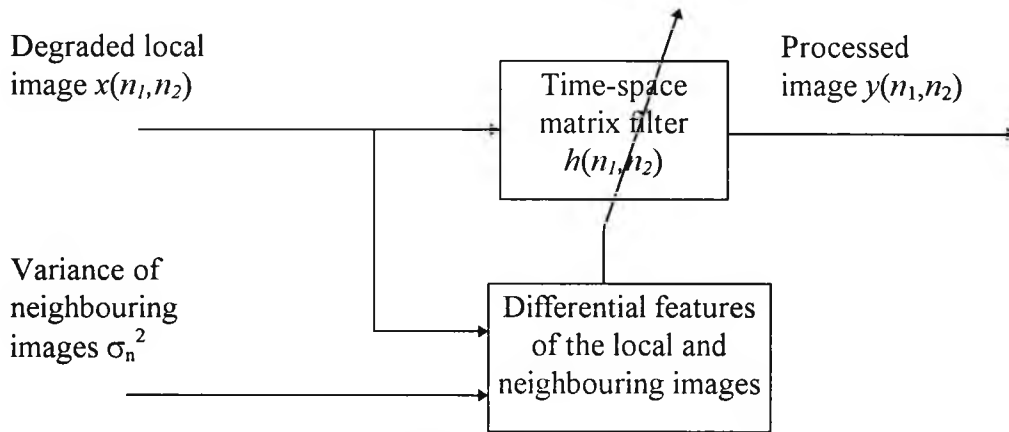


Figure 5.2 Adaptive Wiener filtering system.

5.2.1 Adaptive Wiener filtering for image enhancement

Suppose the degraded input image $x(n_1, n_2)$ can be expressed as an undistorted image $s(n_1, n_2)$ plus additive noise $n(n_1, n_2)$ with zero mean and variance σ_n^2 . That is

$$x(n_1, n_2) = s(n_1, n_2) + n(n_1, n_2). \quad \text{Eq. 5.48}$$

Here n_1 , n_2 denote the A-scan trace number and time series sample number, respectively. The objective of the Wiener filter is to minimise the mean square errors (MMSE) between the undistorted image $s(n_1, n_2)$ and the estimated image at the matrix filter output $y(n_1, n_2)$, i.e.,

$$y(n_1, n_2) = h(n_1, n_2) \oplus x(n_1, n_2), \quad \text{Eq. 5.49}$$

where the symbol \oplus denotes the two-dimensional convolution. In the frequency domain, this will become

$$Y(\omega_1, \omega_2) = H(\omega_1, \omega_2)X(\omega_1, \omega_2), \quad \text{Eq. 5.50}$$

where $h(n_1, n_2)$ and $H(\omega_1, \omega_2)$ are the filter impulse response and its frequency response function, respectively. The optimal filter impulse response or frequency response function can be determined by minimising the mean square errors of the filter output:

$$\begin{aligned} e^2(h) &= E\{|s(n_1, n_2) - y(n_1, n_2)|^2\} \\ &= E\{|s(n_1, n_2) - h(n_1, n_2) \oplus x(n_1, n_2)|^2\} \end{aligned} \quad \text{Eq. 5.51}$$

or equivalently minimising the mean square error of the corresponding spectrum

$$\begin{aligned} e^2(H) &= E\left\{[S(\omega_1, \omega_2) - H(\omega_1, \omega_2)X(\omega_1, \omega_2)]^2\right\} \\ &= E[S^2(\omega_1, \omega_2)] - 2E[S(\omega_1, \omega_2)X(\omega_1, \omega_2)]H(\omega_1, \omega_2) \\ &\quad + E[X^2(\omega_1, \omega_2)]H^2(\omega_1, \omega_2) \\ &= P_{SS} - 2P_{SX}H(\omega_1, \omega_2) + P_{XX}H^2(\omega_1, \omega_2) \end{aligned} \quad \text{Eq. 5.52}$$

where P_{uv} denotes the cross power spectrum of random variables u and v

$$P_{uv} = E[U(\omega_1, \omega_2)V(\omega_1, \omega_2)] \quad \text{Eq. 5.53}$$

The minimum mean square error can be achieved by taking the variation of Eq. 5.52 with respect to the filter frequency response function $H(\omega_1, \omega_2)$ and setting the result to zero, i.e.

$$\begin{aligned}
\delta e^2(H) &= -2P_{sx}\delta H(\omega_1, \omega_2) + 2P_{xx}H(\omega_1, \omega_2)\delta H(\omega_1, \omega_2) \\
&= 2\delta H(\omega_1, \omega_2)[P_{xx}H(\omega_1, \omega_2) - P_{sx}] \\
&= 0
\end{aligned}$$

Eq. 5.54

Thus we have

$$\begin{aligned}
H(\omega_1, \omega_2) &= \frac{P_{sx}}{P_{xx}} \\
&= \frac{P_{ss} + P_{sn}}{P_{ss} + 2P_{sn} + P_{nn}}
\end{aligned}$$

Eq. 5.55

If the original image and the additive noise are uncorrelated and the mean of the image is subtracted from the power spectrum, then the filter frequency response function becomes

$$H(\omega_1, \omega_2) = \frac{\sigma_s^2}{\sigma_s^2 + \sigma_n^2}$$

Eq. 5.56

where σ_s^2 and σ_n^2 are the variances of the original image and noise, respectively.

The corresponding time-space domain impulse response function is

$$h(n_1, n_2) = \frac{\sigma_s^2}{\sigma_s^2 + \sigma_n^2} \delta(n_1, n_2).$$

Eq. 5.57

Although the Wiener filter is in closed form, the variances of the original target image and the noise usually can not be measured directly. However it is possible to estimate the variances adaptively from differential features between the

local and neighbouring images as represented in Figure 5.2. In the implementation for the current work, the processing window is divided into nine regions as illustrated in Figure 5.3. Each of the regions contains M A-scans of N points. For example, a typical complete data set contains 64 A-scans of 1000 points, whereas M and N for each processing region are typically 6 and 64 (i.e. 2^6), respectively. The processing window is then slid in turn along the time and space axes to cover all the A-scan regions.

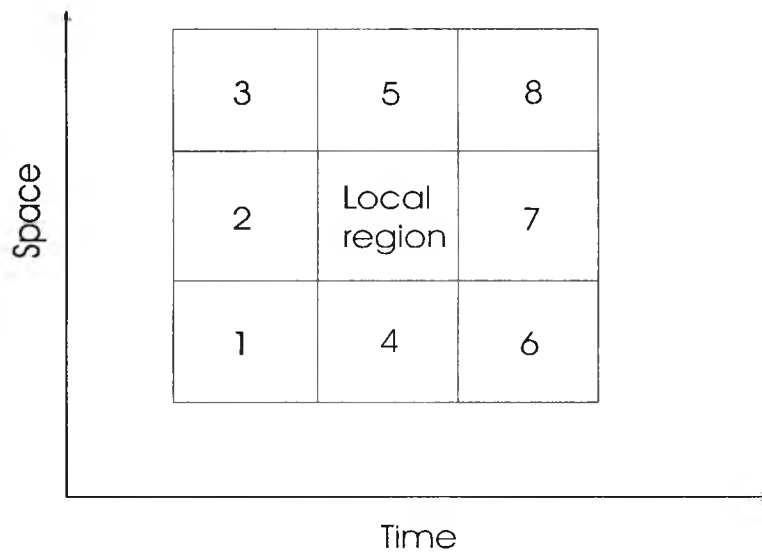


Figure 5.3 A processing window for adaptive Wiener filter.

In detecting small defects, it can be anticipated that the main contribution to the variance of the image in a relatively large area would be from the grain noise. Thus the noise variance σ_n^2 can be estimated from a larger neighbouring area such as the eight neighbouring regions of the local region illustrated in Figure 5.3, i.e.

$$\sigma_n^2 = \frac{1}{8MN} \sum_{i=1}^8 \sum_{n_1=1}^M \sum_{n_2=1}^N [x_i(n_1, n_2) - m_n(i)]^2$$

Eq. 5.58

in which $m_n(i)$ is the mean of the i th neighbouring region, i.e.

$$m_n(i) = \frac{1}{MN} \sum_{n_1=1}^M \sum_{n_2=1}^N x_i(n_1, n_2)$$

$$i = 1, 2, \dots, 8$$

Eq. 5.59

The variance of the target image is estimated from the local region

$$\sigma_s^2 = \begin{cases} \sigma_x^2 - \sigma_n^2 & \text{if } \sigma_x^2 > \sigma_n^2 \\ 0 & \text{otherwise} \end{cases}$$

Eq. 5.60

where σ_x^2 is the variance of the local image, i.e.

$$\sigma_x^2 = \frac{1}{MN} \sum_{n_1=1}^M \sum_{n_2=1}^N [x(n_1, n_2) - m_x]^2$$

Eq. 5.61

and m_x is the mean of the local image, i.e.

$$m_x = \frac{1}{MN} \sum_{n_1=1}^M \sum_{n_2=1}^N x(n_1, n_2).$$

Eq. 5.62

Finally the processed image $y(n_1, n_2)$ within the local region can be expressed as

$$\begin{aligned}
y(n_1, n_2) &= m_x + \frac{\sigma_s^2}{\sigma_s^2 + \sigma_n^2} \delta(n_1, n_2) \oplus [x(n_1, n_2) - m_x] \\
&= m_x + \frac{\sigma_s^2}{\sigma_s^2 + \sigma_n^2} [x(n_1, n_2) - m_x].
\end{aligned}$$

Eq. 5.63

In order to reduce processing time, the means and variances used in Eq. 5.63 are updated at each processing window, rather than point-by-point.

5.2.2 Performance of Adaptive Wiener filter

It can be seen from Figure 5.2 and Eq. 5.63, that the adaptive Wiener filtering algorithm is based on a two-channel process. In this, the input image is divided into a local image region and its neighbouring image regions. The statistical characteristics of the images in the local and neighbouring regions are given by their means and variances. The visibility of a local image can be described by its intensity and contrast, which are quantitatively determined by the local mean m_x and $x(n_1, n_2) - m_x$. To enhance the visibility of a local image, the adaptive Wiener filter modifies the local contrast according to the differential features of the local image and its neighbouring images.

It would be easier to gain some insight of the performance of the adaptive Wiener filter, if we consider two extreme cases. That is, if in a local region where the variance of the local image is much greater than the noise covariance estimated

from its neighbouring regions, i.e. $\sigma_s^2 \gg \sigma_n^2$, the local contrast is assumed mainly to be contributed by the signal $s(n_1, n_2)$. In this case, the Wiener filter gain will approach one, and the filter output will remain approximately the same as the original input $x(n_1, n_2)$. Whilst if the variance of the local image is much smaller than the noise covariance: $\sigma_s^2 \ll \sigma_n^2$, the local contrast is assumed to be mainly due to the noise $n(n_1, n_2)$. In this case the gain of the Wiener filter will approach zero and the output of the filter will be close to the local mean m_x . As a result, the local contrast will be significantly reduced. Thus the overall effects of the Wiener filter are to enhance the signal components and suppress the noise components.

5.2.3 Attenuation compensation

From the above analysis it can be noted that even if the signal component is determined to be dominant in a local region, its contrast will remain approximately unchanged. The visibility of a signal after filtering will still be dependent on its original contrast compared to other regions. Thus in a non-stationary noisy environment, such as in the presence of grain scattering and attenuation, some noise in the region near the transducer may still be visible after filtering, especially if its original local contrast is very high, such as for those massive grain clusters. On the other hand, signals from true targets lying at greater depth may be lost if their local contrasts are too low due to scattering and attenuation. Hence, it should be possible to further enhance filter performance by compensating for attenuation effects.

As we mentioned in Chapter 2, the attenuation effects can be modelled by an exponential function. That is, if the original unattenuated signal is denoted by $x(t)$, then the attenuated signal $z(t)$ can be expressed as

$$z(t) = e^{-\alpha \frac{t}{T}} x(t).$$

Eq. 5.64

where T is the total waveform duration and α as a first order approximation is taken to be an attenuation coefficient averaged over the bandwidth of the signals of interest. In fact, as illustrated in Section 6.4.3, the bandwidth of a defect echo is considerably narrow than that of grain scattering. Therefore this correction is actually a reasonable approximation for the wanted defect signals. Based on this consideration the original signal $x(t)$, can be approximately recovered from $z(t)$ by

$$x(t) = e^{\alpha \frac{t}{T}} z(t).$$

Eq. 5.65

The attenuation coefficient α can then be expressed as

$$\alpha = \ln \left| \frac{x(T)}{z(T)} \right|$$

Eq. 5.66

where $x(T)$ and $z(T)$ are the backwall echoes before and after the attenuation respectively.

According to plane wave theory, the magnitude of the unattenuated backwall echo $x(T)$ can be evaluated from the frontwall echo $z(0)$ by taking into account the reflection and transmission losses. Consider a plane wave impinging at normal incidence on a smooth plane boundary (relative to the wavelength), the reflection coefficient R and transmission coefficient D between medium 1 and 2 can be calculated from their acoustic impedances $Z_i = \rho_i c_i$ ($i = 1, 2$), in which ρ_i and c_i are the corresponding medium density and sound speed, respectively. From this

theory, it is easy to show that the unattenuated backwall echo $x(T)$ can be evaluated from the frontwall echo $z(0)$ by

$$x(T) = -\frac{4Z_1Z_2}{(Z_1 + Z_2)^2} z(0)$$

Eq. 5.67

where Z_1 and Z_2 are the acoustic impedances of the coupling medium (for both plane boundary surfaces) and the test material.

The attenuation coefficient α can then be evaluated from the amplitude of the frontwall and (attenuated) backwall echoes by

$$\alpha = \ln \left| \frac{-4Z_1Z_2z(0)}{(Z_1 + Z_2)^2 z(T)} \right|$$

Eq. 5.68

Of course, this formula can only be applicable under the assumption that both the frontwall and backwall echoes are not saturated.

The processing results from both optimal time-space array processing and adaptive Wiener filtering are presented as false colour B-scan images in the next chapter. Comparisons are made with results from the spatial averaging method.

6. Results

In this chapter, the various signal and image processing techniques developed for the current application will be evaluated using real experimental data captured from the material of current interest. The description of the experimental system set-up together with the testing material and targets will be presented in Section 6.1. In order to evaluate signal processing techniques in a quantitative way, automatic detectors will be used to test the performances of signal enhancement. It is convenient therefore to discuss and evaluate these detectors in Section 6.2 prior to testing the one-dimensional signal enhancement techniques in Sections 6.3 and 6.4. The two-dimensional array processing and image enhancement techniques will be evaluated finally in Section 6.5.

Also, it is helpful to define signal-to-noise ratio in a fashion that takes account of the pulsed nature of the wanted signal. To this end, the defect signal-to-grain-noise ratio is defined here as

$$SNR = 10 \log_{10} \left(\frac{\frac{1}{N_s} \sum_{i=M-N_s/2}^{M-1+N_s/2} y^2(i)}{\frac{1}{N_t} \sum_{i=0}^{N_t-1} y^2(i) - \frac{1}{N_s} \sum_{i=M-N_s/2}^{M-1+N_s/2} y^2(i)} \right)$$

Eq. 6.1

where M is the sample index corresponding to the centre of the target signal and N_s and N_t are the length of the signal from the target and the total data length, respectively.

6.1 Experimental systems

6.1.1 Data acquisition

Two systems have been used to capture A-scan data. The first made use of a wide-band system developed at City University by Dr. J.P. Weight. The second was a state-of-the-art data acquisition system installed at the NDT Department at Rolls-Royce, Filton. The basis of both systems is similar and is as shown schematically in Fig 6.1.1.

The experimental set-up used in the ultrasonics laboratory at City includes a wide-band system to generate and receive ultrasonic pulses (within an overall bandwidth 0.5 - 20 MHz) and a digital oscilloscope for data capture. The A-scan signals were obtained using an unfocused 5MHz, 20mm diameter transducer (Aerotech Alpha F08179). The signals were digitised by a LeCroy 4910 digital oscilloscope at a sampling rate of 100MHz with 16 bit resolution and then transferred to a PC via an IEEE488 interface using software developed by the author. Signal processing was carried out on both a SUN SPARC Station 2, and on a 486DX2 66MHz PC.

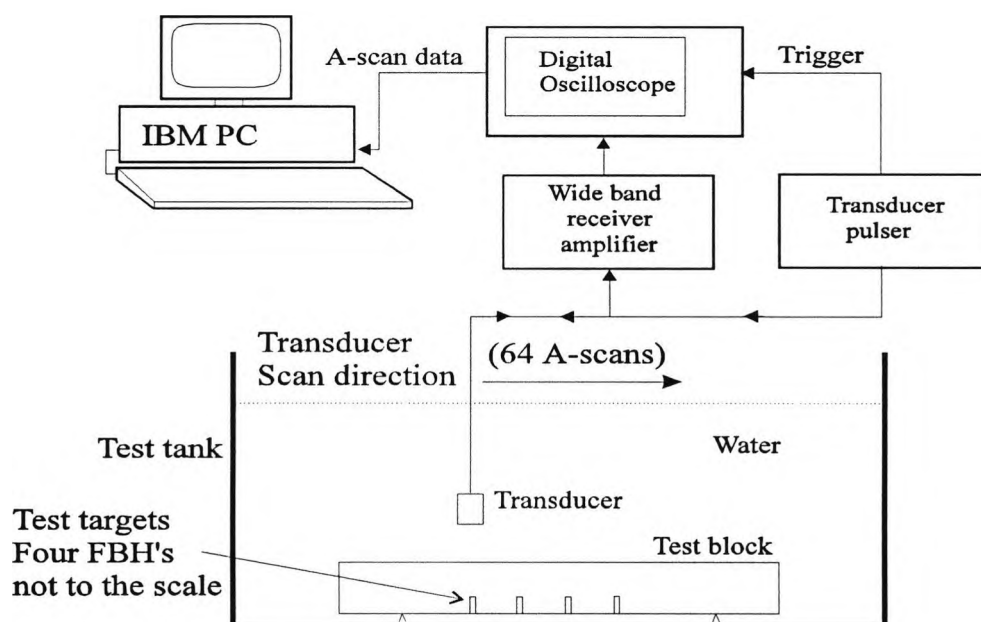


Figure 6.1.1 Schematic diagram showing the basis of the ultrasonic data acquisition systems used.

The data acquisition system used at Rolls-Royce can automatically capture sequential A-scan data with 8 bit resolution at a sampling rate of 100MHz and scan repetition rate of 1000 A-scan/sec. It has the capability of performing spatial averaging as the scan proceeds. When averaged data is required, the mean is normally taken over 6 adjacent A-scans. A typical data set usually contains 64 A-scans including test targets consisting of four flat-bottomed holes (FBH) which were drilled at the backwall of the test block (as illustrated in Figure 6.1.1). A more detailed description of the test targets and materials will be given in the next section. Two transducers were used: an unfocused, 5MHz, 12.7mm diameter probe and a weakly focused 10MHz, 12.7mm diameter transducer (RR type No. D12149, focal length 152mm).

In all cases, a water-coupled transducer was used and the test pieces were fabricated from various samples of Waspaloy. To avoid the greatly complicated structure of echo responses resulting from near-field diffraction effects [Weight, J.P., 1993], the water coupling path was chosen so that the samples were within the far field of the interrogating transducers.

6.1.2 Testing material and targets

In the present work, the material of interest in the evaluation of the various signal and image processing techniques presented here is Waspaloy. Waspaloy is a Nickel based superalloy designed to maintain high strength, with good creep, crack and fatigue resistance, in demanding high-temperature environments [Shen, G.]. One of the most common applications of the materials is for the disk like structures anchoring the turbine blades in a jet engine. To ensure the required mechanical properties, the disks are usually forged and then heat-treated. Consequent machining and work hardening often leads to relatively coarse-grained, inhomogenous microstructures. Since jet engine disks are safety-critical components, the ability to detect small defects with reliability guaranteed by a large

safety margin is, of course, of paramount importance. However, as a result of the coarse-grained, inhomogenous structure of the Waspaloy, the detection of small flaws is often limited by the masking effect of scattering from grain boundaries.

In order to gain some insight of the grain structure of Waspaloy, microscopic examination of a sample from a typical test piece has been carried out by the author. The metallographic specimen was prepared by grinding, polishing and etching operations. The sample block was first lapped manually using silicon carbide paper abrasives of 800 grit, followed by 1200 grit, using water as a lubricant. All the scratches from grinding were then removed by polishing on nylon cloth wheels charged with 6-micron and then 1-micron diamond paste, lubricated with a few drops of lapping oil to obtain a mirror-like polished surface. The grain boundaries of the Waspaloy were finally revealed by chemical etching with a solution of ferric chloride.

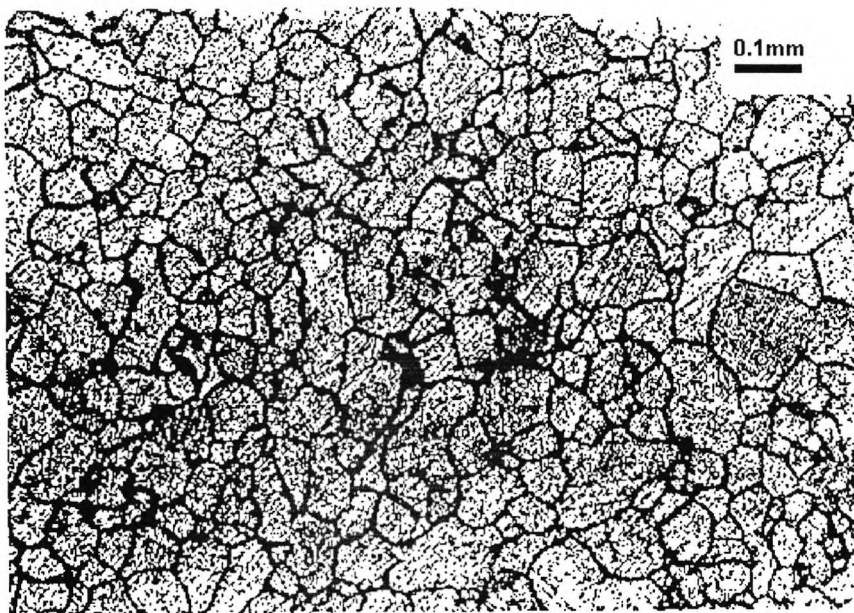


Figure 6.1.2 Photomicrograph of a Waspaloy specimen taken at a location to illustrate the typical mean grain size. This is estimated to be about 0.1mm.

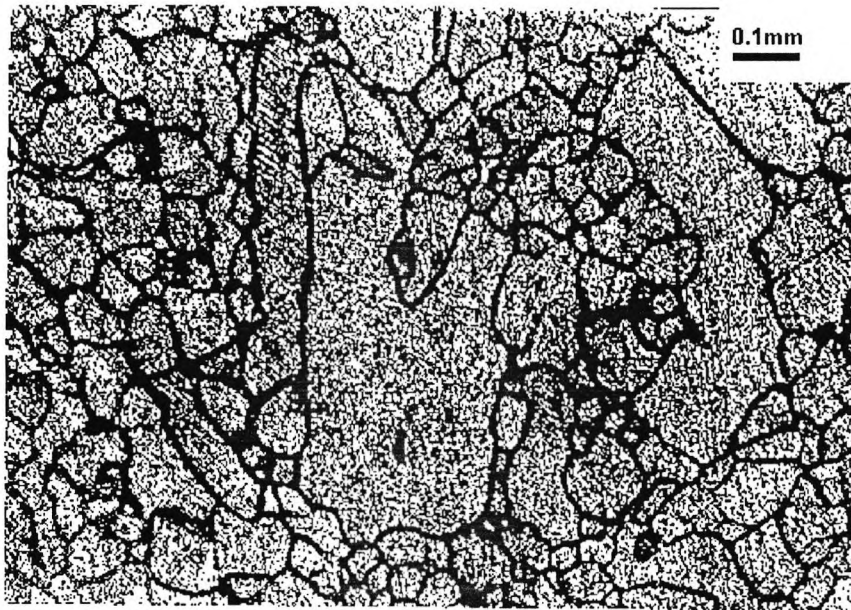


Figure 6.1.3 Photomicrograph of a Waspaloy specimen taken at an area containing a massive grain at its centre. The size of the large grain is well over 0.5mm and as such is similar to the desired minimum (albeit more strongly scattering) detectable defect.

The microstructure features of the prepared Waspaloy specimen were examined under a microscope at 100 times magnification. Photomicrographs were taken at two representative locations to demonstrate the mean grain structure as well as the existence of “massive grain clusters”. Figure 6.1.2 shows that the mean size of the grains is about 0.1mm, whereas the size of the massive grain shown in the centre of Figure 6.1.3 is well over 0.5mm. The mean grain size is such that the material will in general be highly scattering at the ultrasonic frequencies used, even though these were chosen bearing in mind the conflicting requirements of resolution and sensitivity. The existence of massive grain clusters at not infrequent positions gives rise to extra, localised scattering. Eventhough the effective scattering cross section of a grain cluster will be less than that of a test target of similar dimension, the grain clusters could be falsely classified as defect signals, especially when they lie at short range. It is likely that these “rogue” grains could be the major source of excessive false alarms when conventional processing such as fixed threshold detection is used.

The majority of the data to be considered here was obtained from known artificial defects. In reality, the shape of a natural flaw is usually very irregular and can not be simulated by any universal model. However, it is sensible to use some simple targets for preliminary evaluation of various processing algorithms. This could also offer potentially simplified mathematical modelling. One such commonly used target is a flat-bottom hole (FBH) with its axis aligned with the incident beam. Typically, the target size (area of the bottom surface) was chosen so that the defect signal had similar amplitude to the unwanted grain scattering.

The experimental data was taken from three main types of test samples. The first was two coarse-grained samples of Waspaloy (a 50mm cube and a 50×50×25mm block) containing a test target - a 1mm diameter FBH. The second was a section of jet engine disc (JED) containing 0.64mm and 0.89mm FBH's. The third was also taken from a jet engine disc but from a region not including any test targets. However this last group did include two A-scans containing a real flaw identified by the NDT group at Rolls-Royce.

The data provided by Rolls-Royce was taken from a test piece cut from a Waspaloy jet engine disc (JED). The JED test piece contained test targets consisting of four groups of flat-bottomed holes. Due to some special treatments required to make the jet engine disc, its grain size varies along the radius (increases towards outer edge) of the disc. Two sets of six holes of diameter 0.64mm and 0.89mm were drilled in a "noisy" section (larger grain size area) of the JED test piece and two identical sets were positioned in a section having a finer grain structure (less "noisy"), making 24 test targets in all. Some data was provided from each of these sets but only the data from the noisy section was processed, since the signal to noise ratio of the data from cleaner section was good enough for all of the targets to be detected by conventional means. Usually the data comprised 64 A-scans obtained whilst scanning a transducer in a single line passing over typically four test targets.

Most of the data captured included echo signals from the front and back walls of the test piece. In general, the wanted signal and the grain noise were at a level much smaller than the front and back wall echoes. If the receiver gain was set to give good signal to (random electronic) noise ratio, the front and back wall echoes would be well above the saturation point of the receiver. Since the saturated wall echoes are not useful for any signal processing but can in fact introduce some distorted frequency components into the signal spectrum to spoil signal processing, the wall echoes are excluded before further processing.

6.2 Results: Detection

Here the performance of adaptive threshold detection is compared with simple fixed threshold detection, where the threshold level is set empirically. The current application is restricted to the use of non-coherent detection since a synchronised reference signal is not available. Therefore only the envelope information is needed for detection purposes. This is extracted using a square-law envelope detector that gives a similar output to that from the rectified and smoothed signal output from a typical receiver. The data was integrated over a time duration similar to that of the transmitted pulse length.

Typical inputs and outputs to the envelope detector are illustrated in Figure 6.2.1(a) and (b), respectively. A similar rectified and smoothed signal is also included (Figure 6.2.1(c)) for comparison. In this example, the input data contains 600 samples which corresponds to $6\mu\text{s}$ of original data. The smoothing effect of integrating the data means that a longer sampling interval is adequate. Typically the number of data points can be reduced by a factor of 20. This will considerably enhance the efficiency of detection processing.

Much of the literature in this area gives relatively few results to demonstrate the usefulness of particular methods but here an attempt was made to give statistically reliable results by using data set containing 64 A-scans. An example of results for just one A-scan (taken from the JED test piece using a 5MHz, 13mm diameter unfocused transducer) and known to include a true target signal is given in Figure 6.2.2. The input A-scan is shown on the top left (a), and the corresponding output from the square-law envelope detector (b) is shown alongside. The outputs from the fixed thresholding, CA-CFAR and ACML-CFAR detectors are shown below as (c), (d) and (e), respectively. In this particular example, all three detectors have correctly identified the true target signal from a 0.89mm flat bottomed hole. There are however two false indications from the fixed thresholding detector, but none from the adaptive detectors. Figure 6.2.3 shows some corresponding results but for the case when there is no known target signal in the input data. Now the fixed threshold detector gives two false target indications but both adaptive detectors are free of false alarms.

To allow a direct comparison of the various methods used in Figure 6.2.2-3, the detection parameters for each detector were chosen to give a similar detection rate over a set of 64 A-scans. The results are summarised in Table 6.2.1 and show that the two adaptive detectors have similar performance for the case of a single target in a homogeneous noise environment. As discussed in Section 3.2.2, the only advantage of the ACML-CFAR detector is that it should give better performance with multiple target situations.

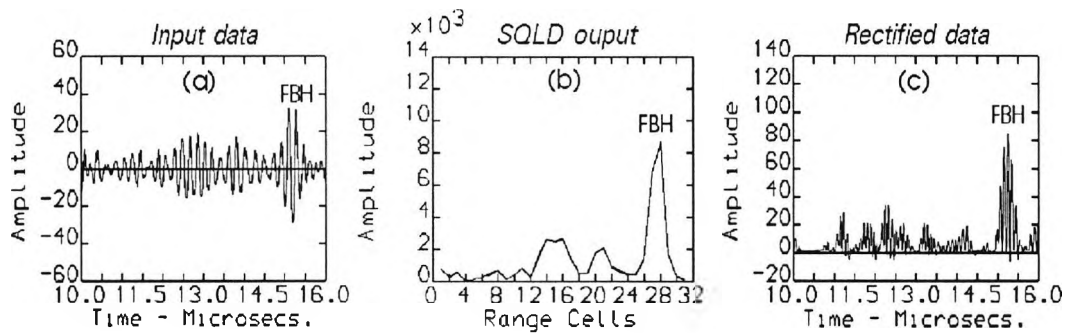


Figure 6.2.1 Unrectified input data is shown in (a). Figures (b) and (c) are the output of the square-law envelope detector and the rectified data respectively.

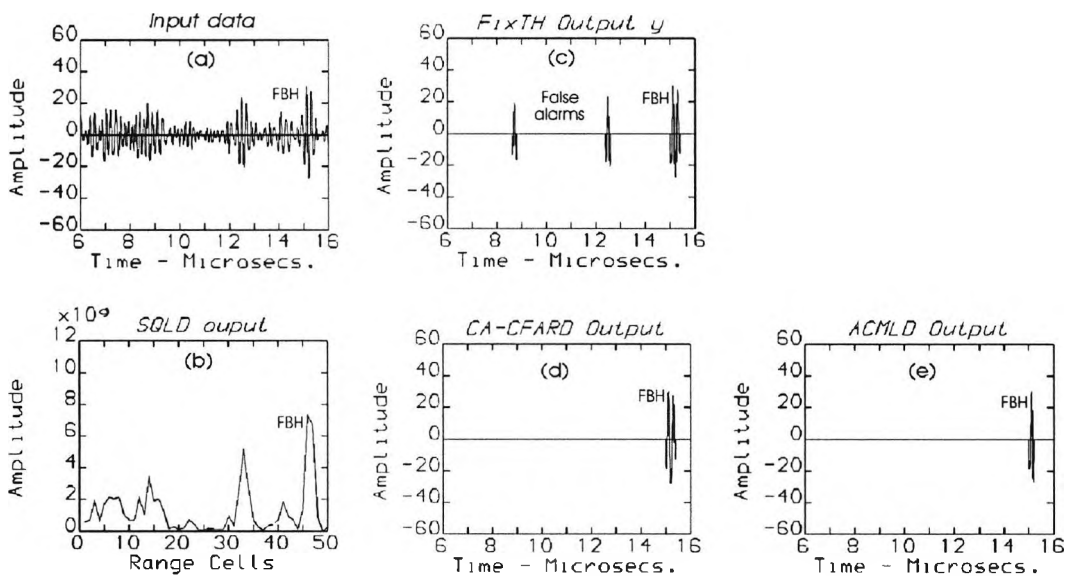


Figure 6.2.2 The input A-scan waveform and corresponding square-law envelope detector output are shown in (a) and (b). The outputs of the fixed thresholding, CA-CFAR and ACML-CFAR detectors are given as (c), (d) and (e), respectively.

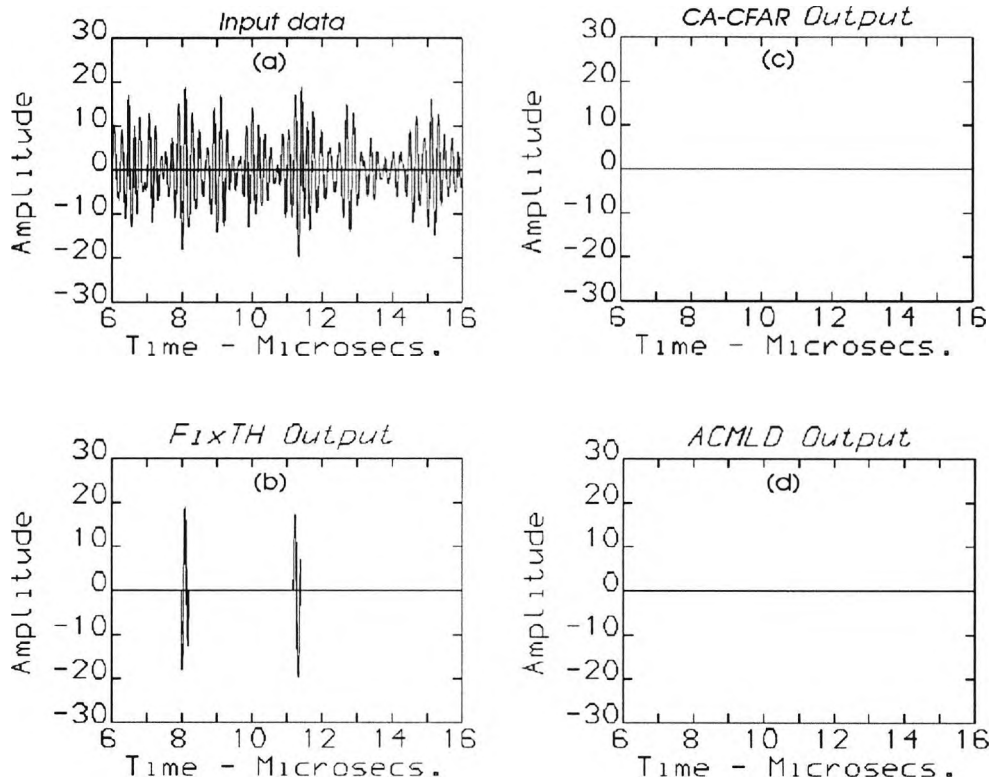


Figure 6.2.3 The input data did not include any known target signal but the fixed threshold detector gave two false target indications. However, both adaptive detectors were free of false alarms.

A group of 64 A-scans data taken by a 5MHz, 12.7mm diameter unfocused transducer from a Wasपालoy Jet engine disc.	Fixed Thresholding Detection Processing Parameters: $T_h = 3100$ $T_c = 0.2 \mu s$		CA-CFAR Detector Processing Parameters: $P_f = 4 \times 10^{-3}$ $T_c = 0.2 \mu s$		ACML-CFAR Detection Processing Parameters: $P_f = 4 \times 10^{-3}$ $T_c = 0.2 \mu s$	
	No spatial averaging	Spatial averaged	No spatial averaging	Spatial averaged	No spatial averaging	Spatial averaged
Known Targets: 0.86mm FBH						
Target 1 indications	2	4	0	4	0	4
Target 2 indications	3	0	0	2	0	2
Target 3 indications	4	3	2	2	2	2
Target 4 indications	3	1	0	0	0	0
Unknown target indications	170	14	4	4	5	3
Unknown target positions	66	7	4	2	5	3

Table 6.2.1 Summary of the detection results from a set of 64 A-scans

Before going on to discuss the tabulated results for the set of 64 A-scans, it is helpful to discuss what would be expected if the test block was constructed from a completely noise-free material and the transducer were to be scanned directly over the centre line of the targets. For the target size, scan increment and beam width employed, it can be expected that about 10 adjacent scans may include a signal from a given test target. However with the much poorer signal-to-noise ratios obtained from the Waspaloy test piece used here, the number of adjacent scans showing a positive target indication is likely to be less than this. This partly arises as a consequence of the poorer signal-to-noise ratio itself, but also because of the Gaussian-like beam profile. Furthermore, the number of positive indications would be further reduced if the line of scan was not directly through the centre of each target. On discussing this point with the Rolls-Royce personnel who captured the data, it transpired that each target fell within the beam, but it was not guaranteed that the scan line was through *every* target centre.

In the rows showing true target indications in Table 6.2.1 we see that the maximum number of true indications for a given target is in fact just 4 and that not all targets are always detected. The first method - fixed thresholding without spatial averaging - gives the most positive target indications but suffers from a large number of false alarms.

It is convenient to classify the false alarms as follows: the total number of false indications is given as “unknown target *indications*”, but if an unknown target indication continually appears in adjacent A-scans at the same time position we denote it as from a single target position (i.e. “unknown target *positions*”).

The number of false alarms using fixed thresholding can be reduced considerably by using original data that had been spatially averaged, but unfortunately the number of true indications also drops somewhat. Both of the adaptive detectors give even fewer false alarms - especially when used with spatial averaging - whilst maintaining a similar number of true target indications.

Tests showed that the performance of the CA-CFAR and ACML-CFAR detector was not particularly sensitive to the values chosen for the desired false alarm rate and the number of reference cells, given by $N_c = T/T_c$. Here T and T_c are the total waveform time duration and cell duration, respectively. For instance, with the current data, good results were obtained if $0.001 \leq P_f \leq 0.0001$. The better the signal-to-noise ratio r , the smaller could be the value of P_f to achieve a similar detection rate.

The advantage of using a fixed thresholding level detector is of course its simplicity, ease of implementation and freedom from the need to make assumptions on the probability distribution of the grain noise. However, the theoretical analysis and experimental results have shown that with a fixed threshold detector, the false alarm rate is extremely sensitive to fluctuations in the noise power. Consequently, its detection performance is very sensitive to the setting of the threshold level, therefore its consistency can not be controlled in the current application environment, where noise power often changes with inspection position. In contrast, detection performances of the adaptive threshold detectors are self optimised and consistent performance is maintained as noise levels fluctuate. This is demonstrated by the results of Table 6.2.1, where the data noise levels do fluctuate as a result of a varying grain structure.

6.3 Results: Split-spectrum processing

To evaluate the various split spectrum processing methods described in Section 4.1, a set of 64 A-scans provided by Rolls-Royce was processed. Again, the data were taken from a test piece cut from a Waspaloy jet engine disc using the same experimental conditions as for Table 6.2.1. A number of results from individual A-scans are presented first, before summarising results from the whole set in Table 6.3.1. Where known targets are present in the individual results, their positions are labelled FBH.

6.3.1 Processing parameter selection

Split spectrum processing parameters can be determined by following the procedures described in Section 4.1 but with some modifications to suit current experimental conditions. For instance, instead of using the backwall echo to determine the upper frequency cut-off point as described by [Karpur, P. 1988] the echo from a known target was used. This was more appropriate for the current work, since the defects are of wavelength order and their echo responses are likely to have different frequency content compared to that of the echo from a large plane reflector such as the backwall. The following procedure was adopted:

- (1) The central frequency separation between adjacent filter is set to $\Delta f = 1/T$, where T is the duration of a single A-scan.
- (2) Set the half power bandwidth of the filter to $B_f = 3\Delta f$ and fix the central frequency of the first Gaussian bandpass filter at 1MHz above the lowest frequency of the received signal spectrum.

- (3) The number of filters N is then increased until the SNR for a known target signal reaches a maximum. The optimum processing frequency bandwidth is then determined by $B = (N - 1)\Delta f$.
- (4) The half power bandwidth of the filter can then be optimised by adjusting the B_f to obtain the maximum SNR.

6.3.2 Processing results

Using the above procedure for the data shown in Figure 6.3.1, $\Delta f = 0.0833\text{MHz}$ and the optimum SSP parameters are $B_f = 0.3\text{MHz}$ and the frequency range is $3\text{MHz} \leq f \leq 6.5\text{MHz}$. The number of filters required to cover this frequency range is $N = 43$. Corresponding SSM, SSPT and SSPTM results are shown in Figure 6.3.1 (c), (e), and (f) respectively. Figure 6.3.1(d) gives the output from the ACML detector when fed with data after SSM processing, using the same detector parameters as used in Table 6.2.1, i.e. a false alarm rate P_f of 10^{-4} and a cell time duration T_c of $0.2\mu\text{s}$. The adaptive detector described in Chapter 3 will be used here, as it is later useful as a means to objectively measure the variation in signal enhancement when changing the values of parameters used in SSM processing. Since the polarity thresholding method used with split spectrum processing is itself a form of detector, the results from polarity threshold processing in (e) and (f) can be directly compared with the adaptive detector output (d). It is clear that all of the SSP algorithms enhance the defect SNR remarkably, but the output after polarity thresholding shows a number of false alarms. Furthermore as will be illustrated by Figure 6.3.4, if constant parameters are used for all 64 A-scans in a set, there will be some instances where the wanted signal is lost rather than enhanced.

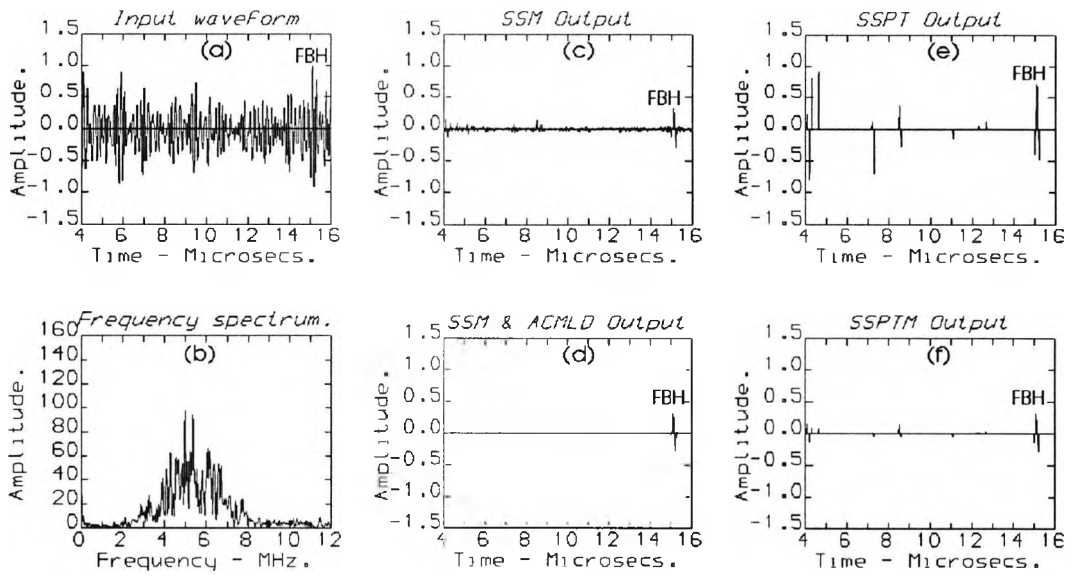


Figure 6.3.1 Split spectrum processing results using the present adaptation of Karpur's method to set parameters. A typical example of the original data is shown in the time and frequency domains in (a) and (b), respectively. The position of the true target signal is denoted by FBH. Results after processing are shown in (c - f): (c) after minimisation; (d) after minimisation and adaptive detection; (e) after polarity thresholding and (f) after polarity thresholding and minimisation.

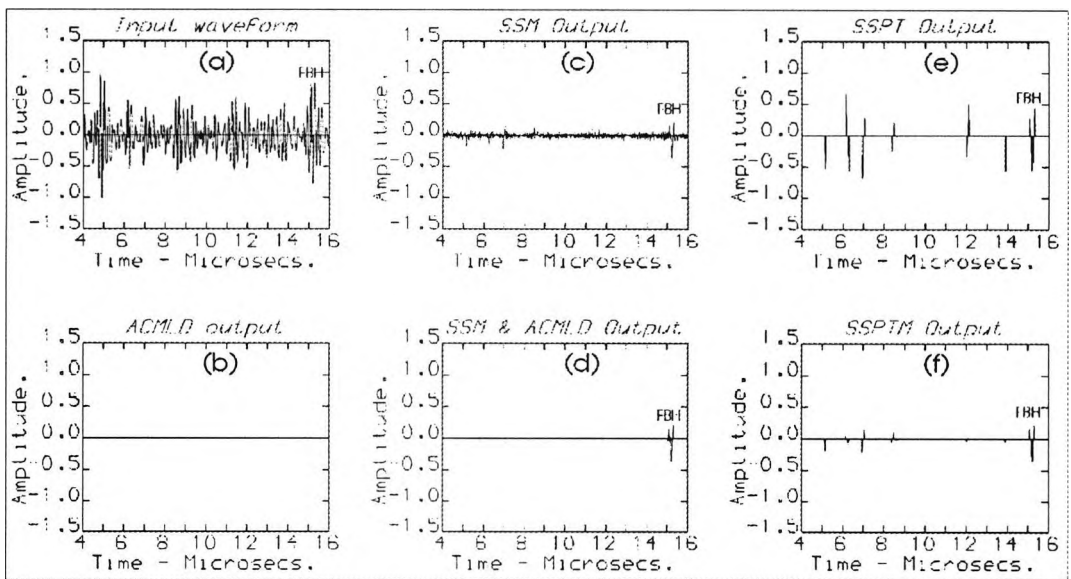


Figure 6.3.2 Split spectrum results as in Figure 6.3.1, but showing the original data after adaptive detection in (b).

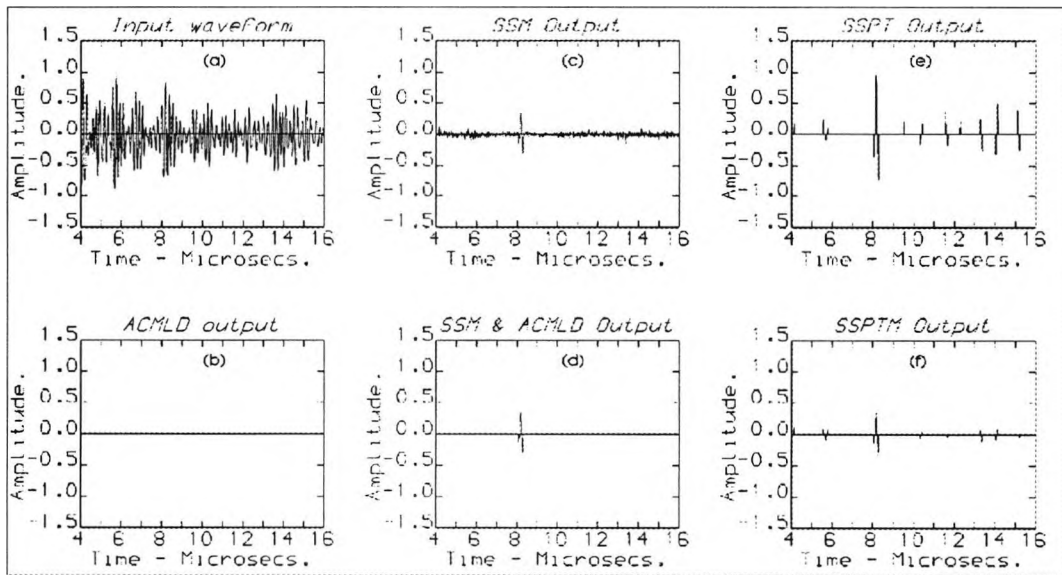


Figure 6.3.3 Split spectrum results as in Figure 6.3.2, but at a position where no known target exists.

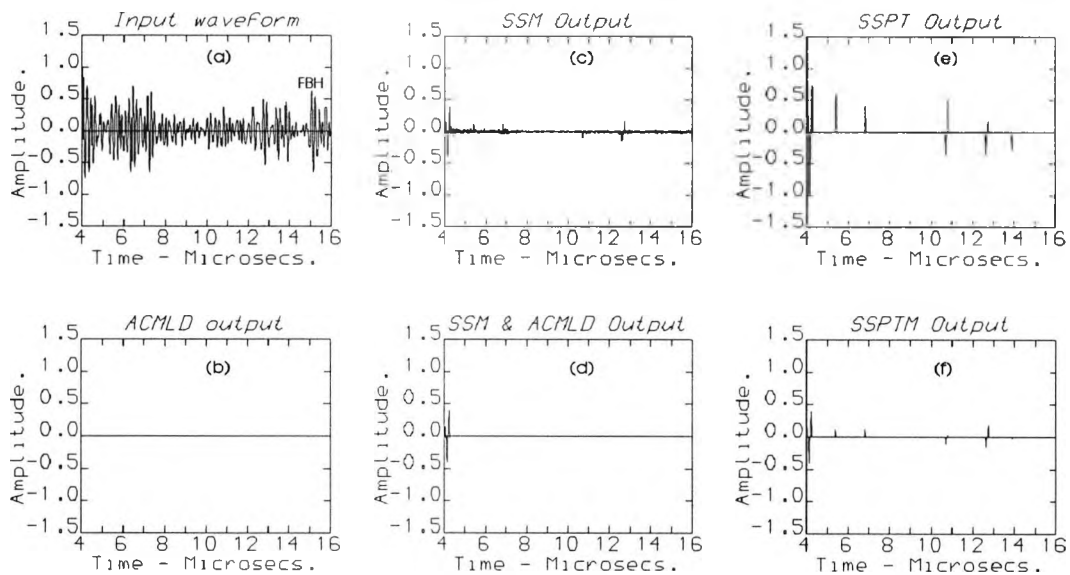


Figure 6.3.4 Split spectrum results as in Figure 6.3.2, but with a poorer input signal to noise ratio. None of the methods used were able to detect the true signal.

Figure 6.3.2-Figure 6.3.4 illustrate SSP results using the same parameters as for Figure 6.3.1 but for a number of A-scans at different transducer position including one where there was no known target (Figure 6.3.3). The SSM, SSPT and SSPTM methods give similar results for the data of Figure 6.3.1 and Figure 6.3.2 - the true target signal is always detected but there are a number of false alarms using a polarity thresholding detector or polarity thresholding after minimisation. However, in Figure 6.3.3(a) there is no known target but all SSP methods give false alarms. On the other hand, if the input SNR in a given A-scan is lower than that used to determine the processing parameters, then a known target signal may not be found as in Figure 6.3.4.

The results shown so far have been made with a fixed central frequency separation $\Delta f = 1/T$ defined in Section 4.1. This requires the number of filters N to be 43 to cover the processing frequency range of 3.5MHz as selected above. Tests carried on a large number of A-scans from the same test piece give similar problems to those identified in Figure 6.3.1- Figure 6.3.4 and it would seem that the method suggested by Karpur et al to select SSP parameters is not optimum for the current data.

An alternative implementation of SSP - using a fixed overlap point at the half power point of the Gaussian bandpass filter proposed here has also been investigated. Figure 6.3.5- Figure 6.3.7 illustrate some results processed using this approach, particularly in order to optimise the SSM processing. The optimal parameters used here were: frequency range $3\text{MHz} \leq f \leq 6\text{MHz}$, number of the filters $N = 3$. In Figure 6.3.5 - Figure 6.3.6, the grain scattering is visibly reduced compared to the known wanted signal (FBH), but the output SNR has not been enhanced sufficiently for the known signal to be found by the ACML detector. Here the same detector parameters as before, i.e. a false alarm rate $P_f = 10^{-4}$ and cell duration $T_c = 0.2\mu\text{s}$ are used. A higher false alarm rate could detect the known signal but only at the expense of increasing the total number of false alarms.

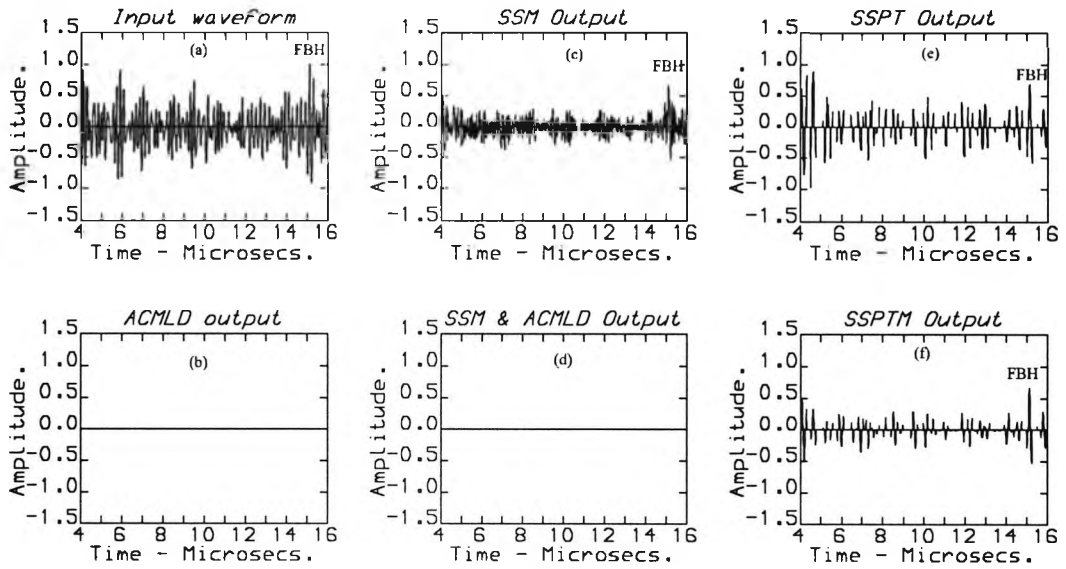


Figure 6.3.5 Split spectrum processing results as in Figure 6.3.2, but using a fixed overlap point at the half power point of the Gaussian bandpass filter and with the parameters selected empirically to give optimum overall performance for SSM processing. Note that the data used in Figure 6.3.5 to Figure 6.3.7 was identical to that of Figure 6.3.1 - Figure 6.3.2 and Figure 6.3.4, respectively.

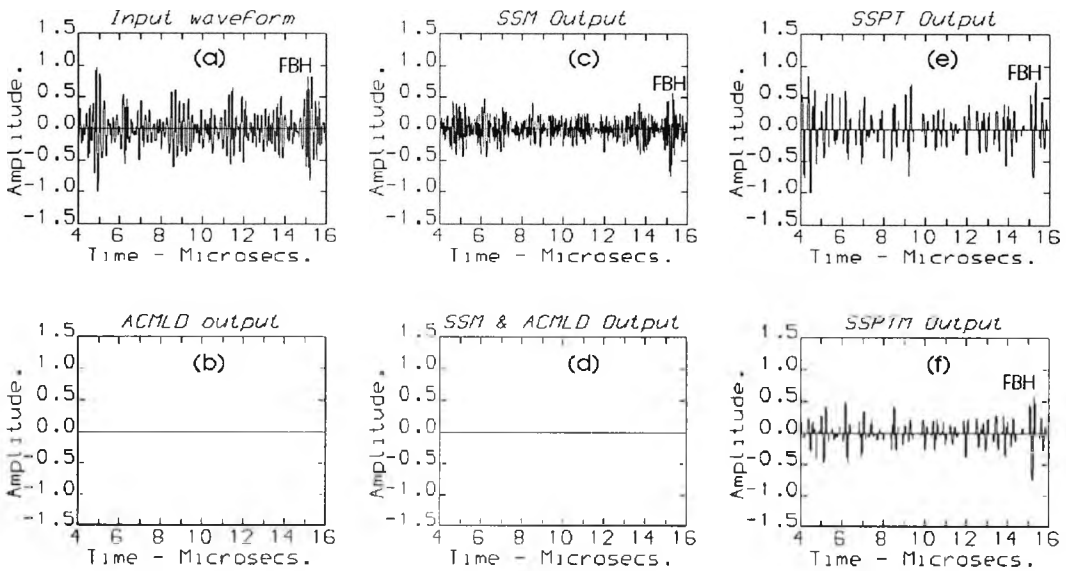


Figure 6.3.6 Split spectrum results as in Figure 6.3.2 but using the same method as in Figure 6.3.5.

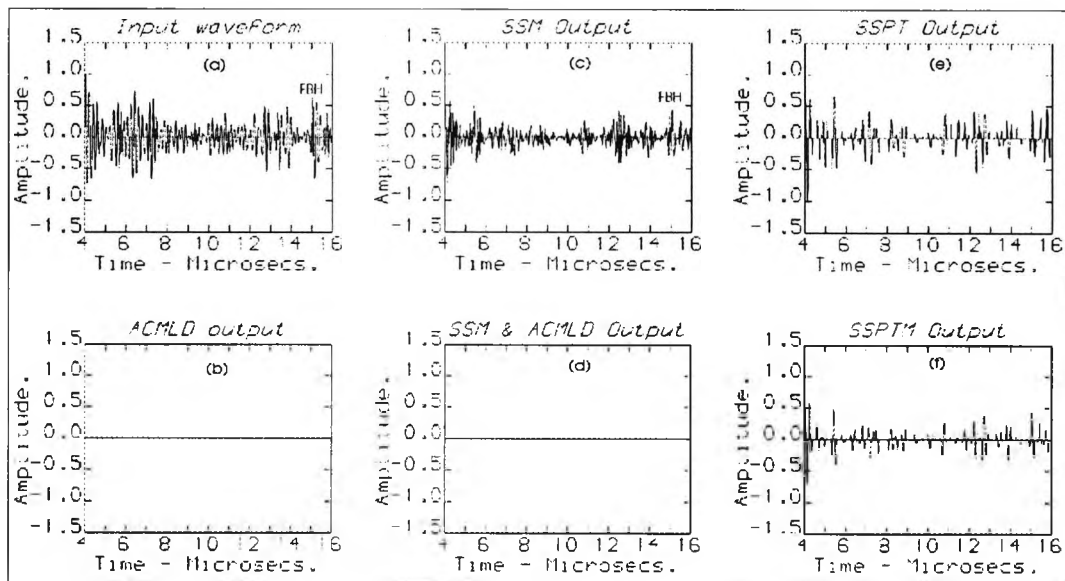


Figure 6.3.7 Split spectrum results using the same method as in Figure 6.3.5, but with a poorer input signal to noise ratio. None of the methods was able to reliably detect the true signal.

The approach used to obtain the results of Figure 6.3.5-Figure 6.3.7 gives less sensitivity to parameter selection and can use up to a factor of ten less filters than does the method of Karpur et al for the current application. Once chosen the parameters may be kept constant for a given test piece. However, in spite of this the signal to noise ratio in these scans is so poor that it was not possible to reliably detect all known signals.

One method investigated here to improve the detection of wanted signals is to use the iterative approach outlined in Section 4.1. In the results shown in Figure 6.3.8 - Figure 6.3.10 two iterations were used. The data used for Figure 6.3.8 - Figure 6.3.10 were the same as that of Figure 6.3.5 - Figure 6.3.7, respectively. In Figure 6.3.8 and Figure 6.3.9, the SNR's are significantly enhanced after SSM, better than was achieved in Figure 6.3.5 and Figure 6.3.6, and now in

(d) it is possible to detect the known signal, using SSM followed by adaptive detection, without any false alarms. However, this could not be consistently achieved, especially with SNR's poorer than that of the data used to set the parameters, as shown in Figure 6.3.10.

The sensitivity of SSP to the number of filters used is demonstrated in Figure 6.3.11 - Figure 6.3.13. By changing from 3 to 15 filters whilst retaining all other parameters, a dramatic SNR enhancement can be achieved with SSPT, however, unfortunately there is still a large number of false alarms. Furthermore, as also demonstrated in Figure 6.3.11- Figure 6.3.13, a similar test with the SSM method found that with 15 filters there was no improvement at all over the unprocessed SNR's and hence even with adaptive detection, the known signal cannot be detected.

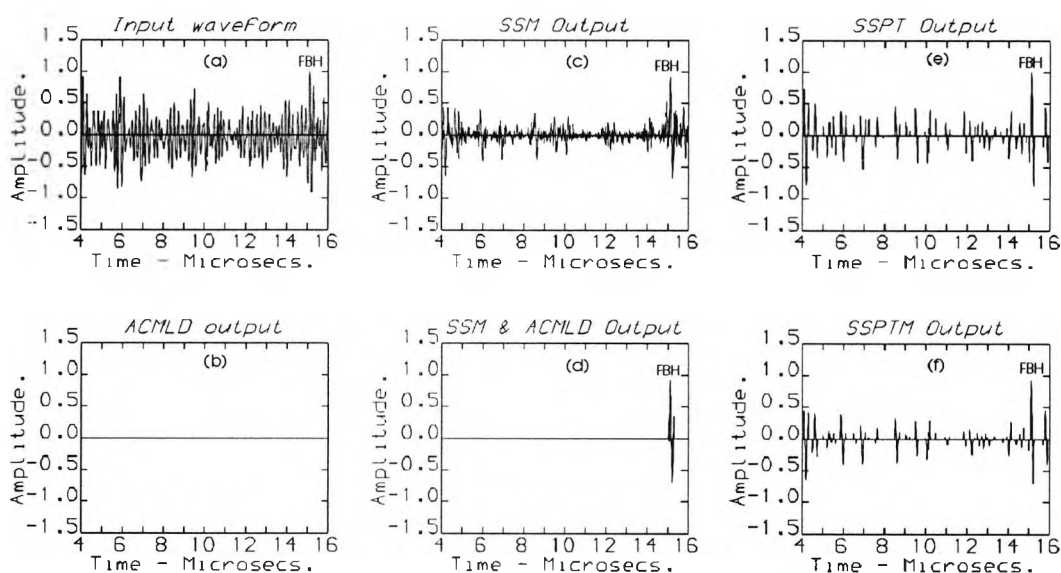


Figure 6.3.8 Split spectrum processing results using the method adapted here to select optimum minimisation parameters as in Figure 6.3.5 - Figure 6.3.7, but with two iterations as described in Section 4.1. The data was as for Figure 6.3.1 and Figure 6.3.5 but here the extra processing gives much better signal enhancement.

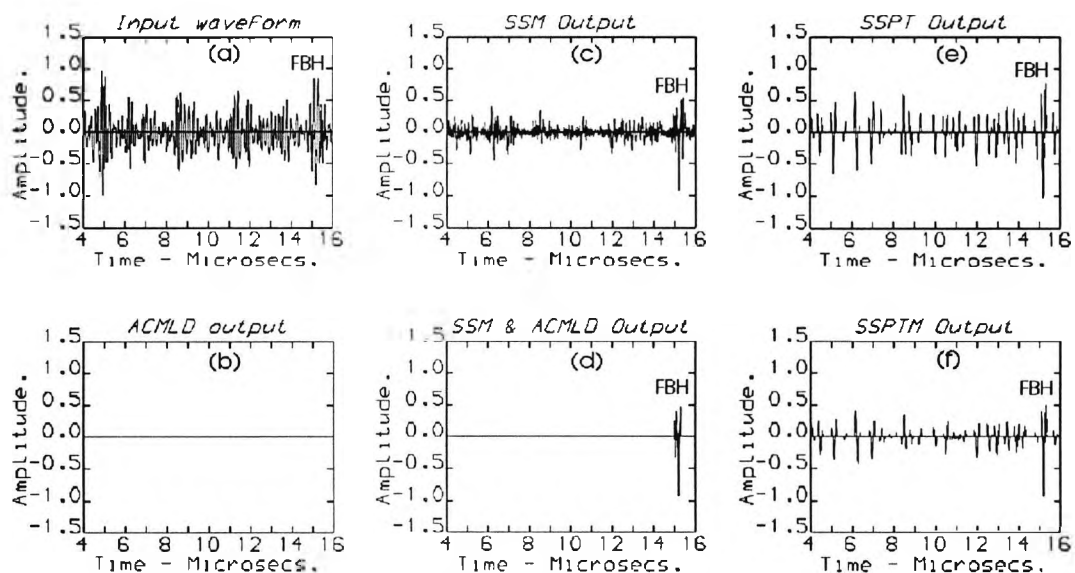


Figure 6.3.9 Split spectrum processing results using the method adapted here as in Figure 6.3.8. The data was as for Figure 6.3.2 and Figure 6.3.6, but note the much better signal enhancement.

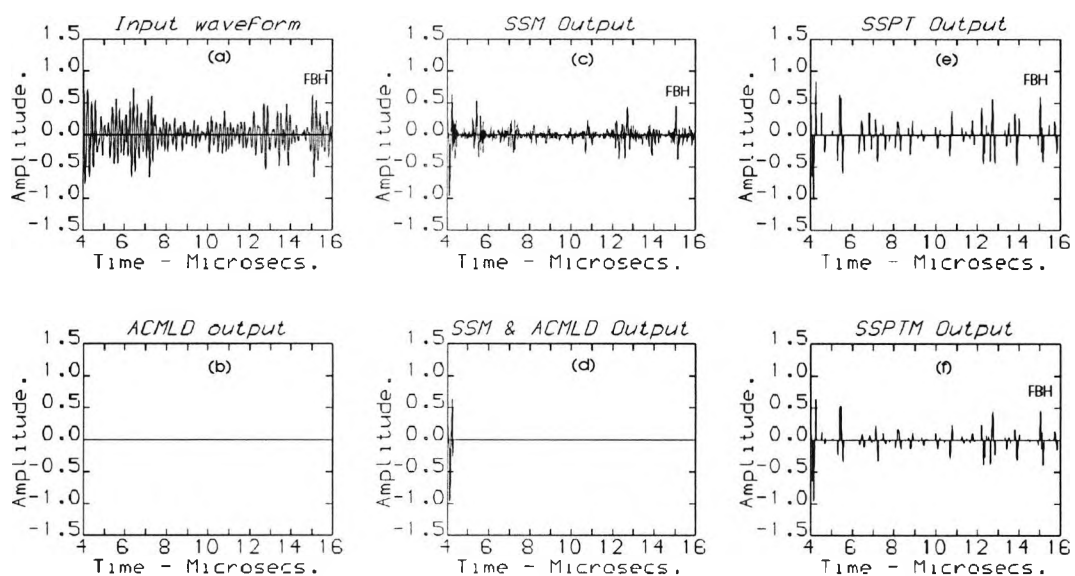


Figure 6.3.10 Split spectrum processing results using the modified method as in Figure 6.3.9 but for the data of Figure 6.3.4 and Figure 6.3.7 that had a poorer input signal to noise ratio. None of the methods were able to reliably detect the true signal.

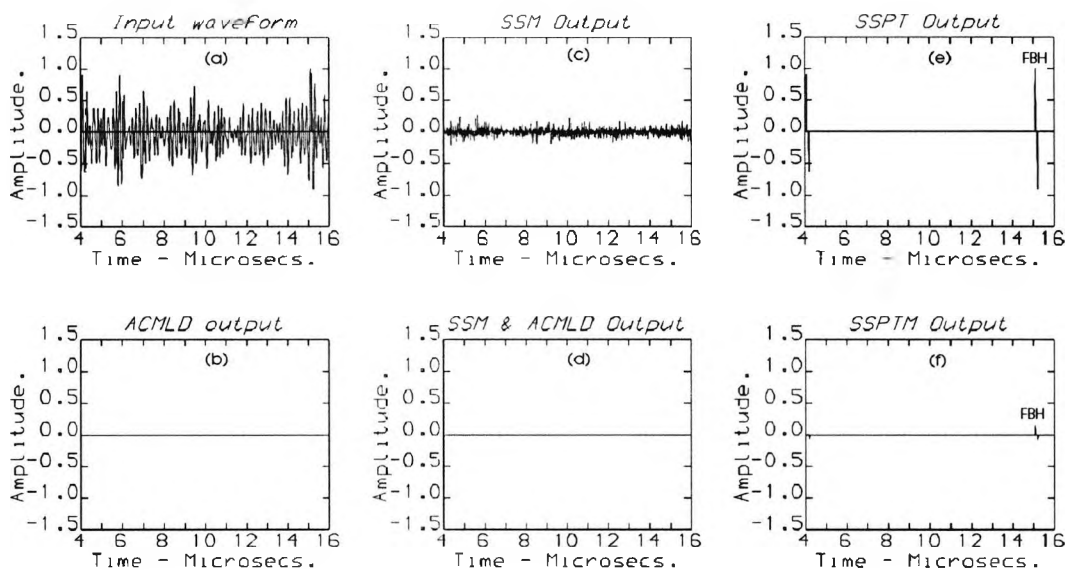


Figure 6.3.11 Split spectrum processing results using the modified method to select optimum parameters for polarity thresholding. The data was as for Figure 6.3.5 and Figure 6.3.8 but note almost complete lack of false alarms in the polarity thresholding results (e and f).

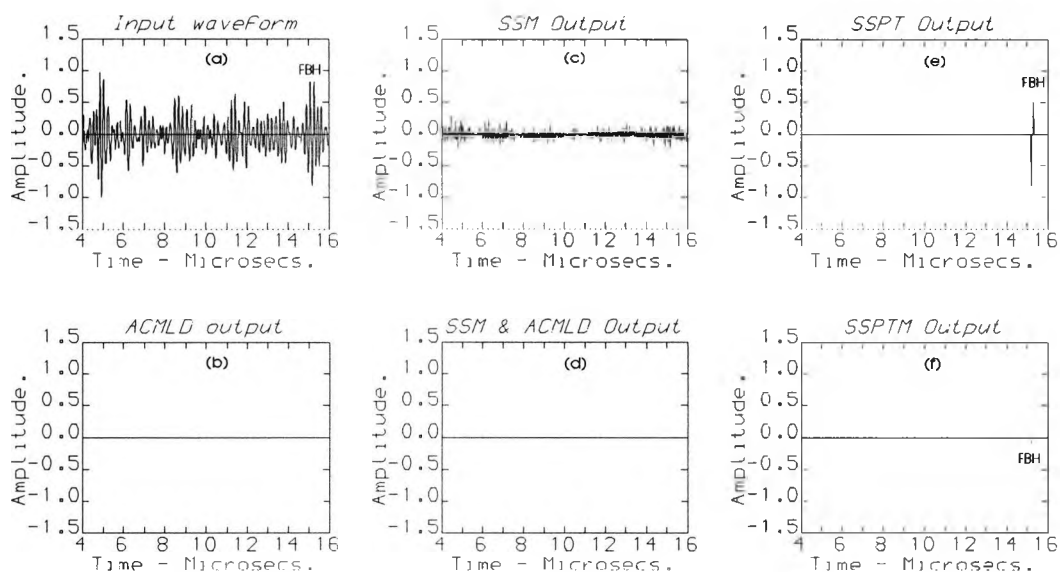


Figure 6.3.12 Split spectrum processing results using the modified method to select optimum parameters as used in Figure 6.3.11. The data was as for Figure 6.3.6 and Figure 6.3.9. Again note completely free of false alarms after polarity thresholding (e and f).

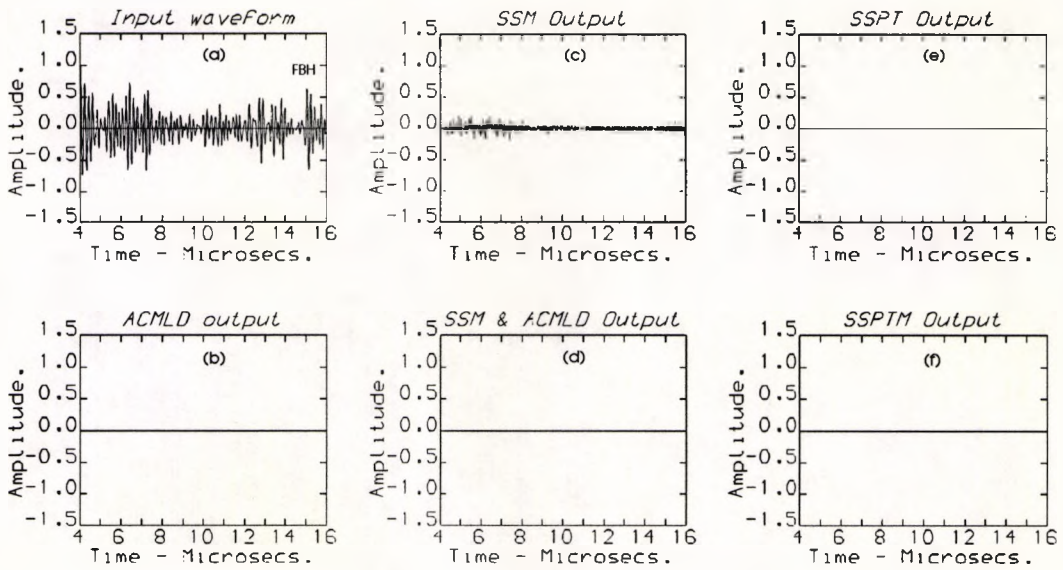


Figure 6.3.13 The data was as for Figure 6.3.7 and Figure 6.3.10 and using the modified method to select optimum parameters as used in Figure 6.3.11. Again with such poor signal to noise ratio none of the methods could detect the true signal.

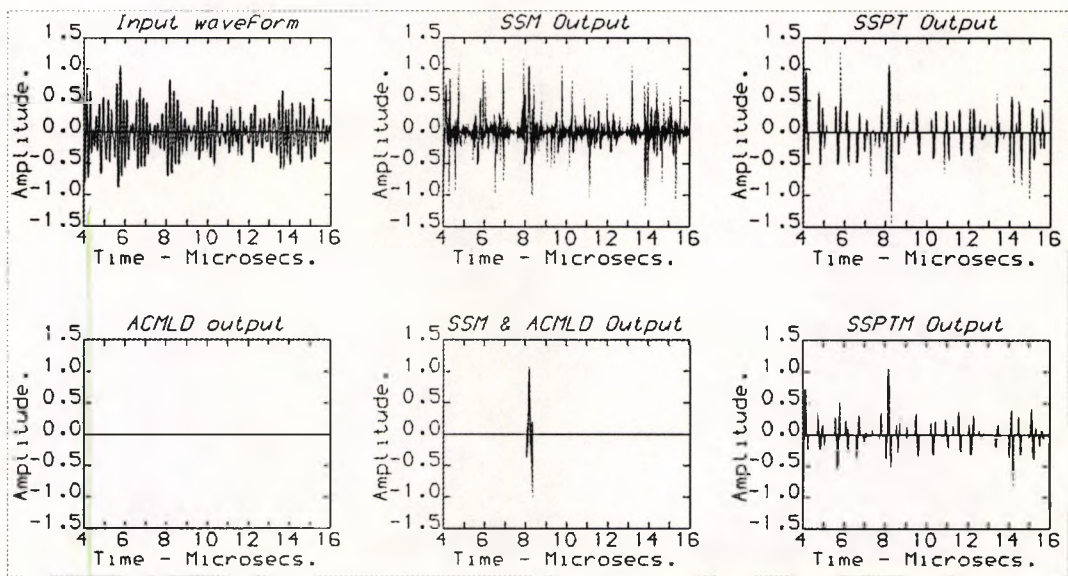


Figure 6.3.14 A typical result of a false alarm from the modified SSM method using the modified method to select optimum parameters as used in Figure 6.3.11.

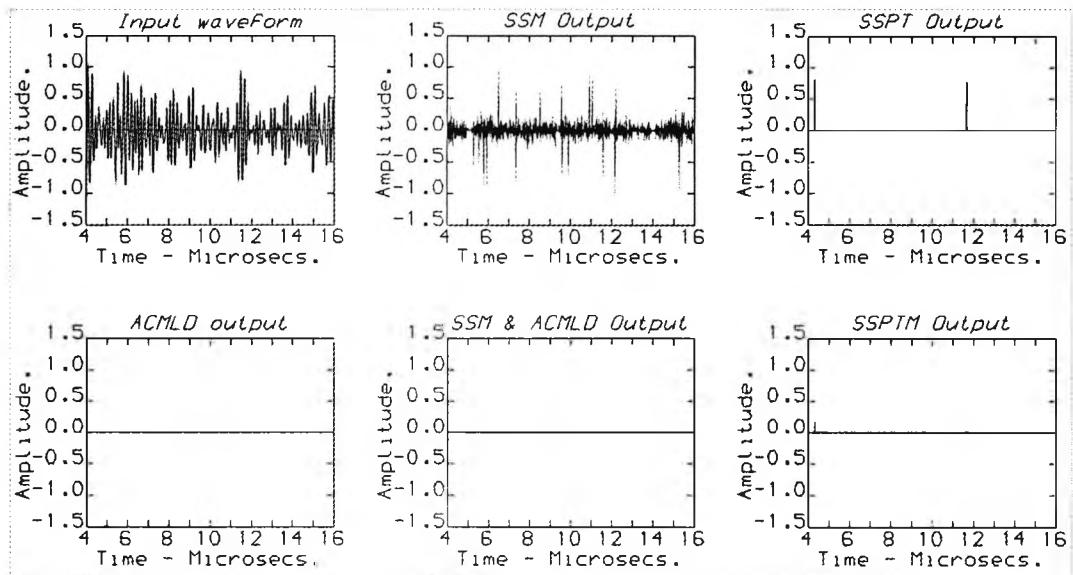


Figure 6.3.15 A typical example of false alarms from results obtained by using the modified SSPT method to select optimum parameters as used in Figure 6.3.11.

ACML-CFAR False Alarm Rate $P_f = 10^{-4}$ Time duration of the cells $T_c = 0.2\mu s$	SSM with $\Delta f = 1/T$ using ACMLD Frequency Range $3 \leq f \leq 6.5$ (MHz) Filter bandwidth $B_f = 0.3$ MHz	SSM with overlaps at half power points using ACMLD Frequency Range $3 \leq f \leq 6$ (MHz) Number of Filters $N = 3$ Iteration Number $N_i = 2$	SSPT with overlaps at half power points Frequency Range $3 \leq f \leq 6$ (MHz) Number of Filters $N = 15$	SSPTM with overlaps at half power points Frequency Range $3 \leq f \leq 6$ (MHz) Number of Filters $N = 15$
Target 1 Indications	5	5	5	5
Target 2 Indications	6	4	1	1
Target 3 Indications	6	4	5	5
Target 4 Indications	5	3	5	5
False Alarms	28	23	14	13

Table 6.3.1 Summary of the processing results from a set of 64 A-scans using various split spectrum processing methods. Some of these (columns 2 and 3) are in conjunction with adaptive detection. The processing parameters are given at the top of each column and were kept constant for each method.

All of the above results in this section can be summarised by means of Table 6.3.1 which gives results for each of the implementations tested using a set of 64 A-scans. The outcome of using Karpur's method is shown in column two and the parameters used for the other three methods have been chosen to give similar true target detection rate. All of the methods eventually find all of the known targets but each also gives a number of false alarms, as shown at the bottom of the table. As an example, false alarms from the modified SSM and SSPT using their optimum parameters listed in the Table 6.3.1 are illustrated Figure 6.3.14 and 6.3.15 respectively. With the current data it would seem that polarity thresholding (SSPT) with the filter overlap points set at the half power level together with minimisation in conjunction with polarity thresholding (SSPTM), gives the least number of false alarms.

6.3.3 Discussion

Extensive tests made to check the sensitivity of SSP methods to parameter values showed that good signal enhancement was only achieved with optimum parameters that are in general different from A-scan to A-scan. From the results shown in Table 6.3.1, it seems that SSPTM offers better overall performance among the three methods but its optimum parameters are more difficult to determine. This is because the optimum number of filters is dependent on the SNR's of the input data which are often unknown *a priori* and/or vary from scan to scan. Furthermore the central frequency separation can not be fixed at $\Delta f = 1/T$, otherwise the filter bank with an optimum number of filters determined from Eq. 4.20 may not be able to cover an optimum processing frequency range. In addition, if the overlap point is not fixed at the half power point, the filter bandwidth can be yet another independent parameter needing to be determined.

Various other approaches have been investigated to systematically set as many of the processing parameters as possible, but it would seem that consistently good performance can only be obtained by choosing the parameters empirically and individually for every A-scan.

It may be concluded that a useful practical compromise is to select the two SSP parameters according to:

- (1) Select an A-scan containing a true signal but with poorest expected input SNR.
- (2) Use the method proposed in Section 6.3.1 to determine the processing frequency range.
- (3) Apply SSPTM with a fixed overlap point and increase the number of filters until the output SNR reaches the maximum.

The parameters so determined can be used to detect the defect signals in other data obtained under the same experimental conditions, provided that the SNR is not lower than used to determine the parameters in (1) above.

6.4 Results: Adaptive filtering

Before presenting results using adaptive filtering it is convenient to discuss the selection of processing parameters.

6.4.1 Processing parameter selection

A major consideration in using adaptive filtering is of course the appropriate selection of the parameters μ_n , α and L (defined in Section 4.2.3). Experiment showed that in the current application the method is not particularly sensitive to the value of any one of these. Furthermore, once the parameters have been chosen for a given set of experimental conditions, it is not necessary to change them as the transducer is scanned over the component being tested. Taking the three parameters in turn, in theory, as is discussed in [Tarrab, M.], the convergence of the NLMS algorithm is guaranteed if $0 < \mu_n < 1$. Tests with the current data showed that good performance of the filter was achieved if $\mu_n \sim 0.01$ and that changing this by a factor of 5 only made a small difference. The sensitivity of the filter to the values of α and L was also tested. Typically, good results were obtained if $0.0001 \leq \alpha \leq 0.1$ and $10 \leq L \leq 20$.

6.4.2 Processing results

Since the performance of the adaptive filter to be used here relies on the noise signal becoming less correlated than a wanted signal as the distance between the A-scan positions of two input channels is increased, the normalised cross correlations between data from a datum position with that at 4 points at increasing distance to one side, have been calculated. Results for both a gated signal and noise alone are shown in Figure 6.4.0 As can be seen in Figure 6.4.0 the wanted signal does indeed have wider cross-correlation width with respect to its "datum" signal than does the noise. For a same transducer position, the cross-correlation between the signals is typically twice higher than is the grain noise. Note that with the current data, the scan increment is close to 1mm.

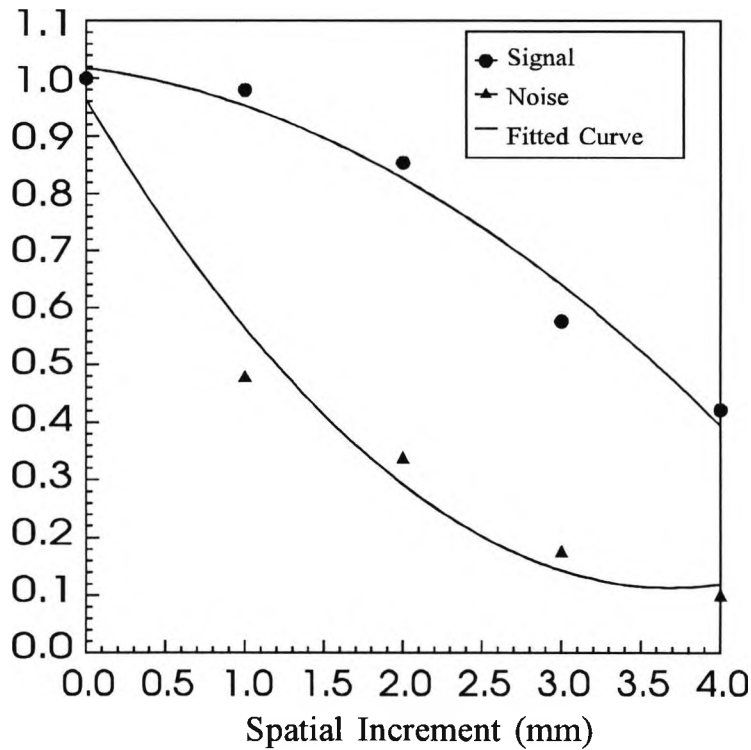


Figure 6.4.0. Cross correlation of signals from a datum position with those at increasing distance to one side. A least-squares fit to a second order polynomial was used to plot the curve.

Figure 6.4.1 shows the two input data channels (a), (b) and the output after (c) adaptive filtering and (d) adaptive detection. The reference signal, $x(k)$ in (b), was captured with the transducer moved by 2mm from the position at which the primary input signal, $d(k)$ in (a) was captured. In addition, the corresponding time domain gain of the NLMS adaptive filter is plotted to the same time scale in (e). This illustrates the typical tracking ability of the NLMS adaptive filter in response to the nonstationary input data. It can be seen that the peak of the time domain power gain of the adaptive filter is coincident with the position of the known target signal labelled FBH. Furthermore, the sharpness of the gain response demonstrates that the convergence speed of the NLMS algorithm is fast enough to track the time-varying characteristic of the input data. Here the relevant characteristic is the cross correlation of the target signal between the primary input and the reference input.

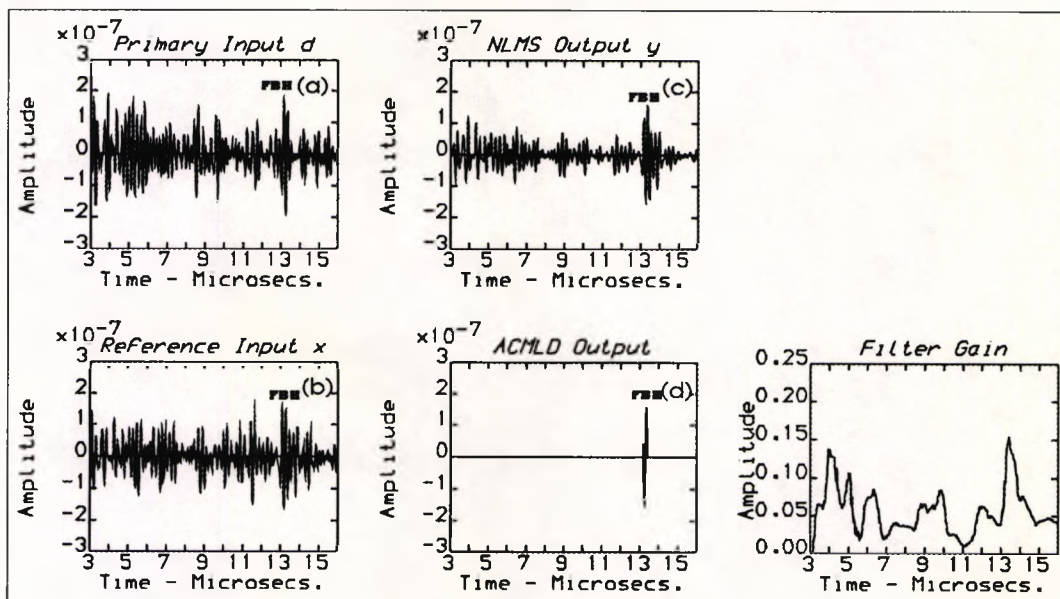


Figure 6.4.1 Ultrasonic A-scan data before (a and b) and after adaptive filtering (c) and detection (d). The test target was a flat-bottomed hole (FBH) of diameter 1.0mm in a Waspaloy test block. An unfocused 5MHz transducer of diameter 20.0mm, was used in transmit receive mode to interrogate the targets. The reference signal, $x(k)$ in (b), was captured with the transducer moved by 2mm from the position at which the primary input signal, $d(k)$ in (a) was captured. The adaptive filter and detector parameters used here were: $L=15$, $\mu=0.01$, $\alpha=0.001$, $P_f=0.0005$, $T_c=0.2\mu s$.

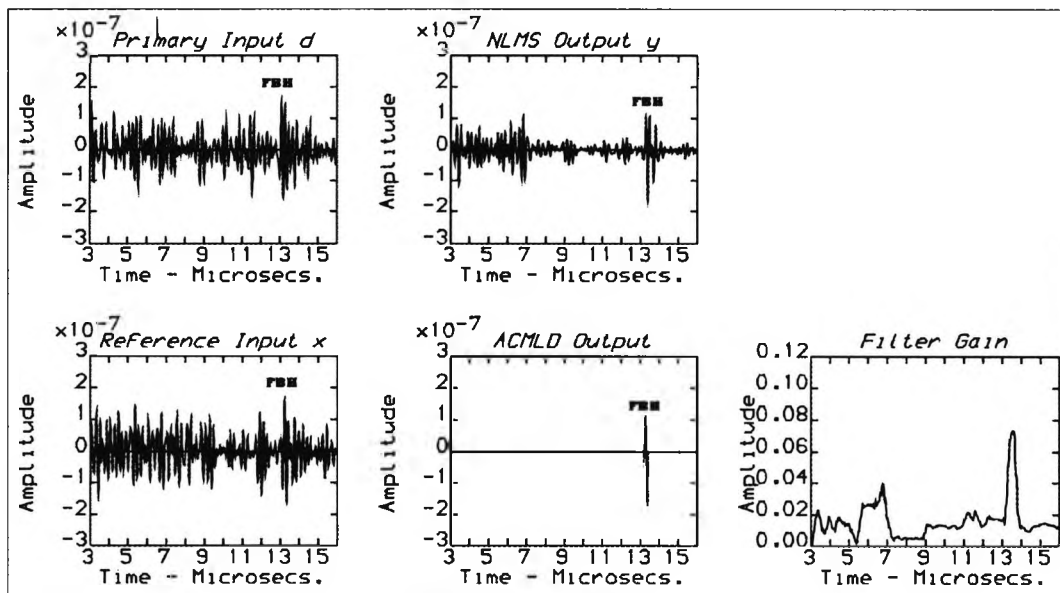


Figure 6.4.2 Results with two adjacent transducer positions as in Figure 6.4.1, but with a displacement of a further 2mm. That is, the reference signal in Figure 6.4.1 became the primary input here. The improvement in signal-to-noise ratio was similar to that of Figure 6.4.1, demonstrating good consistency since it was arranged that the wanted signal would be present in all of the scans considered.

As can be seen in Figure 6.4.1 (c), there was a marked reduction in the grain noise after processing, the input and output signal-to-noise ratios (as defined in Eq. 6.1) being 6dB and 10dB, respectively. The parameters of the filter and detector used here were $L=15$, $\mu_n=0.01$, $\alpha=0.001$, $P_f=0.0005$ and $T_c=0.2\mu s$.

In tests carried out to assess the consistency of the method, and the significance of the time position of a wanted target, fixed parameter values were used to process data taken from different transducer positions and progressively truncated data whilst always retaining the known test signal. The results given in Figure 6.4.2 were taken with the transducer at adjacent positions to those used for Figure 6.4.1. That is with the reference signal in Figure 6.4.1 now used as the primary signal and the next adjacent scan as the reference signal. The improvement in signal-to-noise ratio was similar to that that of Figure 6.4.1.

The following four figures (Figures 6.4.3-6.4.6) show the effect of progressively cutting off 4 μ s from the beginning of the data acquired with the transducer positioned as for Figures 6.4.1 and 6.4.2. This was done to check the ability of the method to cope with a short data stream and with the wanted signal appearing at different positions within the data stream. In all cases, the known signal is correctly identified and the filter gain curve shows a distinct peak at the position of the wanted signal.

Further tests were carried out to quantify the performance of the NLMS adaptive filter by processing the full set of 64 A-scans as used in testing split spectrum processing. To demonstrate that the NLMS filter is not particularly sensitive to parameter values, the same processing parameters were used as those of Figures 6.4.1 - 6.4.6, even though that data was obtained from a completely different test block with a different target size. The results summarised in Table 6.4.1 assume that the only defects present in the Waspaloy test piece examined were those introduced artificially, i.e. the four flat-bottomed holes. Any target indications from areas which did not include a FBH were regarded to be "false alarms". As discussed in Section 6.2, it might be anticipated that there would be up to ten indications for each known target, but with the experimental conditions used here the actual number of true indication per target will be less than this. Again this is partly due to the poor signal to noise ratio but also to the requirement that for the adaptive filter to perform well, the target signals in two adjacent inputs must be better correlated than are the corresponding noise signals. This is more likely to happen around the centre of the beam than it is to either side. In addition, the number of positive indications would be further reduced if the line of scan is not directly through the centre of each target. For all of these reasons, it would be expected that the number of adjacent scans showing detectable indications of the target will be reduced as the material becomes noisier.

As shown in Table 6.4.1, after NLMS filtering and ACML-CFAR processing, all four targets were correctly detected and there were no false alarms.

It should be pointed out that the same processing parameters were used for processing all 64 A-scan data as summarised in Table 6.4.1.

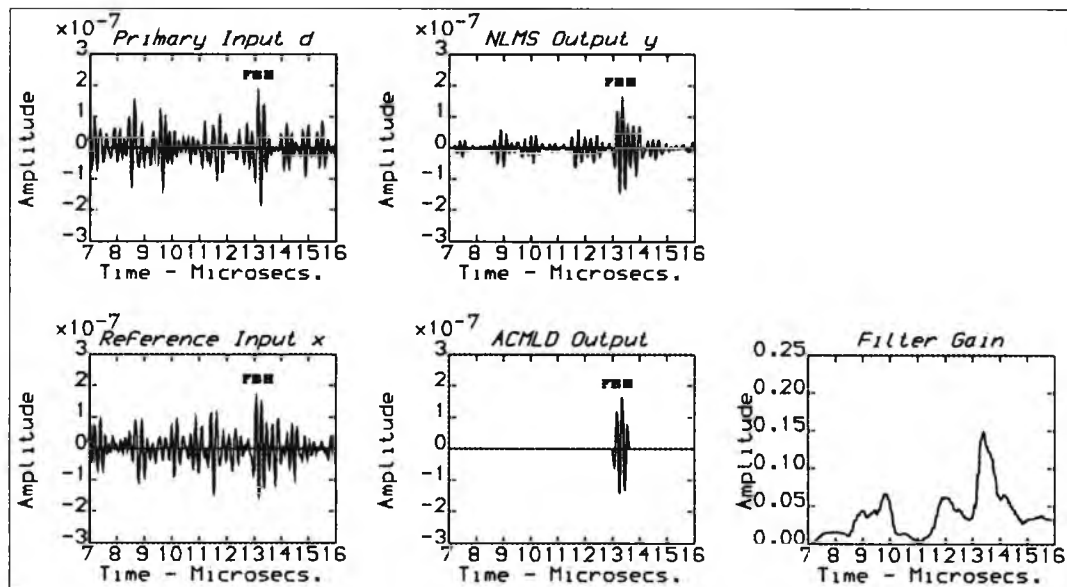


Figure 6.4.3 Results with the transducer in the same positions and processing parameters as for that of Figure 6.4.1, but the data truncated by $4\mu\text{s}$ at the beginning.

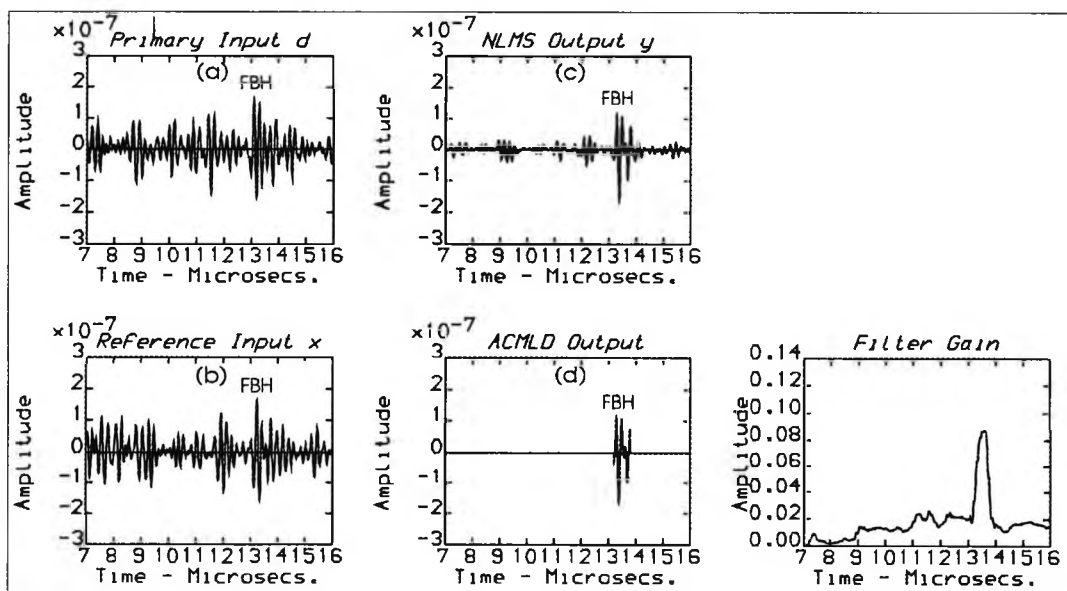


Figure 6.4.4 Results as for Figure 6.4.2, but the data truncated by $4\mu\text{s}$ at the beginning.

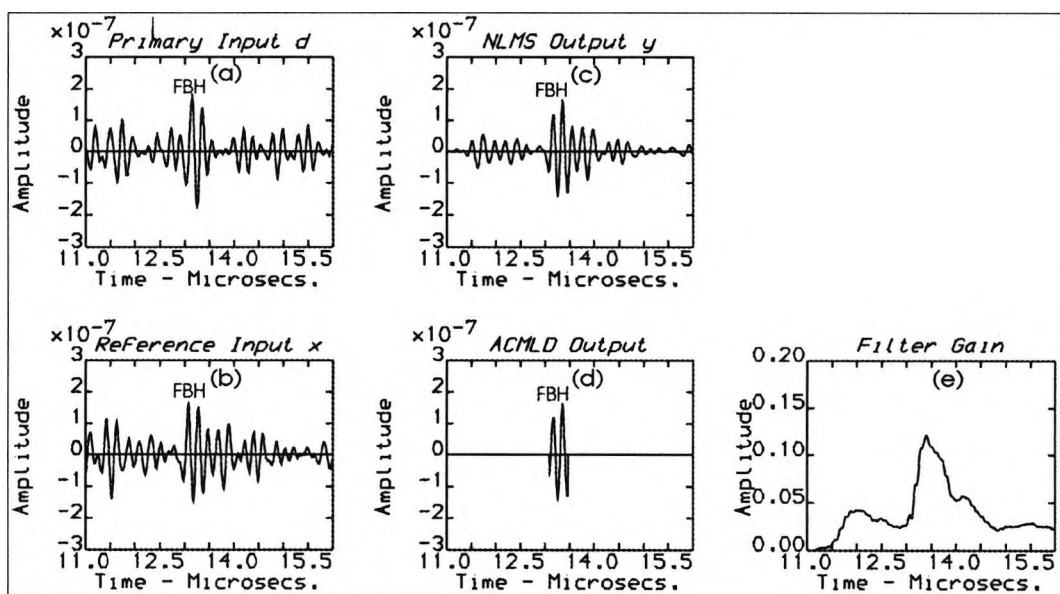


Figure 6.4.5 Results as for Figure 6.4.3, but with a further truncation of $4\mu\text{s}$.

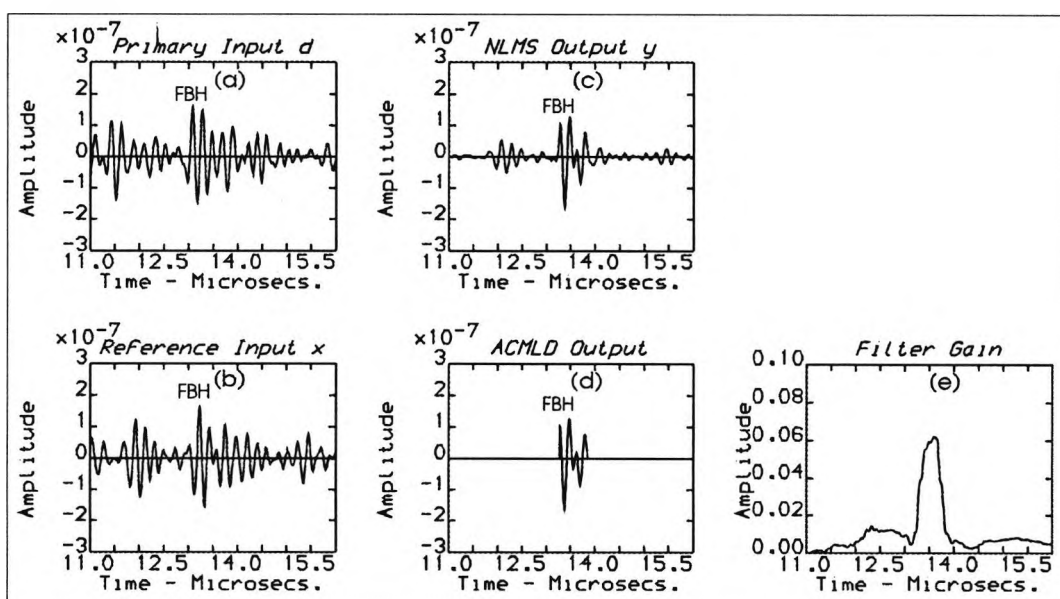


Figure 6.4.6 Results as for Figure 6.4.4, but with a further truncation of $4\mu\text{s}$. Taken in conjunction with the results of Figures 6.4.1-5 this demonstrates that the ability to detect targets at different depths.

Input data: A group of 64 A-scans taken by a 5MHz, 12.7mm diameter unfocused transducer from a Waspaloy Jet engine disc.	NLMS & ACMLD Processing Parameters: $L=15$ $\mu_n = 0.01$ $\alpha = 0.001$ $P_f = 0.0005$ $T_c = 0.2\mu s$		SSPTM Processing Parameters: $3\text{MHz} \leq f \leq 6\text{MHz}$ $N_f = 15$	
Four Known Targets: 0.86mm FBH	No spatial averaging	Spatial averaged	No spatial averaging	Spatial averaged
Target 1 indications	1	3	2	5
Target 2 indications	4	2	0	1
Target 3 indications	3	2	3	5
Target 4 indications	1	1	4	4
Unknown target indications	4	0	17	13
Unknown target positions	3	0	15	6

Table 6.4.1 Adaptive filtering (NLMS algorithm) and detection (ACML-CFAR detector) results for 64 A-scans using constant processing parameters. For comparison some split spectrum processing results are included. The adaptive techniques give greatly improved performance, as the entries for the number of false indications in the bottom two rows shows.

In order to compare the performance of the NLMS adaptive filter with that of split spectrum processing, in particular the SSPTM method, the same 64 sets of A-scan data were also processed by SSPTM, using the same Split Spectrum parameters as in Table 6.3.1. Namely, a frequency range of $3\text{MHz} \leq f \leq 6\text{MHz}$ and with $N_f = 15$. Although, the two methods give a similar number of true target indications, split spectrum processing gives many more false alarms. Furthermore, as has already been discussed, the adaptive filter is much less sensitive to parameter selection than is split spectrum processing.

Another important practical advantage of the adaptive filtering approach over SSP is that the processing time is much shorter than with SSP. In order to make quantitative comparisons of the processing times for the various methods used, approximate formulae for the number of floating point operations (FLOP's) have been derived by inspection of the algorithms used. The formulae and the

corresponding number of Flop's for SSP, NLMS adaptive filtering and the various detection methods evaluated here have been listed in Table 6.4.2. It shows, for instance, that for the typical parameters used here, adaptive filtering is about 10 times faster than SSP.

Algorithms	SSP	NLMS	Fixed Threshold	CA-CFAR	ACML-CFAR
Formula	$5N_f N \log_2 N$	$5LN$	$5N + 3N_c$	$5N + 10N_c$	$5N + 4N_c^2$
FLOP's	$\sim 10^6$	$\sim 10^5$	~ 5300	~ 5700	$\sim 1.5 \times 10^4$

Table 6.4.2 The estimated order of number of FLOP's for various signal enhancement and detection methods. The number of FLOP's are estimated using the same number of input data points ($N=1024$) and typical parameters throughout: the adaptive filter length L and number of SSP filter N_f are the same as used in the Table 6.4.1 ($L, N_f=15$); total number of range resolution cells $N_c=50$.

6.4.3 Results: adaptive filtering with bandpass filtered reference input

To evaluate the effectiveness of adaptive filtering using a bandpass filtered reference input (see Section 4.2.3), two A-scans taken from a Waspaloy test block containing a real flaw were processed. A 10MHz, 12.7mm diameter, weakly focused transducer ($f_f = 15\text{cm}$) was used in obtaining the data.

Figure 6.4.7 shows (a), the gated real flaw signal and (b) its spectrum. Corresponding results after bandpass filtering are shown in (c) and (d) respectively. The bandpass filter was chosen according to the arguments given in Section 2.1, with filter length $L_b=30$ and frequency range $8\text{MHz} \leq f_b \leq 9\text{MHz}$. For comparison, results for a representative sample of gated grain noise obtained from the same test piece under the same experimental conditions are presented in Figure 6.4.8. As can be seen from Figure 6.4.7 and Figure 6.4.8:

- (1) The higher frequency band is more predominant in the grain noise than in the target signals.
- (2) In the frequency domain, the defect scattering on the whole fluctuates less than does the grain noise.
- (3) The defect signal is essentially unchanged after bandpass filtering. In contrast, a gated section of typical grain noise is dramatically changed in both the time and frequency domain after the filtering.
- (4) As might be anticipated, the bandpass filter appears to make the wanted signal and the noise look similar, however the crucial effect is that it reduces the correlation between the noise in each input channel.

Based on these disparities, an attempt has been made to improve signal enhancement by further decorrelating the noise (see section 6.4.2) using a bandpass filter in the reference channel of the adaptive filter. Some representative results are shown in Figure 6.4.9. The primary and unfiltered reference inputs containing a real flaw signal are shown in (a) and (b), respectively. The output of the adaptive filter with unfiltered reference input (b) is illustrated in (c). The adaptive filter output with bandpass filtered reference input (d) is shown in (e). The parameters used were: bandpass filter length $L_b=20$, frequency range $8\text{MHz} \leq f_b \leq 9\text{MHz}$, time delay $\delta t=0.2\mu\text{s}$, filter length $L=10$, convergence step size $\mu=0.03$ and $\alpha=0.01$, false alarm rate $P_f=10^{-4}$, cell duration $T_c=0.1\mu\text{s}$. It can be seen that although the SNR in both the unfiltered and filtered reference input channels ((b) and (d)) are similar, the SNR in the output of the adaptive filter (c) with bandpass filtered reference input (d) is evidently enhanced more than that in the output of the adaptive filter (c) with unfiltered reference input (b). The flaw signal is correctly detected in the consequent output of the adaptive detector as shown in (f). Tests made using the same detector settings showed that the flaw could not be detected without bandpass filtering. It should be pointed out however, that a drawback of using a bandpass filtered reference input is that it will certainly increase the processing time and introduce additional parameters requiring to be optimised.

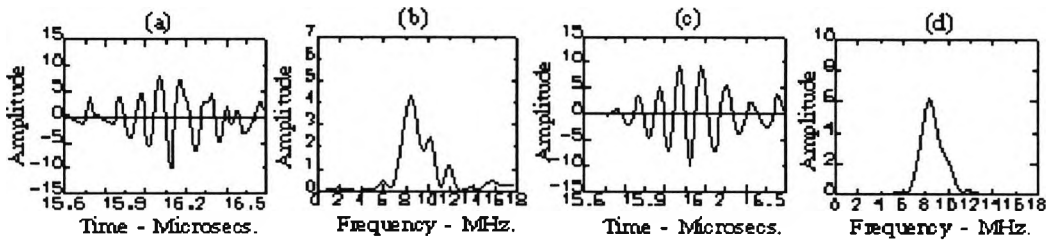


Figure 6.4.7 A typical (gated) real flaw signal before and after bandpass filtering. The flaw signal and its spectrum are shown in (a) and (b), respectively and (c) and (d) give the corresponding signals after filtering.

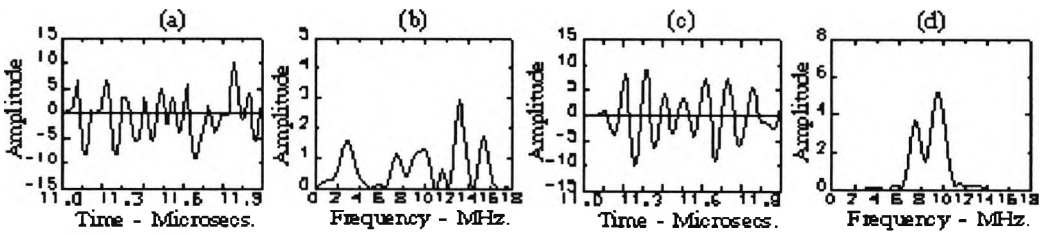


Figure 6.4.8 Gated grain noise before and after bandpass filtering displayed in same order as in Figure 6.4.7 and using the same filter.

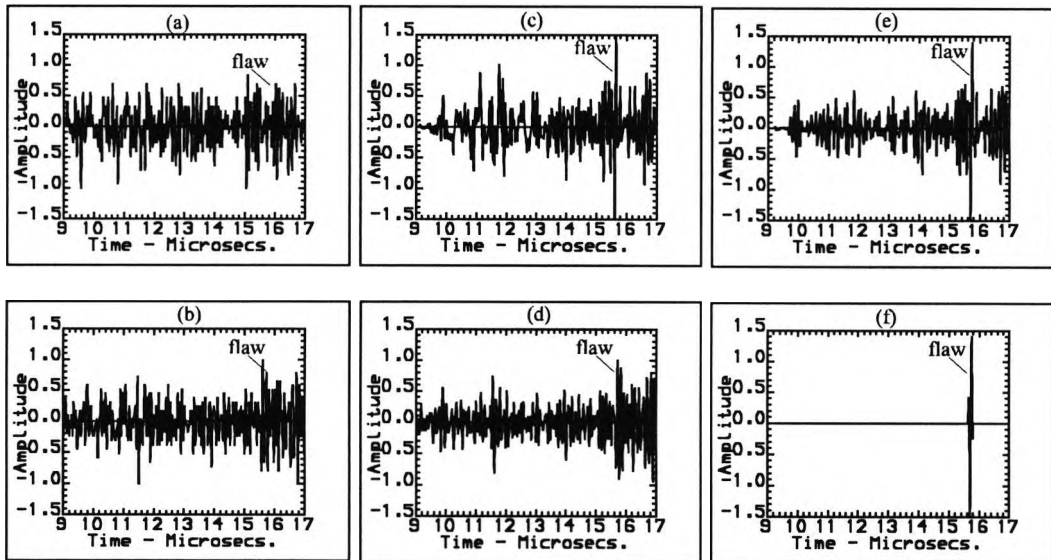


Figure 6.4.9 A-scan data containing a real flaw signal before and after adaptive filtering. The primary and unfiltered reference inputs are shown in (a) and (b), respectively. The results of adaptive filtering with and without bandpass filtering are shown in (e) and (c), respectively and (f) shows the flaw signal as identified by the adaptive detector (using bandpass filtering).

6.4.4 Processing results using a non-uniformly excited high-resolution transducer

So far all of the data has been obtained using conventional transducers. Here some results for data obtained by using a specially developed transducer are presented. The transducer was designed to give lateral resolution an order of magnitude better than that of a conventional transducer of the same aperture and bandwidth. The new transducer is an example of an edge-wave-only-transducer, in which the excitation is controlled in an axisymmetric pattern, strong at the rim and rapidly falling off towards the centre. Such transducers were first developed at City University by Dr J.P. Weight [Weight, J.P., 1982].

Full details of the theory, construction and evaluation of our transducers have appeared elsewhere [Weight, J.P., 1986], but very briefly, a conventional circular transducer radiates a locally plane wave in the geometric region straight ahead of its aperture, together with a spreading "edge" wave which propagates in all directions from its rim. All aspects of the beam structure result from the existence of these plane and edge waves and from the interference between them whenever they overlap. For instance, the fact that the near field lateral resolution of a conventional transducer approximates to its diameter is due to the extent of the plane wave radiated. Edge-wave-only-transducers seek to give improved resolution by shading out the plane wave, so that just the edge wave is radiated. The good resolution stems from the fact that as a result of circular symmetry, only a target lying right on the transducer axis will simultaneously receive energy from each element of the transducer rim. Furthermore the directivity of the edge waves is such that the good resolution is maintained over a depth range of a few transducer diameters. On reception, the scattering from a target will only be received simultaneously when the target lies on axis. For small targets, the sensitivity of an ideal edge-wave-only transducer approaches that of a conventional transducer of

the same size. For larger, flat and perpendicularly-aligned targets, the sensitivity is less than with a normal transducer, since in effect only a small region of the target surface is being interrogated

An approximately edge-wave-only transducer suitable for the current application has been constructed by the author. The transducer was modified from a Panametrics V307 probe with a centre frequency of 5MHz and diameter 25mm. It consists of a small modified front-face electrode in a ring configuration and the existing complete back-face electrode. The first step was to remove the existing matching layer and electrode and attach an insulating disc with a diameter just less than that of the piezoelectric element. A very thin layer of epoxy resin was used to fix a standard diameter microscope cover slip to form the insulating layer. A conductive layer of silver was then applied over the whole front face using a sputtering system. This film provided both the ring like electrode where it contacted the transducer element and a screening layer over the insulating disc. The screening layer greatly reduces the pick-up of unwanted RF noise, especially that from the stepper motors used in the transducer scanning system. The ring electrode configuration gives rise to field fringing which results in an approximation to the nonuniform excitation required to generate edge waves only. A brief experimental evaluation of the approximate EWO transducer was made to confirm its good lateral resolution over the depth range of current interest. More detailed theoretical and experimental evaluation of a similar transducer can be found in [Weight, J.P., 1982] and [Weight, J.P., 1984].

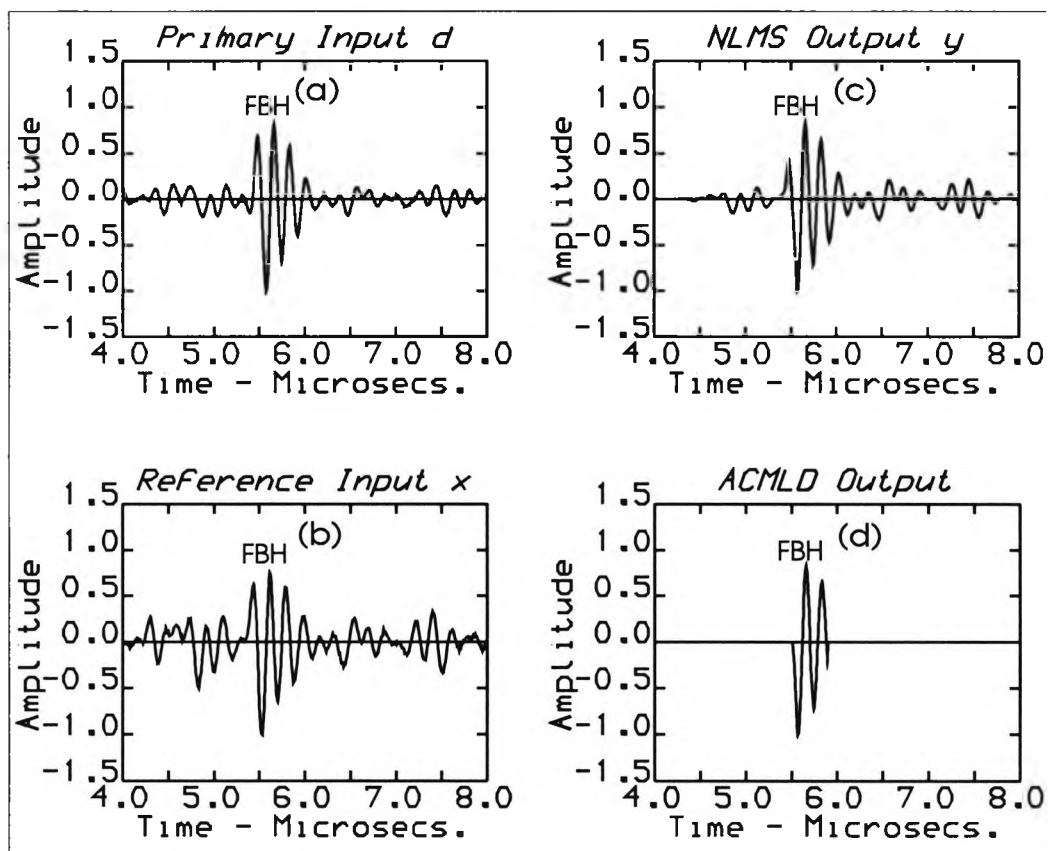


Figure 6.4.10 Adaptive filtering and detection methods applied to data captured by a non-uniformly excited transducer - an edge-wave-only transducer. Here (a) and (b) are the primary and reference input respectively. The output from the filter and detector are shown in (c) and (d). Comparison of (b) and (c) shows that the grain scattering is reduced.

Figure 6.4.10 and Figure 6.4.11 show A-scans obtained using the new transducer to interrogate two test pieces similar to those used in obtaining the results of Figures 6.4.1 - 6.4.6. Both blocks contained a single flat-bottomed hole of diameter 1mm, the metal paths to each target being 15mm and 38mm, respectively. Since the typical beam width of the EWO transducer is about one tenth that of a conventional transducer of the same aperture, the scan increment has been also reduced accordingly in obtaining these A-scans. This is necessary to maintain the cross-correlation of the target signals between the adjacent A-scans required by the adaptive filtering.

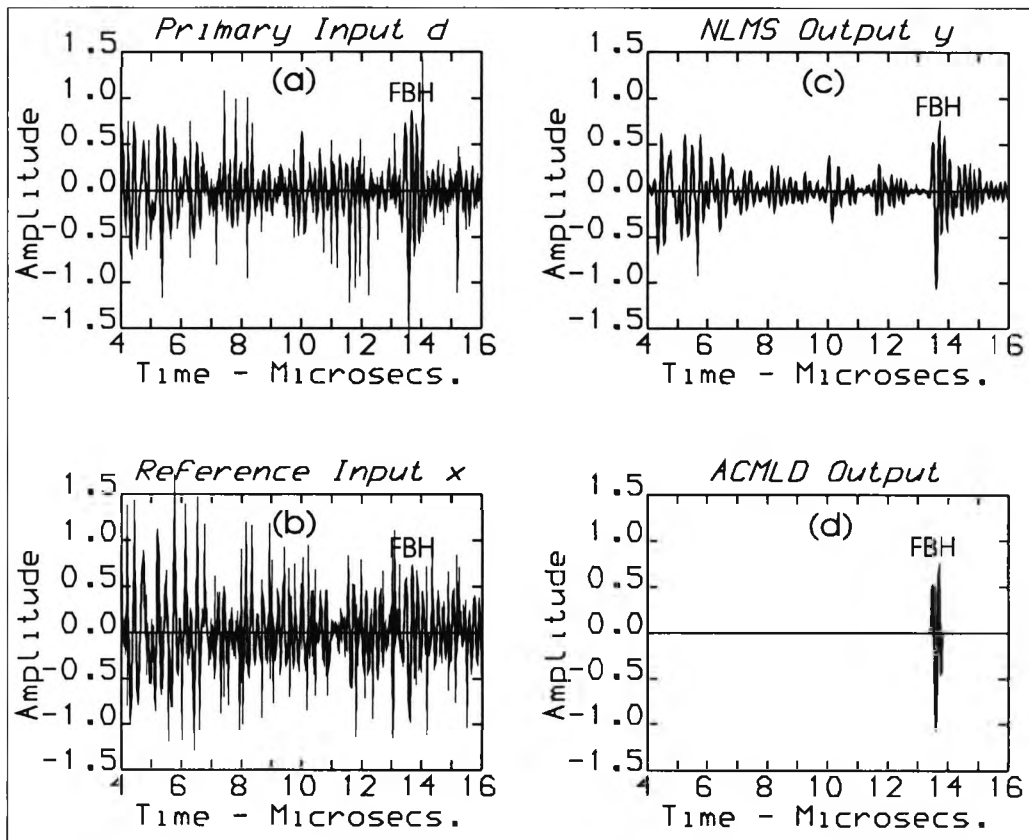


Figure 6.4.11 Similar to the results shown in Figure 6.4.10 but for a deeper target at 38mm. Again, there is significant reduction of the unwanted grain scattering.

The results obtained from the target lying at 15mm (Figure 6.4.10) show quite good signal-to-noise ratio even before processing, but some reduction in the noise is still evident and the wanted signal has been correctly identified by the ACML detector. However a dramatic improvement in signal-to-noise ratio is shown in Figure 6.4.11 which gives the results for the deeper target. For this target, it was not possible from the original data to reliably detect the signal, with any detection methods used. But as illustrated in Figure 6.4.11 after adaptive filtering the wanted signal was correctly detected by the ACML detector.

6.5 Results: Optimal time-space array processing and image enhancement techniques

A set of 64 A-scans including four test targets were used to evaluate the array and image processing. The data were taken from the JED test piece by the NDT department at Rolls-Royce using an unfocused, 5MHz, 12.7mm diameter probe, digitised at a sampling rate of 100MHz and 8 bit resolution.

The four test targets included three FBH's - two at 0.64mm diameter and another at 0.89mm and a two-feature target (hereafter, "double" FBH) composed of one smaller FBH of 0.64mm diameter drilled into the bottom of a FBH of 0.89mm diameter. Schematic diagrams showing the target configurations and the corresponding idealised B-scan image are shown in Figure 6.5.1 and Figure 6.5.2, respectively. The validity of the schematic diagram Figure 6.5.2 was confirmed experimentally using a larger "double" FBH (a FBH of 0.89mm diameter drilled into the bottom of a FBH of 1.14mm diameter) and positioned at the less "noisy" section of the JED test-piece. The three A-scans illustrated in Figure 6.5.3 were obtained with the transducer carefully aligned so that beam axis was perpendicular to the test piece surface. In the central result, the target lies on the beam axis, the two adjacent scans being taken with the transducer ± 2 mm off axis. These results show that when scanning the transducer across the "double" FBH, the echo signals from the shoulder of the "double" FBH have similar variation as the echo signals from the bottom of the "double" FBH but the amplitude of the signal from the shoulder is much smaller. The set of 64 A-scans to be processed here was taken from a more noisy part of the disc resulting in signal to noise ratios at least 12dB worse than those of the data shown in Figure 6.5.3. So, the signal corresponding to

the shoulder of the "double" FBH will be smaller than the grain scattering and will be much more difficult to detect than the signal from even the smaller FBH's. For convenience of comparison between the target configuration and the processed images, the time range and A-scan numbers indicated are the same as those to be used later when presenting false colour B-scan images of the test piece.

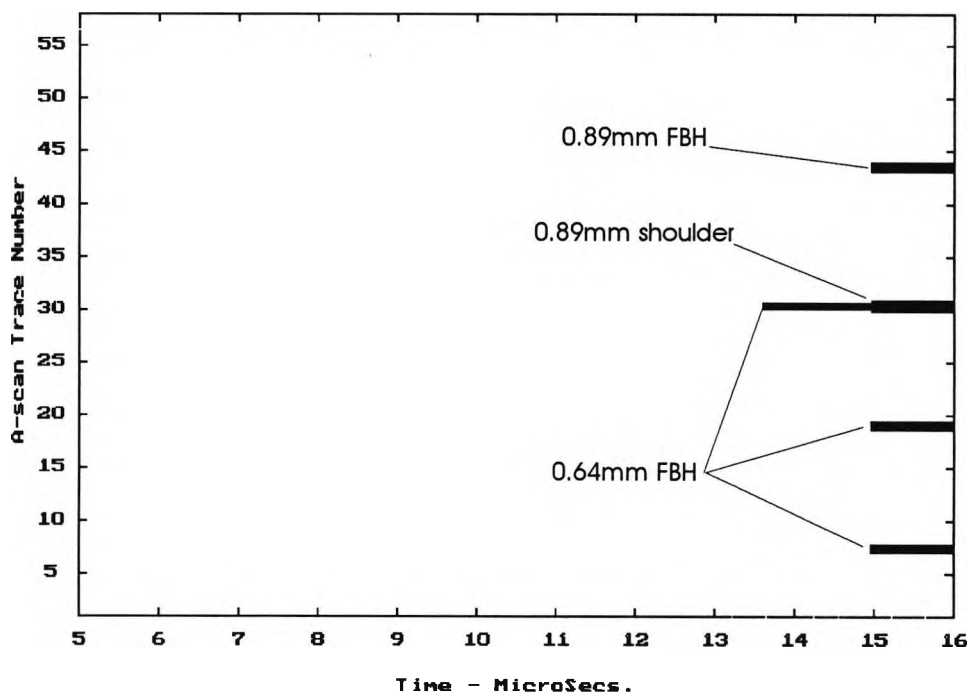


Figure 6.5.1 A schematic diagram of the test target configuration. The dimensions stated are for hole and shoulder diameters - note that the diameters of the holes are not shown to scale but the position of each hole bottom is.

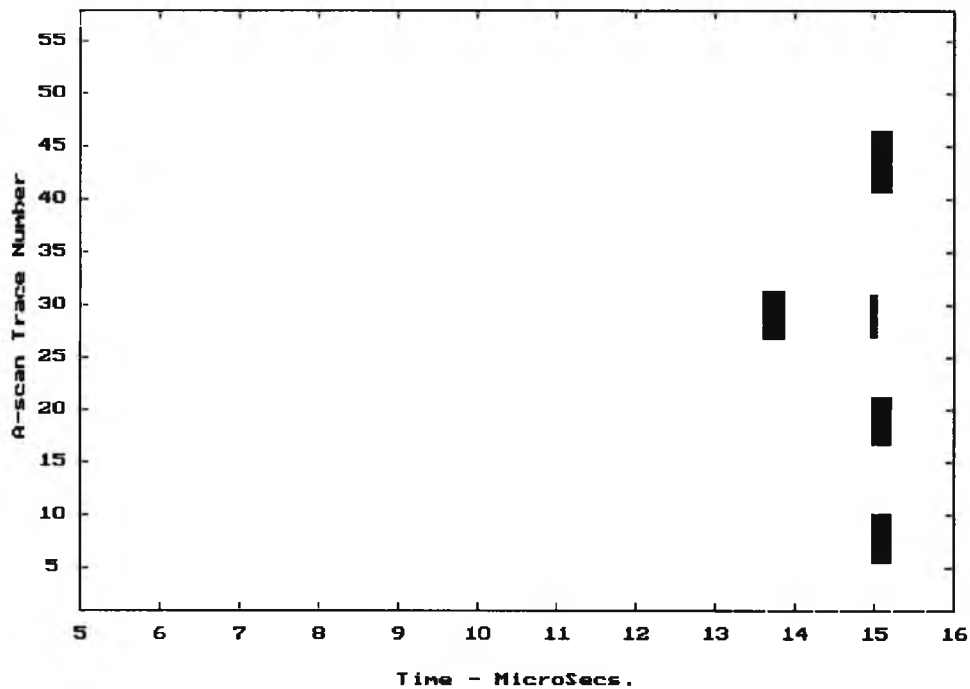


Figure 6.5.2 Anticipated B-scan image corresponding to the test target configuration shown in Figure 6.5.1.

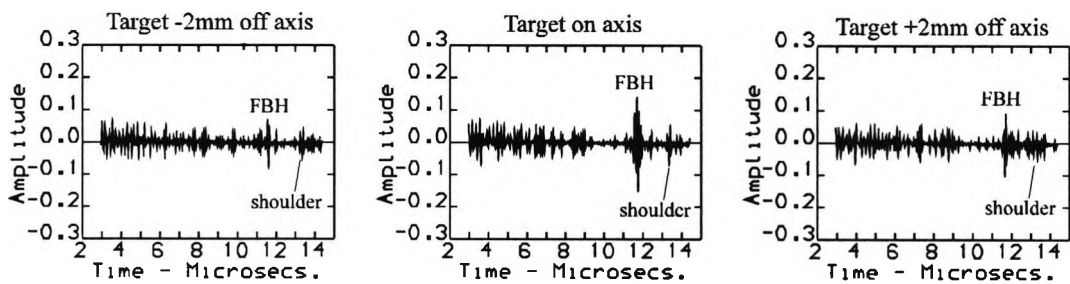


Figure 6.5.3 The three A-scans were obtained with the transducer carefully aligned so that beam axis was perpendicular to the test piece surface. In the central result, the target lies on the beam axis, the two adjacent scans being taken with the transducer ± 2 mm off axis.

Two types of B-scan false-colour images are used to present the experimental and processed results in this section. The first is a B-scan waveform image with the amplitude emphasised by (point-by-point) changing the trace colour with signal amplitude, according to the linear three colour scale included in Figure 6.5.4. The second is a B-scan intensity image with waveform intensity in false colour scale. In the B-scan intensity image, the colour of each pixel is determined by the power of the waveform amplitude according to a linear colour scale with fifteen colour steps as shown in Figure 6.5.7.

6.5.1 Time-space array processing based on optimal waveform estimation

A waveform image constructed from the original unprocessed data is shown in Figure 6.5.4. It can be seen that, due to the strong masking effect of the grain scattering, it is very difficult to identify the four defect positions from just this picture.

Spatial averaging can smooth out some of the grain noise as shown in Figure 6.5.5, where each trace represents an average of 6 adjacent A-scans, taken as the data was recorded. However it is still not possible to reliably locate all of the targets. Note that to aid direct comparison of each method, all of the waveform images have been normalised to the same amplitude scale.

A significant improvement in image quality can be obtained by applying MVDR time-space array processing. The signal-to-noise ratio (see Eq. 6.1) of the image has been enhanced by 7dB. The following parameters were used: number of input channels $M = 6$; processing window length $N = 64$. Now the four target

signals can be visually identified in Figure 6.5.6 at the locations which have significant number of points with the red colour that represents the high amplitude levels. However the signals corresponding to the shoulder of the "double" FBH are still too small to be seen.

To demonstrate the processing effects, the above results were also presented in B-scan intensity image format as shown in Figure 6.5.7-Figure 6.5.9 accordingly.

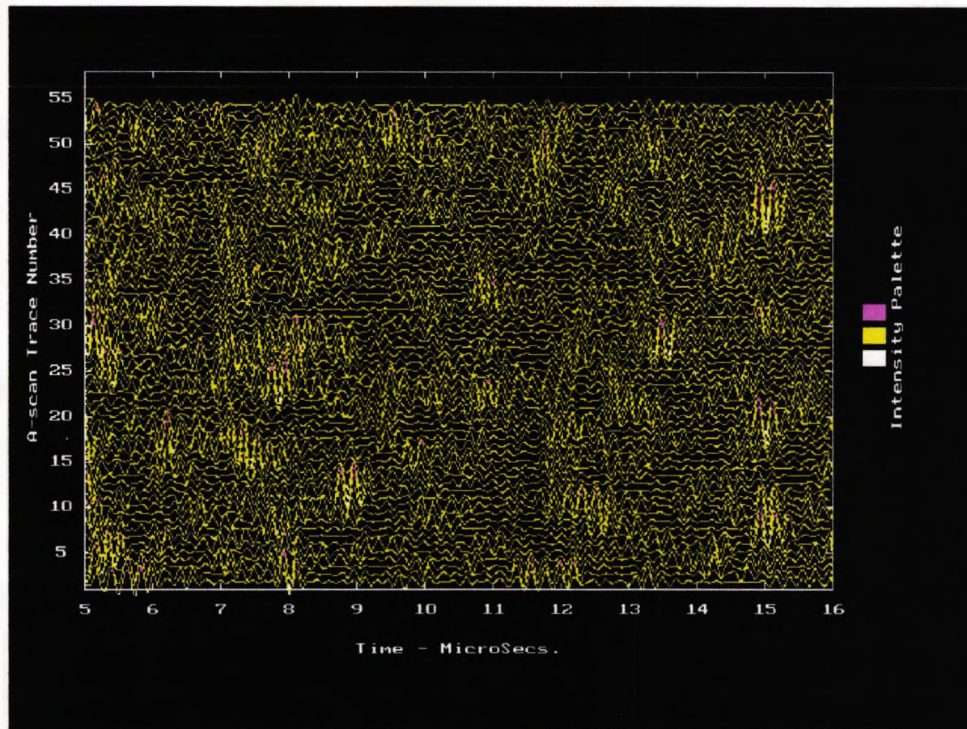


Figure 6.5.4 The original unprocessed 64 A-scans.

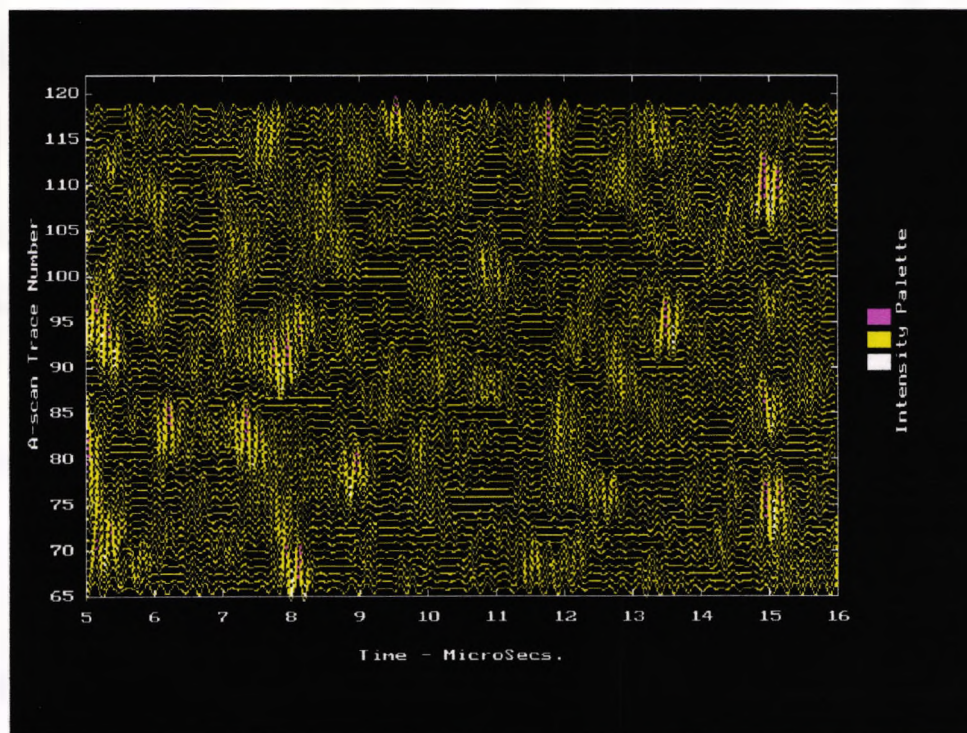


Figure 6.5.5 Spatial averaged result provided by Rolls-Royce for the same test block and A-scans as in the Figure 6.5.4. It shows that some of the defect signals are even less visible than some of the grain noise.

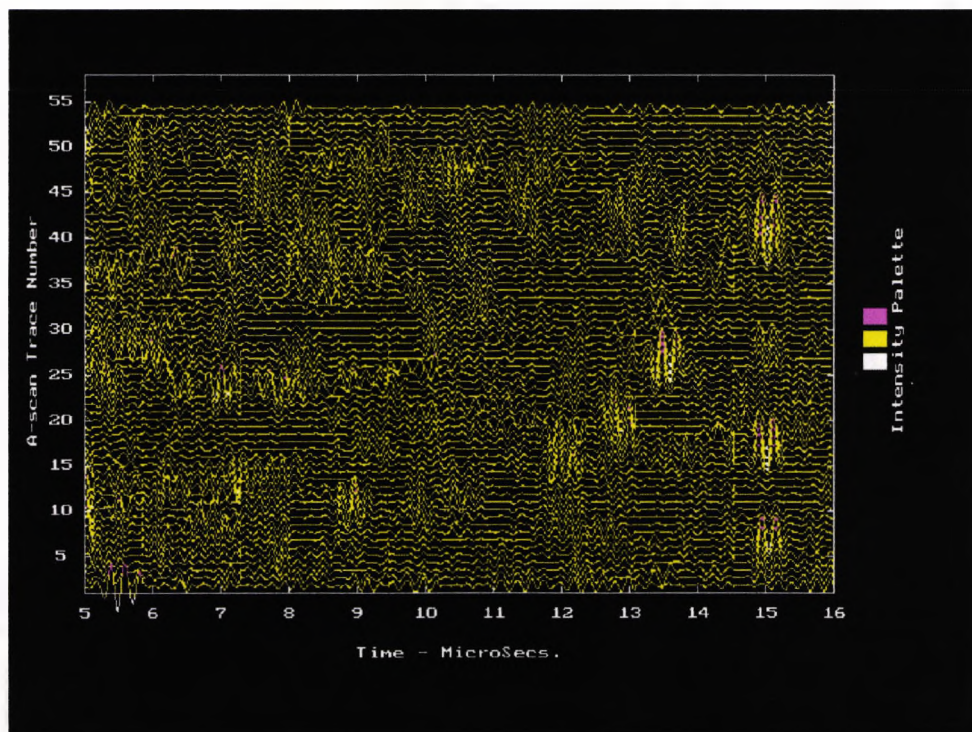


Figure 6.5.6 Result from time-space array processing based on optimal waveform estimation. The signal-to-noise ratio of the image has been enhanced by 7dB.

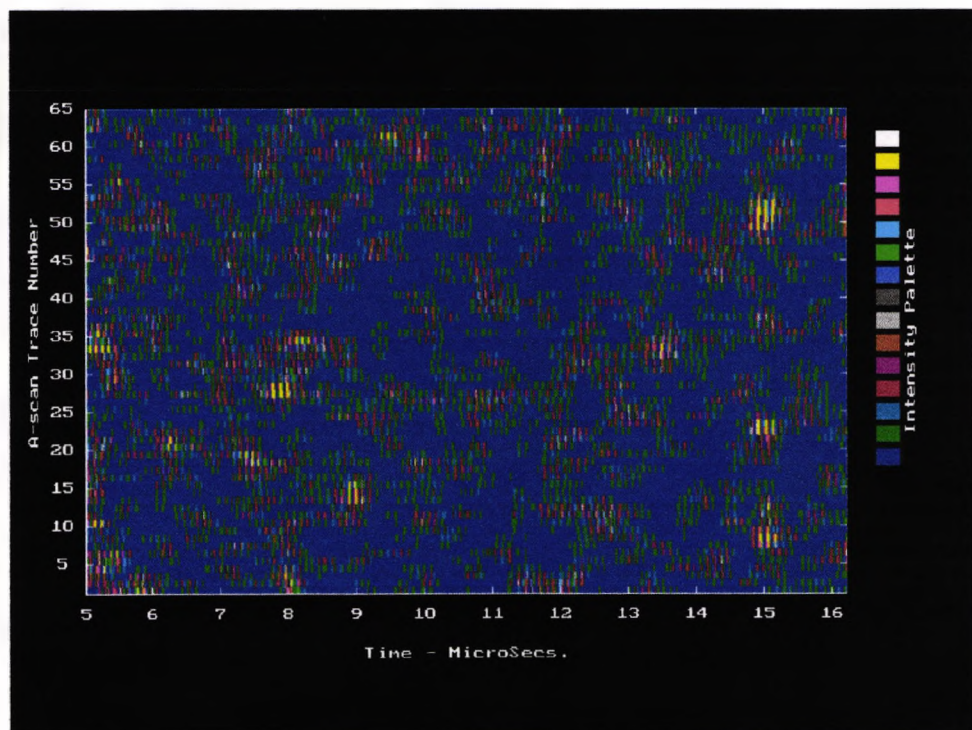


Figure 6.5.7 The false colour image of the same original A-scan data as shown in the Figure 6.5.4 - the original unprocessed 64 A-scan data.

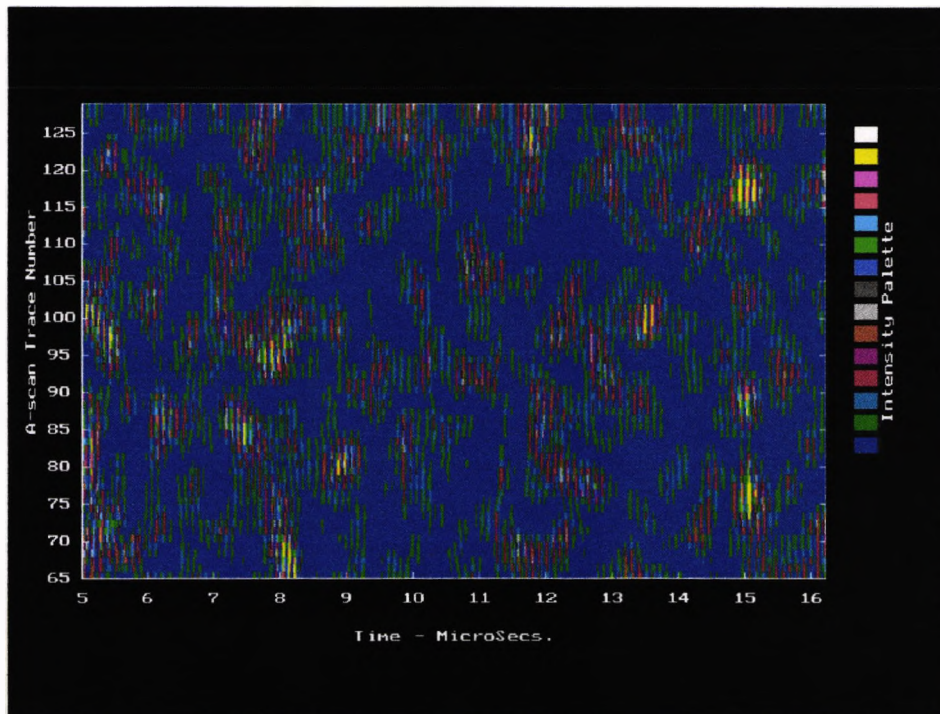


Figure 6.5.8 The false colour image of the same spatial averaged A-scan data as shown in the Figure 6.5.5.

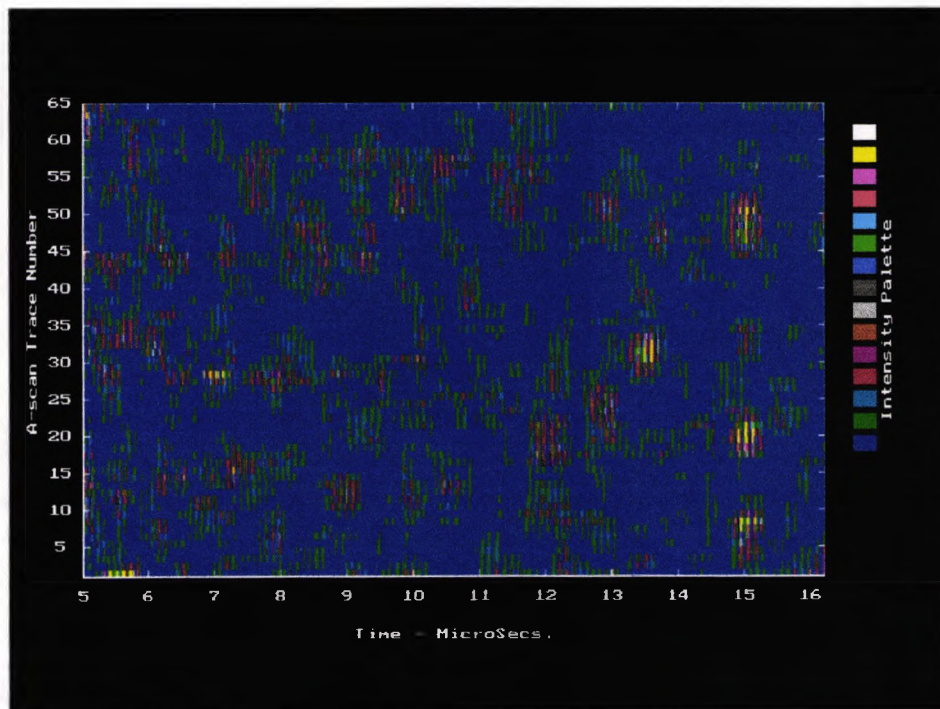


Figure 6.5.9 The false colour image of the A-scan data processed by optimal time-space array processing method, same as shown in Figure 6.5.6. The four distinct target signals can be clearly identified. The signal-to-noise ratio of the image has been enhanced by 7dB.

6.5.2 Adaptive Wiener filtering

The two dimensional adaptive Wiener filtering method described in Chapter 5 has been applied to process the same A-scan data (Figure 6.5.4) as used in obtaining the results of Figure 6.5.6 and Figure 6.5.9. The processing cell consists of 6 traces and each trace was windowed to contain 32 samples.

In order to give a consistent comparison, the unprocessed A-scan data (Figure 6.5.10), the spatial averaged A-scan data (Figure 6.5.11) and the A-scan data after adaptive Wiener filtering (Figure 6.5.12) are all presented in normalised format and applied with the same attenuation factor $\alpha = 0.8$.

It can be seen from the result after adaptive Wiener filtering in Figure 6.5.12 that the time-space domain contrast and sharpness were greatly enhanced compared to both the unprocessed A-scan data (Figure 6.5.10) and the spatial averaged result (Figure 6.5.11). The four defect spots can now be distinguished from the grain noise by their significant number of red colour points shown in Figure 6.5.12 or yellow colour points in Figure 6.5.13. These colours are indications of the high signal amplitude or intensity levels. The signal-to-noise ratio of the image has been enhanced by 15dB. This is achieved by the non-linear processing based on the differential information extracted from the local image and its surrounding image of the time domain input signals. That is, if the local image variance is greater than the variance of its neighbouring image, the output signal amplitude will be proportional to its input signal amplitude, otherwise, the output signal amplitude will be set equal to the local mean. Typically, the areas filled with straight lines in the processed result (Figure 6.5.12) correspond to the regions where the waveform amplitudes were set to their local means.

It should be noted that, although after adaptive Wiener filtering some strong grain scattering is still present, the overall contrast of the target image is visibly greater than that of the grain noise. Whereas before the filtering their contrasts are very similar.

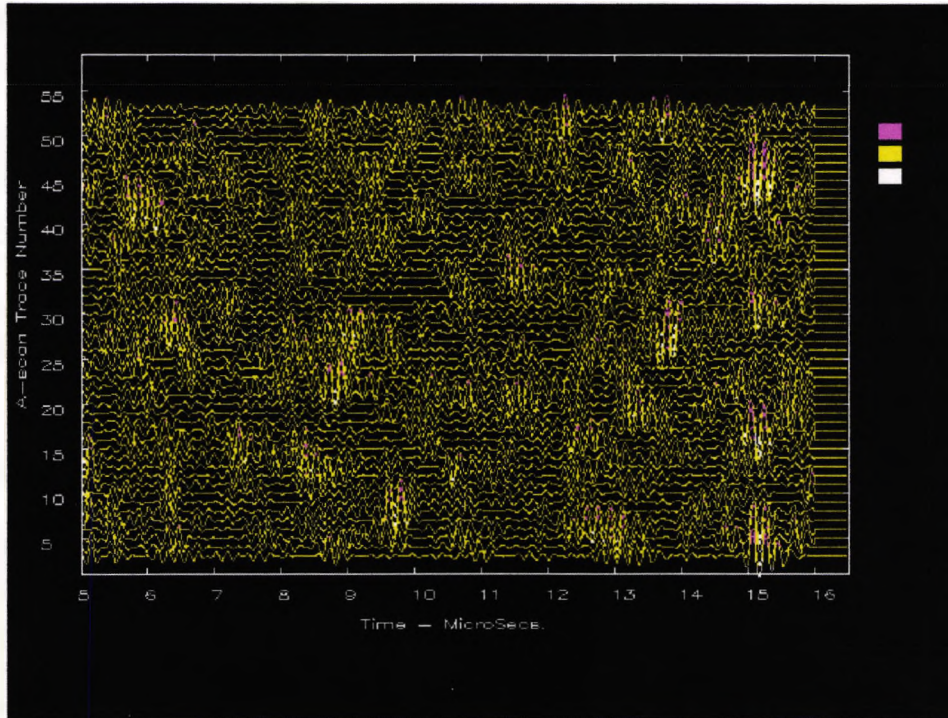


Figure 6.5.10 The same test block and A-scan as in the Figure 6.5.4 but with additional attenuation compensation. The attenuation factor used here is $\alpha = 0.8$.

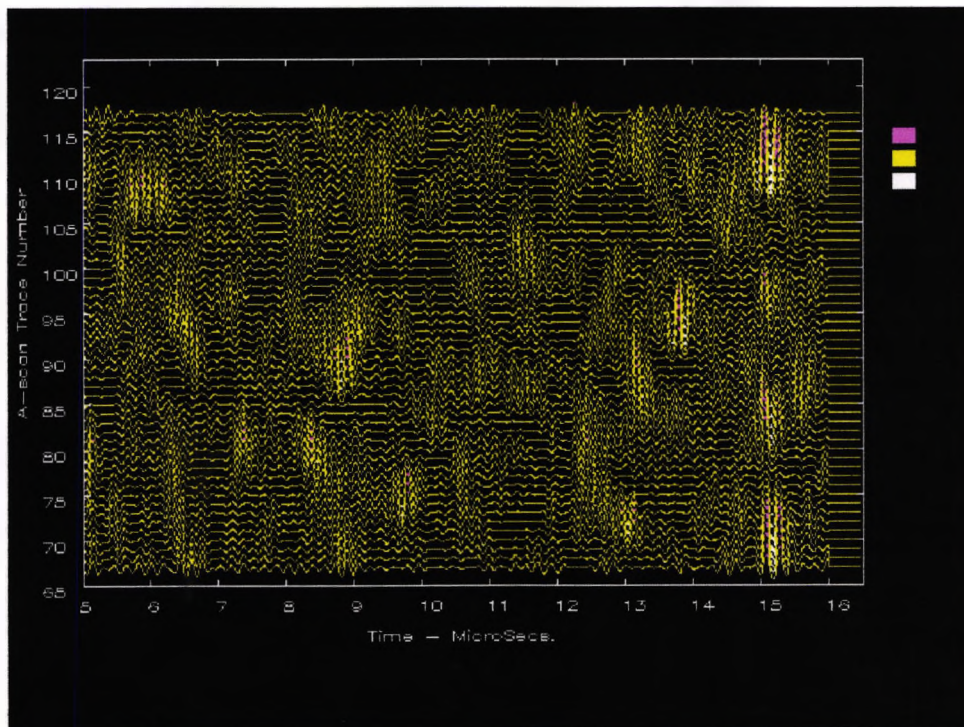


Figure 6.5.11 The same spatial averaged result as shown in Figure 6.5.5 but with additional attenuation compensation. The attenuation factor used here is same as used in the Figure 6.5.10 ($\alpha = 0.8$).

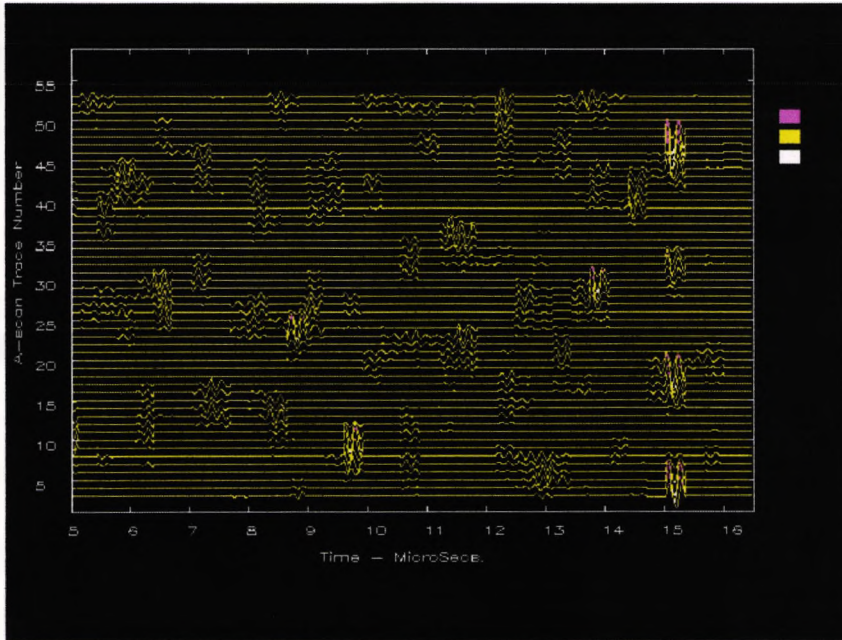


Figure 6.5.12 Output of two-dimensional adaptive Wiener filter for the same input A-scans as shown in Figure 6.5.4. The attenuation factor used here is same as used in the Figure 6.5.9 and Figure 6.5.11 ($\alpha = 0.8$). Here the contrast and sharpness of the four defect spots were remarkably enhanced.

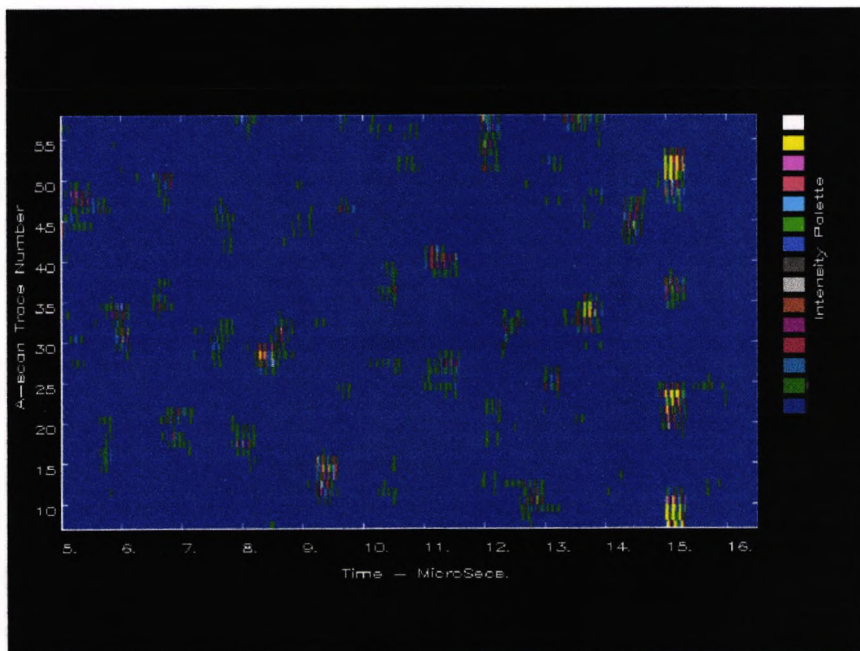


Figure 6.5.13 The false colour image of the 64 A-scans processed by Wiener filtering, same as shown in Figure 6.5.12 ($\alpha = 0.8$). The signal-to-noise ratio of the image has been enhanced by 15dB.

6.5.3 Discussion

From the above results, it can be seen that both optimal time-space array processing and two-dimensional adaptive Wiener filtering can greatly enhance the visibility of defect images masked by grain scattering noise. Both methods offer better overall performance than that of spatial averaging.

On comparing two-dimensional adaptive Wiener filtering to optimal time-space array processing, we can see that the Wiener filter enhances the sharpness and contrast of the images to a greater extent. However, it is a non-linear method that distorts the waveforms. This of course would not be a problem if the enhanced images are interpreted visually according to colour thresholding and no further processing requiring original waveform information is planned. Furthermore, the assumption of an exponential attenuation model may introduce additional artificial effects. In contrast, optimal time-space array processing is a linear method without any attenuation compensation, and therefore keeps the original signal waveform undistorted. This feature can be useful for further automatic pattern recognition processing, such as defect identification, location, sizing and classification, but time-space array processing is much more computing intensive than is Wiener filtering. On the other hand, the adaptive Wiener filter used to produce the result shown in Figure 6.5.12 is only based on the time-space domain local mean and variance. This results in that the overall processing effects are mainly represented as enhancement of contrast and sharpness of image. However the performance of the adaptive Wiener filter can be enhanced further, if more detailed statistical features that can discriminate the defects from the grain scattering could be exploited in the processing.

7. Conclusion

A number of signal processing methods, have been developed and evaluated for ultrasonic quantitative non-destructive testing of highly scattering materials. The processing involves signal enhancement, signal detection and image enhancement. The data considered is for the case of targets in materials with inhomogeneous grain structure, the target dimensions being similar to the average grain size and the dominant wavelengths of the interrogating pulses. For such circumstances, the theoretical and experimental investigations presented here have shown that fixed threshold detection methods widely used in industry are not capable of reliably detecting targets. A major problem with fixed thresholding is that even after the signals have been enhanced, and for a single test piece, the detection false alarm rate will vary exponentially with the noise variance. Much better detection performance has been achieved here by novel applications of adaptive thresholding methods. In particular, methods originally developed for radar applications, such as constant false alarm rate (CFAR) based cell-averaging detector (CA-CFAR) and automatic censored mean level detector (ACML-CFAR), have been adapted and applied to the current application. Such approaches are able to reliably detect defects with a much lower false alarm rate than with fixed thresholding. Their detection performance can be quantitatively controlled by a desired false alarm rate that can be maintained consistently throughout a complicated test piece with widely varying grain structure. Indeed, where the unwanted scattering has certain statistical characteristics, the false alarm rate of CFAR detectors is in fact independent of the noise variance. A number of studies have shown that real scattering from grains has characteristics close to that assumed in the theory. However of course, as defects become smaller, the signal to grain noise ratio can be so poor that some form of signal enhancement is required prior to detection.

Major improvements in signal to grain noise ratios can be obtained with a number of signal processing techniques, but some of these are very sensitive to the optimum choice of signal processing parameters. For instance, split spectrum minimisation in conjunction with polarity thresholding can only give good results with the current data if optimised for each individual A-scan. The optimisation requires knowledge of the input signal to noise ratio which is usually unknown *a priori*. Simpler methods such as spatial averaging are less susceptible to parameter selection, but only moderate signal enhancement can be obtained.

In most earlier work related to the current application, the input information from a single channel was used - usually a one-dimensional A-scan time series obtained at one transducer position. Based on analyses of the differential features of typical grain and defect scattering, the novel multi-channel approaches introduced and developed here include: the normalised least mean square (NLMS) adaptive filtering in conjunction with ACML-CFAR adaptive detection, minimum variance distortionless response (MVDR) array processing and two-dimensional adaptive Wiener filtering. Major improvements over existing methods have been achieved by self-optimising filter responses not only according to differential features between the signals and grain noise in the time and or frequency domain, but also according to differential features in the spatial domain.

Experimental evaluations on a set of 64 A-scans obtained during scanning of a coarse-grained JED test piece have shown that small defect signals masked by scattering noise can be detected automatically with near-zero false alarm rate by using novel implementations of NLMS filters in conjunction with ACML-CFAR detection. Typically, NLMS filters can enhance the signal-to-noise ratio by 5~7dB over a whole set of data using constant processing parameters throughout. Not only do these new methods offer much lower false alarm rates than does for instance split spectrum processing, the processing time is much shorter than FFT based methods. In fact, it is feasible to implement the new methods for on-line processing. For instance, as estimated in the Table 6.4.2 a typical number of FLOP's for NLMS adaptive filtering is about 10^5 for a single A-scan. If the

processing is operated in real time at a typical scan rate of 1000 A-scan/sec., the number of float point operation required per second (FLOPS) is about 10^8 or 100 MFLOPS. Using a parallel implementation of the algorithms, it is feasible that this processing speed can be achieved by currently available digital signal processors, such as the TMS320C40's that each have an operating speed of 50 MFLOPS.

Another novel approach evaluated here is to produce enhanced pseudo B-scan images from a set of sequential A-scans using MVDR array processing and two-dimensional adaptive Wiener filtering methods. Results from real A-scan data have shown that the signal-to-noise ratio of images can be significantly enhanced, typically by 7dB with MVDR processing and 15dB with adaptive Wiener filtering. The enhanced images provide visual information that can be interpreted manually according to colour thresholding or automatically by further pattern recognition processing for defect identification, location, sizing and classification.

To summarise: major improvements over existing methods have been achieved by introducing and developing novel multi-channel adaptive filtering approaches based on analyses of the differential features of grain and defect scattering. These approaches optimise filter responses by not only using differential features between the defect signals and grain noise in the time and or frequency domains as in traditional existing methods, but also by adaptively exploiting additional differential features in the spatial domain to enhance the defect signals and images. Automatic detection of the enhanced signals is achieved using constant false alarm rate detectors adapted and developed from well-established radar techniques. The performance of the new approaches is evaluated by processing not just a few A-scans or simulated data as usually shown in the literature, but extensive sets of A-scan data from test blocks containing both artificial targets and real flaws. The results show that the new methods can detect all the test target signals masked by grain noise, with near zero false alarms, and that the visibility of defect images corrupted by grain scattering has been considerably enhanced. An important advantage of the current work is that fixed processing parameters have

been used throughout. Furthermore, some of the methods could be implemented for on-line real-time application using currently available digital signal processors to construct a programmable system that is capable of operation in real time at typical scan rates. These results should encourage further research and development of the approaches proposed. In particular, it could be beneficial to make use of the concepts introduced here in other methods, such as the wavelet transform or neural network-based processing.

8. Future work

The results presented here have shown encouraging improvement in the detection of defect signals masked by grain noise, and in the enhancement of the visibility of defect images embedded in grain scattering. They are a first step towards providing a statistically reliable evaluation for the digital signal/image processing techniques used. A fuller evaluation would involve a larger number of test blocks than available at present as well as large-scale tests with components containing real defects.

In the current work, signal and image enhancement involving frequency domain characteristics has been carried out using the Fast Fourier Transform. An alternative approach for time-frequency domain analysis that has recently attracted some interest in the signal-processing community [Weiss, L.G., 1994] is the wavelet transform method. Since the ultrasound echo signals from defects can be viewed as superposition of scaled and translated replicas of the transmitted signal - a "mother" wavelet, defect signals could be identified by decomposing the signals over the collection of the wavelets, i.e. by taking a wavelet transform. Also, the echo signals scattered by grains are often nonstationary as a result of the inhomogeneous nature of the grain structure. Thus, as has already been discussed, the characteristics of the signal and noise might be anticipated to have localised differential features in both the time and frequency domains. Such characteristics suggest that the performance of signal and image processing based on frequency analysis could be improved by using a wavelet transform in place of a FFT. However, it should be borne in mind that to work well the wavelet transform approach requires at least some distinctive differential features between the wanted signal and the unwanted noise after the transform. One such feature is that the wanted signals are better correlated with the hypothesised wavelets than is the unwanted grain scattering. The current work shows that the data encountered here

is such that these features could be extracted but at a level that may not be significantly distinguishable to offer any major improvement over the methods investigated here. Nevertheless, wavelet transform methods for the current application may be worth investigating in future, especially in conjunction with any new development in signal processing involving localised time-frequency analysis.

Further developments in signal/image enhancement and defect detection, location, sizing and classification could result from an improved understanding of the scattering characteristics of the grains and the true defects. In particular, more theoretical and experimental research is required for the case of small targets with dimensions similar to the grain size, and the dominant wavelengths of the interrogating pulses. Obviously, to discriminate the true defect-signals from the grain noise, it is crucial to identify sufficient differential features that can be incorporated into the processing. However, at present only very limited knowledge of such features is available, therefore the full potential of the techniques investigated has probably not yet been achieved.

One approach to obtain such knowledge could be to make use of recent work¹ to predict echo responses from targets in, albeit, idealised loss-free solids, as a means towards predicting realistic scattering patterns. The ability to do this would not only provide unlimited data for evaluating existing signal processing methods, but could also provide some insight into the physical mechanism of the grain and true defect scattering. This in turn could facilitate further development of improved techniques including, for instance neural network methods, where a detailed knowledge of the features of wanted and unwanted signals is of great benefit. Alternatively, neural network methods could be used as tools to extract discriminating features that could be exploited in further processing.

¹. See for instance: [Weight, J.P., 1993], [Stacey, R., 1993], [Lhemery, A., 1995][Sumbatyan, M. A.,1994] [Sedov, A., 1992]

Finally it is likely that the existing methods developed here could have application for on-line real-time signal processing. A feasibility study is being carried out in conjunction with a number of state-of-the-art digital signal processor suppliers, the conclusion being that adaptive Wiener filtering and NLMS adaptive filter in conjunction with ACML adaptive detection techniques could be implemented in real time with a moderate amount of parallel processing. Such a system would be fully programmable and could therefore incorporate and/or develop further improvements in real-time signal processing.

Glossary of Acronyms

ACML - automatic censored mean level (see page 29).

CFAR - constant False Alarm Rate (see page 23).

FBH - flat-bottom hole (see page 94).

JED - jet engine disc used in the current application (see page 94).

LMS - the least mean square (see page 58).

MGF - moment generating function (see page 19).

MNDR - minimum-noise distortionless response (see page 63).

MVDR - a minimum-variance distortionless response (see page 63).

NLMS - normalised LMS algorithm (see page 60).

SNR - the defect signal to grain noise ratio (see page 90).

SSM - split spectrum minimisation (see page 40)

SSP - split spectrum processing (see page 35).

SSPTM - SSM in conjunction with polarity thresholding (see page 42)

PDF - Probability distribution function (see page 14).

QNDE - quantitative non-destructive evaluation (see page 6).

REFERENCES

- Ahmed, N., Soldan, D.L., Hummels, D.R., and Parikh, D.D., "Sequential regression considerations of adaptive filtering", *Electron. Lett.*, pp.446, July 21, 1977.
- Bamber, J.C., and C. Daft, "Adaptive filtering for reduction of speckle in ultrasound pulse-echo images", *Ultrasonics*, vol 24, pp. 41-44, 1986.
- Beasley, E.W. and Ward, H.R., "Quantitative analysis of sea clutter decorrelation with frequency agility", *IEEE Trans. Aerosp. Electron. Syst. AES-4*, pp468-473. 1968.
- Bilgutay N.M., and Saniie J., "The effect of Grain Size on Flaw Visibility Enhancement Using Split-Spectrum Processing", *Materials Evaluation*, Vol. 42, pp. 808-814, May 1984.
- Bilgutay N.M et al, "Analysis of a non-linear frequency diverse clutter suppression algorithm", *Ultrasonics*, Vol 28, pp. 90-96, 1990.
- Brittain, R., and Weight, J.P., "Fabrication of high-resolution ultrasonic transducers", *Ultrasonics Vol. 25*, 100-106, 1987.
- Burch, S.F., "Comparison of SAFT and two-dimensional deconvolution methods for the improvement of resolution in ultrasonic B-scan images", *Ultrasonics Vol. 25*, pp259-266, Sept. 1987.
- Challis, R. E., "Ultrasonic Compression Wave NDT of Adhered Metal Lap Joints of Uncertain Dimensions", *INSIGHT*, Vol. 37, No. 12, pp954-963, 1995.

- Donohue, K.D., "Maximum likelihood estimation of A-scan amplitude for coherent targets in media of unresolvable scatterers", *IEEE Trans. on Ultras. Ferroelectr. and Freq. Contr. Vol. 39, No. 3, May 1992.*
- Donohue, K.D., Bressler, J.M., Varghese, T., and Bilgutay, N.M., "Spectral correlation in ultrasonic pulse echo signal processing", *IEEE Trans. on Ultras. Ferroelectr. and Freq. Contr. Vol. 40, No. 4, July 1993.*
- Finn, H.M. and R.S. Jonson, "Adaptive Detection Mode with Threshold Control as a Function of Spatially Sampled Clutter-level Estimates", *RCA Rev. Vol. 30, pp. 414-464, Sept. 1968.*
- Gandhi P.P. and S.A. Kassam, "Analysis of CFAR Processors in Nonhomogeneous Background", *IEEE Transactions on Aerospace and Electronic Systems Vol. 24 No.4 July 1988.*
- Hansen, V.G. and H.R. Ward, "Detection Performance of the Cell Averaging LOG/CFAR Receiver", *IEEE Trans. AES-8, pp. 648-652, Sept. 1972.*
- Hansen, V.G., "Constant False Alarm Rate Processing in Search Radars", *IEE 1973 International Radar Conference, London, pp. 325-332, Oct., 1973.*
- Himonas, S.D. and Barkat, M., "Automatic Censored CFAR Detection for Nonhomogeneous Environments", *IEEE Transactions on Aerospace and Electronic Systems Vol. 28 No.1 January 1992.*
- Hou, X.Y. et al., "Direct Evaluation of Radar Detection probabilities", *IEEE Transactions on Aerospace and Electronic Systems Vol. 23 No.4, pp418-423, July 1987.*

- Ilan, A. and Weight, J.P., "The propagation of short pulses of ultrasound from a circular source coupled to an isotropic solid", *J. Acoust. Soc. Am.* 88 (2), August, 1990.
- Karpur, P. et al., "Split spectrum processing: optimizing the processing parameters using minimisation", *Ultrasonics Vol. 25*, pp204-208, July 1987.
- Karpur, P. et al., 1988, "Split spectrum processing: determination of the available bandwidth for spectral splitting", *Ultrasonics Vol. 26*, pp204-209, July, 1988.
- Kraus, S. and K. Goebels, "Improvement of signal-to-noise ratio for the ultrasonic testing of coarse grained materials by signal averaging techniques", *Proc. First Int Symp Ultrason. Mater Charact., Gaithersburg, USA, 7-9 June 1978*.
- Lee, J.S., "Digital image enhancement and noise filtering by use of local statistics", *IEEE Trans. Patt. Ana. Mach. Int., Vol. PAMI-2*, March, 1980, pp.165-168.
- Lhemery, A. "Impulse-response method to predict echo-responses from defects in solids - Part I: Theory", *J.Acoust.Soc. Am.* 98 (4) (1995), p. 2208-3787.
- Lim, J.S., "Two-dimensional signal and image processing", *Prentice-Hall International, Inc.*, pp.365-367, 1990.
- Luis, V.D., "Backscattering grain noise modelling in ultrasonic non-destructive testing", *Waves in Random Media 1*, pp81-92, 1991.
- Mason, W.P. and McSkimin, J.H. 1947, "Attenuation and scattering of high frequency sound waves in metals and glasses", *JASA*, 19 pp. 464-473, 1947.

- Mohana, P., "Split-spectrum processing: analysis of polarity thresholding algorithm for improvement of signal-to-noise ratio and detectability in ultrasonic signals", *IEEE Trans. on UFFC. Vol. 36, No. 1, pp101-108, Jan. 1989.*
- Moor, J.D. and N.B. Lawrence, "Comparison of Two CFAR Methods Used with Square Law Detection of Swerling I Target", *IEEE 1980 International Radar Conference, Washington, D.C., pp. 403-409, 1980.*
- Murthy, R. Bilgutay, N.M. and Saniie, J. 1989, "Application of Bandpass Filtering in Ultrasonic Non-destructive Testing", *Review of progress in Quantitative Nondestructive Evaluation of Materials (QNDE), Vol. 8, pp. 759-767, 1989.*
- Newhouse, V.L. Bilgutay, N.M. Saniie, J. and Furgason, E.S. 1982, "Flaw-to-Grain Echo Enhancement by Split-Spectrum Processing", *Ultrasonics, Vol. 20, pp. 59-68, Mar. 1982.*
- Newhouse. V.L and et al. "A real time split spectrum processing system", *Ultrasonics International 89 Conference proceedings, pp. 43-46, 1989.*
- Papadakis, E.P., "Ultrasonic attenuation caused by scattering in polycrystalline media", *Physical Acoustics, Vol. IV - part B, pp269-328, (Ed. Mason, W.P.) Academic Press, New York, USA. 1968.*
- Papadakis, E.P., "Scattering in polycrystalline media", *Methods of Experimental Physics, Vol. 19, Ultrasonics, P.D. Edmonds, Ed. Academic Press, New York, pp. 237-298, 1981.*
- Papoulis, A., "Probability, random variables, and stochastic processes", *McGraw-Hill, Inc., New York, 3rd edition, pp.93, (1991).*

- Rohling, H., "Radar CFAR Thresholding in Clutter and Multiple Target Situations", *IEEE Trans. AES-19*, pp. 608-621, July 1983.
- Saniie, J. et al., "Quantitative grain size evaluation using ultrasonic backscattered echoes", *J. Acoust. Soc. Am.* 80, pp1816-1824, 1986.
- Saniie, J. et al., "Statistical evaluation of backscattered ultrasonic grain signals", *J. Acoust. Soc. Am.* 84, pp400-408, 1988.
- Saniie J. and D.T. Nagle, "Analysis of Order-Statistic CFAR Threshold Estimators for Improved Ultrasonic Flaw Detection", *IEEE Trans. on Ultras. Ferro. & Freq. Contr.*, vol. 39, pp. 618-629, Sept. 1992.
- Sedov, A., Schmerr, L. and Sung, S. J., "Ultrasonic scattering by a flat-bottom hole in immersion testing", *J. Acoust. Soc. Am.* 92, 478-486 (1992).
- Shankar, P.M. Bencharit, U. Bilgutay, N.M. and Saniie, J. 1988, "Grain Noise Suppression through Bandpass Filtering", *Materials Evaluation*, Vol. 46, pp. 1100-1104, July 1988.
- Shen, G., Semiatin, S.L., and Shivpuri, R., "Modeling microstructural development during the forging of Waspaloy", *Metallurgical and materials Trans. A*, Vol. 26A, pp.1795-1803, July 1995.
- Stacey, R., and Weight, J.P., "Ultrasonic echo responses from targets in solid media using finite difference methods". *IEE Procs Part A* vol 140 No 4 303-316 (1993).
- Sumbatyan, M. A. and Boyev, N. V., "Mathematical modeling for the practice of ultrasonic inspection" *Ultrasonics*, 32, 5-11 (1994).

- Tarrab, M. and Feuer, A., "Convergence and performance analysis of the normalized LMS algorithm with uncorrelated Gaussian data", *IEEE Trans. on Info. Theory*, Vol. 34, No. 4, pp.680-691, July, 1988.
- Van Trees, H.L. "Detection, Estimation, and Linear Modulation Theory", *New York, Wiley*, pp182, 1968.
- Vaughan, R.J. and Venables, W.N., "Permanent expressions for order statistic densities", *J.R. Statistical Society, B*, 34, pp308-310, (1972).
- Weight, J.P., "The propagation and reception of wide-band ultrasonic pulses". *Ph.D. Thesis, The City University*, (1982).
- Weight, J.P., "Resolution transducers, systems and methods for the transmission and/or reception of waves propagated by vibration". *U.S.A. Patent No. 4,509,153* (1982).
- Weight, J.P., "New transducers for high-resolution ultrasonic testing". *NDT International*, Vol 17, No. 1, *Butterworth & Co (publisher) Ltd.*, (1984).
- Weight, J.P., "High resolution ultrasonic transducers". *Proceedings of the British Institute of Non-Destructive Testing - 21st Annual Conference. British Institute of NDT, Newcastle UK*, 335-350 (1986).
- Weight, J.P., "Modelling of ultrasonic pulse-echo techniques for the detection and characterisation of small targets in solids". In: *Proceedings of the 13th World Conference on Non-destructive Testing. Sao Paulo, Brazil. Eds C. Hallai and P. Kulcsar. Elsevier* (1992).
- Weight, J.P., "A model to predict the ultrasonic echo responses of small targets in solids", *J. Acoust. Soc. Am.* 94, 514-526 (1993).

Widrow, B. et al., "Adaptive Noise Cancelling: Principles and Applications", *Proc. IEEE*, vol 63, pp. 1692-1716, Dec. 1975.

Widrow, B. and Stearns, S.D., "Adaptive Signal Processing", *Prentice-Hall, Inc., Englewood Cliffs, N.J.* 1985.

Yan, A. and Vural, A.M., "On overview of adaptive array processing for sonar applications", *EASCON*, 34-A, 1975.

Yue, Li et al, "Two signal processing techniques for the enhancement of the flaw-to-grain echo ratio", *Ultrasonics*, vol 25, pp. 90-94, March 1987.

Zhu, Y. and Weight, J. P., "Ultrasonic non-destructive evaluation of highly-scattering materials using adaptive filtering and detection", *IEEE Trans. on Ultras. Ferro. & Freq. Contr. Vol. 41 No. 1*, pp.26-33, January 1994.

Zhu, Y. and Weight, J. P., "Adaptive signal processing techniques to improve ultrasonic flaw detection in highly-scattering materials", *Review of Progress in Quantitative NDE, Vol. 13A*, pp.817-824, 1993.